THE EFFECTS OF HEAT INPUT ON TENSILE AND FATIGUE PROPERTIES OF SUBMERGED ARC WELDED ASTM A709 GRADE 50 STEEL

A Thesis Submitted to the College of

Graduate Studies and Research

In Partial Fulfillment of the Requirements

For the Degree of Master of Science in Engineering

In the Department of Mechanical Engineering

University of Saskatchewan

Saskatoon

By

Shufang Shen

PERMISSION TO USE

In presenting this thesis in partial fulfilment of the requirements for a Postgraduate degree from the University of Saskatchewan, I agree that the Libraries of this University may make it freely available for inspection. I further agree that permission for copying of this thesis in any manner, in whole or in part, for scholarly purposes may be granted by professors I. N. A. Oguocha and S. Yannacopoulos who supervised my thesis work or, in their absence, by the Head of the Department or the Dean of the College in which my thesis work was done. It is understood that any copying or publication or use of this thesis or parts thereof for financial gain shall not be allowed without my written permission. It is also understood that due recognition shall be given to me and to the University of Saskatchewan in any scholarly use which may be made of any material in my thesis.

Requests for permission to copy or to make other use of material in this thesis in whole or part should be addressed to:

Head of the Department of Mechanical Engineering

University of Saskatchewan

Saskatoon, Saskatchewan S7N 5A9

ABSTRACT

The purpose of this study was to investigate the effects of heat input on tensile and fatigue properties of submerged arc welded American Society for Testing and Materials (ASTM) A709 Grade 50 steel, which was supplied as plates with dimensions of 500 mm × 250 mm × 20 mm by Hitachi Canadian Industries (HCI) Ltd., Saskatoon. Identical heat input (2.75 kJ/mm) was used to weld one side of the plates, while various heat inputs (single wire: 3.03 kJ/mm and 3.43 kJ/mm; tandem wires: 4.11 kJ/mm and 4.56 kJ/mm) were used for the second side. The weld properties were evaluated using visual inspection, ultrasonic inspection, hardness measurements, tensile and fatigue testing, weld bead geometry measurement, optical microscopy and scanning electron microscopy.

The results obtained showed that heat input affected the microstructure, hardness and weld bead geometry of ASTM A709 Grade 50 steel welds appreciably, but had little effect on the tensile and yield strengths. Increase in heat input slightly reduced the amount of acicular ferrite within the weld metal zone, and resulted in coarser microstructures in the coarse-grained heat-affected zone. The hardness of the coarse-grained heat-affected zone and the weld metal zone increased with increasing heat input. The penetration depth, heat affected zone size, bead width, bead reinforcement, penetration area, and nugget area of the weld increased with increasing heat input for both single wire and tandem wire welding, but the contact angle decreased. Electrode melting efficiency increased with increasing heat input for single wire welding, but the

plate melting efficiency only changed within 4% between single wire and tandem wire welding. Percent dilution remained practically unchanged with increasing heat input. In general, the fatigue strength of the welds was slightly higher than that of the parent metal at room temperature. The fatigue strength of ASTM A709 Grade 50 steel and its welds increased slightly at -20 °C and -30 °C compared to room temperature. At room temperature, the welds showed slightly higher fatigue strength than the parent metal.

ACKNOWLEDGEMENTS

I would like to express my appreciation to my supervisors, Professors I. N. A. Oguocha and S. Yannacopoulos, for their encouragement, guidance, and support throughout this research project. I would like to thank my supervisory committee members, Professors C. Zhang and A. Odeshi, for their support, suggestions and useful feedback during the completion of this work.

I would like to express my gratitude to Mr. Rob McEachern and Mr. Jayson Koroll of Hitachi Canadian Industries Ltd., Saskatoon, for their help and provision of materials and welding. I wish to thank Professor C. Simonson for allowing me to use his cold room for low temperature fatigue testing. I wish to express my appreciation to Mr. Robert Peace, Mr. Hans-Jüergen Steinmetz and Mr. Dave Deutscher for their valuable technical assistance. Technical assistance from Mr. Keith Palibroda and Mr. Cam Tarasoff of the Engineering Shop is also greatly appreciated.

Finally, I would like to acknowledge the financial support from Hitachi Canadian Industries Ltd., the Natural Sciences and Engineering Research Council (NSERC), and the Department of Mechanical Engineering, University of Saskatchewan.

May God bless them all.

DEDICATION

I would like to dedicate this thesis to my parents, Liming Shen and Minyi Shen, and Jianwei (Mark) Li, for their unconditional love, support, wise advice, and for always been there for me.

TABLE OF CONTENTS

LIST OF TABLES

LIST OF FIGURES

NOMENCLATURE

Abbreviations

ASTM	American Society for Testing and Materials
SMAW	Shield metal arc welding
GMAW	Gas metal arc welding or gas metal arc welded
GTAW	Gas tungsten arc welding
SAW	Submerged arc welding or submerged arc welded
FCAW	Flux-cored arc welding or flux-cored arc welded
WM	Weld metal
HAZ	Heat-affected zone
PM	Parent metal
HPS	High performance steel
WI	Weld interface
CGHAZ	Coarse-grained heat-affected zone
FGHAZ	Fine-grained heat-affected zone
GBF	Grain boundary ferrite
AF	Acicular ferrite
BF	Block ferrite
WSPF	Widmanstätten side plate ferrite
HI	Heat Input
I	Welding current

V	Arc voltage
S	Welding speed
CR	Cooling rate
CCT	Continuous cooling transformation
T_0	Initial temperature
HSLA	High-strength low-alloy
Ms	Martensite start temperature
Mf	Martensite finish temperature
M-A-C	Martensite-austenite-carbide
H	Heat-affected zone size
W	Bead width
MTR	Mill test report
HCI	Hitachi Canadian Industries
ICP-MS	Inductively coupled plasma mass spectroscope
AWS	American Welding Society
T1	Code for plates welded using a heat input of 3.03 kJ/mm
T2	Code for plates welded using a heat input of 3.43 kJ/mm
T3	Code for plates welded using a heat input of 4.11 kJ/mm
T4	Code for plates welded using a heat input of 4.56 kJ/mm
SEM	Scanning electron microscope or scanning electron microscopy
P	Penetration depth
R	Bead reinforcement
A_p	Penetration area of an unbeveled, gapless welded joint

A_d	Deposition or nugget area of an unbeveled, gapless welded joint
A_t	Total molten area
A_p'	Penetration area of a beveled, gapless welded joint
A_d'	Deposition area of a beveled, gapless welded joint
M	Bending moment
D	Diameter of the specimen
A_b	Cross-sectional area of beveled section
E_{pm}	Plate melting efficiency
E_{em}	Electrode melting efficiency
E_{tm}	Total melting efficiency
N_f	Number of cycles to failure
S-N curve	Stress amplitude vs number of cycles to failure curve
b	Fatigue strength exponent
K_f	Fatigue stress concentration factor
K_t	Stress concentration factor

Greek Symbols

η	Arc efficiency
$\Delta t_{8/5}$	Cooling time from 800 °C to 500 °C
λ	Thermal conductivity
θ	Contact angle
σ_n	Fatigue limit
σ_u	Ultimate tensile strength / Tensile strength
σ	Nominal stress
$\sigma_{\max}$	Maximum stress of the cycle
$\sigma_{\min}$	Minimum stress of the cycle
σ_a	Stress amplitude
σ_m	Mean stress of the cycle
σ_f'	Fatigue strength coefficient

CHAPTER 1

INTRODUCTION

1.1 Overview

Wind power generated by the wind turbine is one of the clean, green, and renewable sources of alternative energy. Worldwide growth in wind power generation since 1994 has been 30% or higher annually (Ancona and McVeigh, 2010). A wide range of materials are used for manufacturing wind turbines. Aluminum or other light weight composites are used for small-size wind turbines. In large wind turbines, however, the turbine material is and will continue to be dominated by steels to meet strength and structural fatigue requirement (Ancona and McVeigh, 2010).

American Society for Testing and Materials (ASTM) A709 Grade 50 steel is widely used for wind turbine towers as well as high-pressure vessels, gas and/or oil pipelines and bridges. It is a high-strength low-alloy steel with low carbon content (0.05 to 0.25 wt% C) and small additions of alloying elements such as niobium, aluminum, vanadium, titanium, molybdenum, copper, and zirconium (Gladman, 1997). Compared to conventional structural steels, ASTM A709 Grade 50 steel provides high yield and tensile strengths, improved toughness, and good weldability.

Welding is the primary fabrication method for manufacturing wind turbine towers and bridges. The primary arc welding methods include shield metal arc welding (SMAW), gas metal arc welding (GMAW), gas tungsten arc welding (GTAW), and submerged arc welding (SAW). Compared to other techniques, SAW is commonly used for fabricating large diameter pipes, ships, pressure vessels, offshore constructions, and wind turbine towers because it offers ease of automation, low operator skill requirements, high deposition rate, deep penetration, high quality welds, excellent surface finish, ability to weld thick plates, and minimum welding fumes (Thornton, 1992; Sevensson, 1994; ASM Metals Handbook, 1983; Chandel *et al*., 1997). Several controllable process parameters influence the weld bead geometry and welded joint characteristics produced using SAW (Chandel *et al*., 1997; Murugan and Gunaraj, 2005; Lee, *et al*., 2000). These include arc voltage, welding current, travel speed, wire feed rate, nozzle-to-plate distance, electrode diameter, and the electrode polarity. The arc voltage, welding current, and travel speed control the heat input to a weld. The high deposition rate in the SAW process results in high productivity, but it requires high heat input. The high heat input means slow cooling rate (Poorhaydari *et al*., 2005), which may affect the mechanical properties of the welded joints. It was reported that increasing the heat input led to an increase in productivity, but it was at the expense of the tensile properties (Chandel *et al*., 1997).

1.2 Motivation

Submerged arc welded ASTM A709 Grade 50 steel joints are often subjected to cyclically varying loads in applications such as wind turbine towers, gas and/or oil

pipelines and bridges. Thus, it is necessary to investigate their fatigue properties. In addition, it is important to understand how welding heat input affects the quality of welds, including fatigue strength, tensile strength, hardness, weld bead geometry and microstructure.

Fatigue properties of the welded joint depend on the mechanical properties and microstructure, which are affected by the welding heat input. Research has shown that heat input affects the microstructure (Dallam *et al*., 1985; Harrison and Farrar and Harrison, 1987a; Jang and Indacochea, 1987; Huang *et al*, 1994; Wang and Liu, 2002; Yang, 2008; Donald *et al*., 1952; Sundaram *et al*., 1987; Kim *et al*., 1991; Güral *et al*, 2007), toughness (Bhole and Billingham, 1983; Farrar and Harrison, 1987a; Sundaram *et al*., 1987; Moeinifar *et al*., 2011; Wang and Liu, 2002; Neves and Loureiro, 2004; Kim *et al*., 2005; Gharibshahiyan *et al*., 2011), hardness (Smith *et al*., 1989; Moeinifar *et al*., 2011; Neves and Loureiro, 2004; Yurioka *et al*, 1987; Gharibshahiyan *et al*., 2011), and tensile strength (Smith *et al*., 1989; Vercesi and Surian, 1998; Neves and Loureiro, 2004; Prasad and Dwivedi, 2008) of the weld metal (WM) zone and heat-affected zone (HAZ) of the welded joints. Thus, this necessitates investigation of the effect of the heat input on the fatigue and mechanical properties of SAW A709 Grade 50 steel joints.

Research has also shown that fatigue properties of the welded steel joints are also dependent on the weld bead geometry (Gurney, 1968; Ninh and Wahab, 1995a; Ninh and Wahab, 1995b; Ninh and Wahab, 1998; Lee *et al*., 2009), which is also affected by

the welding heat input (Chandel *et al*., 1997; Karadeniz *et al*., 2007; Clark, 1985; Lee *et al*., 2000; Chandel, 1990; Chandel and Hang, 1996; Palani and Murugan, 2009; Benyounis and Olabi, 2008; Gunaraj and Murugan, 1999; Murugan and Gunaraj, 2005; Dhas and Kumanan, 2007; Juang and Tang, 2002; Kim *et al*., 2003; Nagesh and Datta, 2002; Rao *et al*., 2009; Palani and Murugan, 2007; Hrabe *et al*., 2009; Tarng and Yang, 1998). Thus, it is necessary to study the effect of the heat input on the weld bead geometry of the SAW A709 Grade50 steel joints.

In cold regions of the world, SAW ASTM A709 Grade 50 steel joints work in the climatic temperature range of +20 to -60 °C (Kobrin *et al*., 1972). However, little research (Forrest, 1962; Frost *et al.*, 1999) has been conducted to investigate fatigue properties of welded steels under sub-zero temperatures.

1.3 Objectives

This study was carried out to achieve the following objectives:

(1) To investigate the effect of heat input on the tensile properties and microstructure of the SAW ASTM A709 Grade 50 steel.

(2) To investigate the effect of heat input on the weld bead geometry of SAW ASTM A709 Grade 50 steel.

(3) To investigate the effect of heat input on the fatigue properties of SAW ASTM A709 Grade 50 steel at room and sub-zero temperatures.

1.4 Thesis Outline

This thesis is organized as follows. Chapter 1 presents an overview of the research project, its motivation, and main objectives. A comprehensive literature survey relating to this project is presented in Chapter 2. Chapter 3 discusses materials and experimental methods applied in this study. Chapter 4 presents and discusses the experimental results. Chapter 5 contains the conclusions deduced from the results and recommendations for future work.

CHAPTER 2

LITERATURE REVIEW

This chapter presents a brief review of (1) the properties of ASTM A709 Grade 50 steel, (2) submerged arc welding, (3) effects of welding heat input on mechanical properties, (4) effect of heat input on weld bead geometry, and (5) factors affecting fatigue properties of welded joints.

2.1 ASTM A709 Grade 50 Steel

ASTM A709 steel is produced in seven grades (i.e., 36, 50, 50S, 50W, HPS 50W, HPS 70W, and HPS 100W) in four yield strength levels (i.e., 36 ksi/250 MPa, 50 ksi/345 MPa, 70 ksi/485 MPa, and 100 ksi/690 MPa) (ASTM Standard A709/A709M, 2009). ASTM A709 Grade 50 steel, with minimum yield strength of 345 MPa, is used widely in the industry for constructing bridges, cranes and wind turbine towers due to its high yield and tensile strengths, high ductility, high toughness, and good weldability. The main constituent of ASTM A709 Grade 50 steel is iron and the main alloying elements include carbon, manganese, silicon, molybdenum, chromium, titanium, nickel, copper, and nitrogen. The mechanical properties of steels are sensitive to the amount and type of elements they contain.

Carbon (C) is the most important alloying element in steel. Adding carbon strengthens and hardens steel, and increases its wear resistance and ability to harden by heat treatment. However, high carbon content hinders weldability, decreases the ductility, and reduces impact toughness of the steel (ASM Handbook, 1990). Carbon in excess of 0.2 wt. % in plain carbon steels forms hard microstructures such as martensite and bainite (ASM Handbook, 1990).

Manganese (Mn) is normally present in all commercial steels to form manganese sulfide stringers, which counteracts the harmful effects of sulphur and improves the machinability of steel (Davis, 2001). In addition, it can provide solid solution strengthening (ASM Handbook, 1990), grain refinement (Davis, 2001), increased hardenability (Davis, 2001) and improved toughness (Harrison and Farrar, 1987).

Silicon (Si) acts as a deoxidizer; fully killed steels usually contain 0.15 to 0.30 wt. % Si for deoxidation. It slightly increases the strength of steel through solid solution strengthening of ferrite, without causing a serious reduction of ductility. However, a high proportion of Si tends to deteriorate toughness and weldability (Davis, 2001).

Elements such as molybdenum (Mo), chromium (Cr), nickel (Ni), copper (Cu), vanadium (V), niobium (Nb) and titanium (Ti) can strengthen steels. Mo increases the hardenability of steels (Davis, 2001). Adding 0.1-0.2 wt. % Mo produces a fine structure of acicular ferrite. Cr is added as a hardening element and is usually used with Ni to produce superior mechanical properties (Davis, 2001). Ni is used to increase toughness

(Harrison and Farrar, 1987) and to improve the low-temperature properties of low-carbon steels (Davis, 2001). Cu improves strength of steel through solid solution strengthening of ferrite and contributes to the corrosion resistance of carbon steels (Davis, 2001). V is generally added to improve strength of steels by controlling grain growth during heat treatment. Small addition of Nb can increase yield and tensile strengths of carbon steels. Ti forms several compounds that provide grain refinement, precipitation strengthening, and sulfide control in low carbon steels.

2.2 Submerged Arc Welding

2.2.1 The Process

Welding is defined as "a process that produces joining of materials by heating them to the melting temperature with or without the application of pressure or by the application of pressure alone and with or without the use of a filler material" (Messler, 2004). There are more than 80 different types of welding processes in commercial use today. Fusion welding is the most widely used welding operation, which involves melting two edges or surfaces and joining them by adding a small amount of molten steel or filler metal into the gap between the two components. Submerged arc welding (SAW) is one of the most commonly used fusion welding processes.

Figure 2.1 shows a typical single-wire SAW process. An arc generated by an electric current passes between the electrode wire and the workpiece generating enough heat to

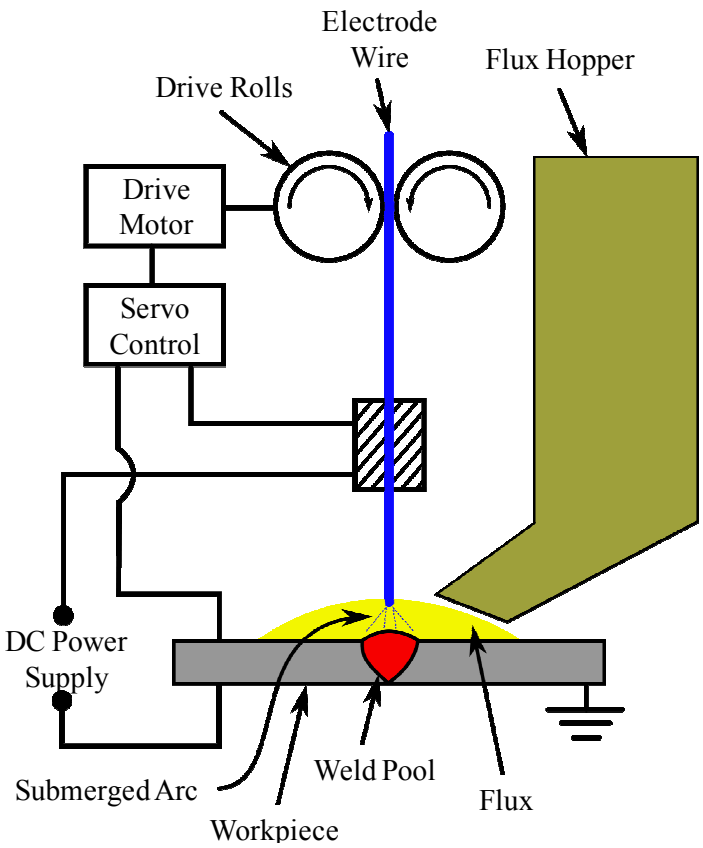

Figure 2.1. A schematic diagram of submerged arc welding process (Wikipedia, 2011).

melt both parent metal and welding wire. The welding wire speed is controlled by a wire feeder to adjust the deposition rate according to different heat inputs. The electric arc and the molten metal are submerged in a bed of granulated mineral material known as the flux, which is supplied from a flux hopper. The flux forms a glass-like slag and floats on the surface as a protective cover against oxidization of the steel. With the flux, no sparks or spatters are produced resulting in a clean welding operation with little fumes. When the welding process is done, the weld metal and flux cool and solidify forming a weld bead covered with a protective slag shield.

Due to its high deposition rate, high quality welds, ease of automation, and release of minimum welding fumes, SAW is commonly used for fabricating large diameter pipes, pressure vessels, offshore constructions, and wind turbine towers (Thornton, 1992; ASM Metals Handbook, 1983; Sevensson, 1994). However, SAW has some limitations: (a) it is limited to welding carbon steels, HSLA steels, stainless steels, and some nickel-based alloys; (b) it can be used only in a flat or horizontal position because of the use of the granular flux; (c) it requires maintaining correct electrode alignment; (d) as in other welding processes, it may result in welding defects such as cracks and lack of penetration; and (e) it may raise health and safety issues because of flux and slag remains (ASM Metals Handbook, 1983).

2.2.2 Structure of a Welded Joint

Figure 2.2 shows four distinct metallurgical zones that are formed in the welded joint during cooling and solidification of the weld pool after welding. These four weld zones are (a) unaffected zone or parent metal (PM), (b) weld interface (WI) or fusion line, (c) heat-affected zone (HAZ) and (d) fusion zone or weld metal (WM). Figure 2.3 shows approximate relationships among peak temperature, weld zones and iron-carbon phase diagram. The size of the HAZ and WM is a result of the severity of the thermal cycle, experienced by heating and cooling. The HAZ is subjected to the full weld thermal cycle and the WM in single-pass is exposed to the cooling part of the cycle. The different temperatures at different welded zones result in a heterogeneous cooling rate in the welded joint. Therefore, the microstructures of a welded joint are different from zone to

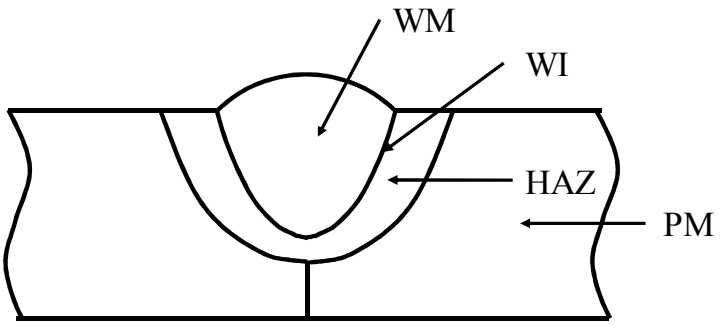

Figure 2.2. Sketch of a single-side SAW joint.

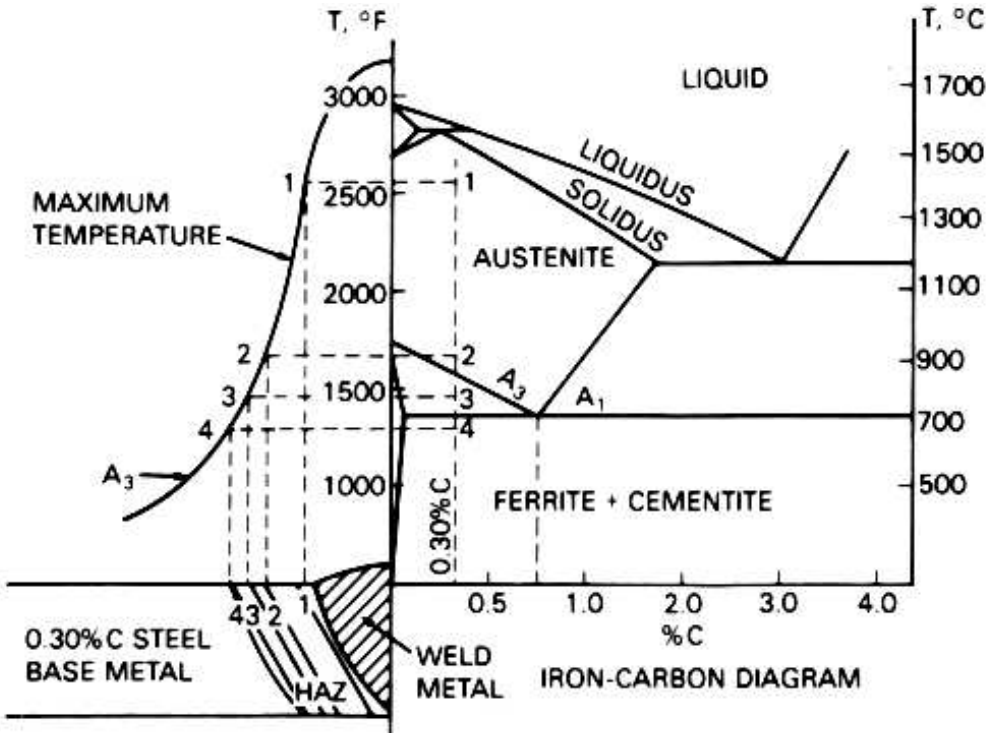

Figure 2.3. A schematic diagram of various regions within a welded joint approximately indicated on the iron-carbon diagram (Connor, 1987).

zone. The microstructures of the HAZ and WM are also strongly influenced by the composition of the PM, electrode wire and flux, the prior grain size of the PM, and the number of welding passes, which strongly affects grain growth and grain transformation (Lancaster, 1999).

The PM retains the same microstructure as the material in the as-received condition and retains its original properties (Donald *et al*., 1952). The typical grain microstructure of the PM of low-carbon steel is of ferrite and pearlite. The PM surrounding the HAZ suffers from residual shrinkage stress (Lancaster, 1999).

The HAZ is an undesirable zone. The metal in this zone experiences temperatures below the melting point but high enough to change the microstructures. The HAZ consists of sub-zones. As shown in Figure 2.3, it can be further divided by temperature, which ranges from 700 °C to 1400 °C (Connor, 1987). In region 1, austenite grain can grow because this region is close to the fusion boundary of the weld metal and considerable time spent at temperature near the melting point of the metal. Therefore, the coarse-grained heat-affected zone (CGHAZ) is formed in this region. The CGHAZ is characterized by high levels of embrittlement due to the coarse-grained structure that provides low resistance to crack propagation. The CGHAZ is normally considered to be the region of the welded joint with the lowest sub-zero temperature toughness causing researchers to label it as a local brittle zone (Lancaster, 1999). The low toughness in the CGHAZ can be explained by the formation of undesirable microstructures such as upper bainite and martensite. Region 2 is austenitized, but the temperature is not high enough

to promote grain growth. The smallest grain structure exists in region 3, called the fine-grained heat-affected zone (FGHAZ). In this region, some grains are austenitized and some are not. The austenite grains are very fine. In region 4, no austenite transformation takes place, but the ferrite grain may be tempered by the heat of welding.

The WI is a narrow boundary which separates the WM from the HAZ. It consists of parent metal that has undergone full or partial melting during the welding process and remains unmixed with the filler metal.

The WM is a mixture of the parent metal, filler metal and alloying elements in the flux, which are completely melted during the fusion process. During solidification, grains tend to grow in a direction perpendicular to the weld interface because this is the direction of the maximum temperature gradient and thus the maximum driving force for the solidification (Kou, 1987). Columnar structure is formed as the weld cools from the parent metal to the center of the weld metal. The microstructure of the WM is obtained as the WM cools from the liquid phase to the room temperature. Transformation of the microstructure in the WM mainly depends on the cooling rate and alloying elements of the steel. Primary microstructures, such as grain boundary ferrite (GBF), acicular ferrite (AF), block ferrite (BF), Widmanstätten side plate ferrite (WSPF) and upper bainite may be obtained in the WM of low-carbon low-alloyed steels (Dallam *et al*., 1985; Harrison and Farrar, 1987).

2.3 Effect of Heat Input on the Properties of Welded Joints

2.3.1 Cooling Rate and Heat Input

In the arc welding process, heat input is an important parameter because it controls the cooling rate of the welded joint and, therefore, affects the microstructure and mechanical properties of the WM and the HAZ. Heat input cannot be measured directly (Funderburk, 1999). However, it can be calculated from the measured arc voltage, welding current, and welding speed as follows (Easterling, 1992):

$$\mathrm{HI} = \eta \frac{I \times V}{1000 \times S} \left(\mathrm{kJ \cdot mm^{-1}}\right) \tag{2.1}$$

where I = welding current (A), V = arc voltage (V), S = welding speed (mm·s^{-1}), and η = arc efficiency. In this study, η = 0.95, which is the mean of the range of values reported for SAW process in (Easterling, 1992).

The cooling rate is a primary factor that determines the final microstructure of the WM and HAZ. The cooling time from 800 °C to 500 °C ($\Delta t_{8/5}$) and the cooling rate (CR) can be determined using equations (2.2), (2.3) and (2.4) (Poorhaydari *et al*., 2005).

$$\Delta t_{8/5} = \frac{\mathrm{HI}}{2\pi\lambda} \cdot \frac{1}{\rho} \mathrm{(s)} \tag{2.2}$$

$$\frac{1}{\rho} = \frac{1}{500 - T_0} - \frac{1}{800 - T_0} \tag{2.3}$$

$$CR = \frac{300}{\Delta t_{8/5}} \left({}^{o}C \cdot s^{-1} \right) \tag{2.4}$$

where λ = thermal conductivity (41 $J \cdot s^{-1} \cdot m^{-1} \cdot {}^{o}C^{-1}$) and T_0 = initial temperature (= 25 ºC) (Poorhaydari *et al*., 2005). Therefore, the relationship between the heat input and the cooling rate can be expressed as:

$$CR \propto \frac{1}{HI} \tag{2.5}$$

2.3.2 Microstructures

Chemical composition, cooling rate (heat input), prior austenite grain size, and inclusion content are considered as the main factors that influence the austenite-to-ferrite transformation in the weld metal (Harrison and Farrar, 1987; Jang and Indacochea, 1987). A typical continuous cooling transformation (CCT) diagram of C-Mn weld metal is shown in Figure 2.4 (Lancaster, 1999). From this diagram, it can be seen that transformation from austenite starts with the formation of proeutectoid ferrite around the austenite grain boundaries. The interior of the austenite grains then transforms into either side plate ferrite or acicular ferrite or both. For most weld metals, there is a tendency to form acicular ferrite for increased cooling rates (Harrison and Farrar, 1987). Slow cooling rates produce pearlite (see Figure 2.4). When cooling rate increases, the austenite-to-ferrite transformation temperature is lowered and carbon atoms do not have enough time to diffuse into the ferrite to form pearlite (Lancaster, 1999). The carbide precipitates appear in the form of needles or plates around or within the ferrite. So,

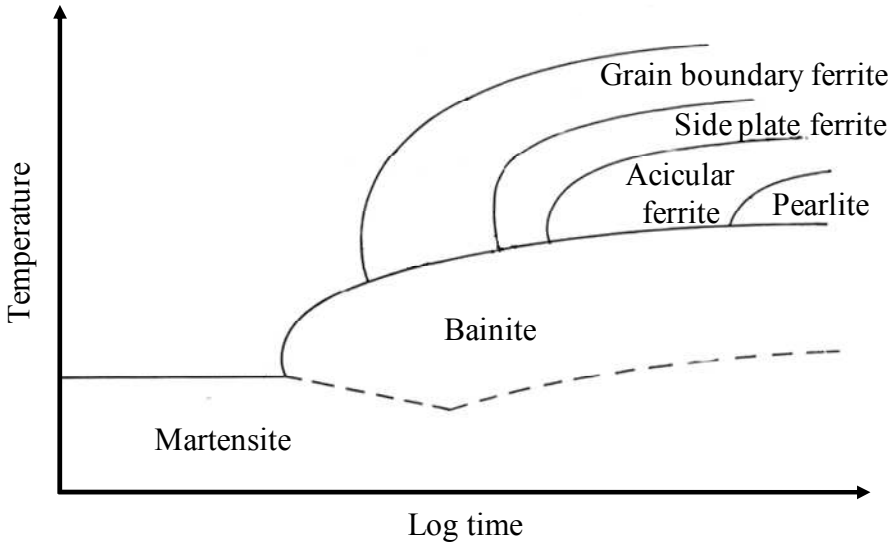

Figure 2.4. Continuous cooling transformation (CCT) diagram for a typical carbon-manganese (C-Mn) weld deposit (Lancaster, 1999).

bainite is formed. At very high cooling rates, martensite is formed and carbon atoms are retained in solid solution.

Huang *et al.* (1994) studied submerged arc welded (SAW) SA516 Grade 70 steel joint produced using a heat input of 1.5 kJ/mm. They found that the WM consisted of GBF, AF, and WSPF. Dallam *et al.* (1985) investigated niobium alloyed HSLA steel weldments with heat inputs of 1.9 and 3.3 kJ/mm. The low heat input welds showed a predominantly fine microstructure of AF. Yang (2008) found that the WM of ASTM A709 Grade 50 consisted of a large volume fraction of AF and GBF for the heat inputs of 1.83 to 4.15 kJ/mm. Wang and Liu (2002) reported that HSLA-100 steel welded joints exhibited a predominantly AF structure with some coarse granular bainite. Farhat (2007) found that the microstructure of the WM of X80 steel weld consisted mainly of a large amount of AF and minor amount of GBF for the heat inputs of 1.37 to 2.24 kJ/mm.

The austenite-to-ferrite transformation in the HAZ occurs in a similar manner to that of the WM. The austenite grains in the HAZ transform into different microstructures during the cooling process. As heat input increases, cooling rate is lowered. The reverse condition produces a fast cooling rate. Under a very fast cooling rate (low heat input), the austenite can transform to martensite in the HAZ. This causes hard and brittle regions, which leads to high strength but low ductility. To maintain good toughness, martensite should be avoided. A low percentage of carbon can help to prevent the formation of martensite. The addition of alloying elements to steel generally lowers martensite start temperature (M_s) and finish temperature (M_f).

With extremely high heat input, typical low toughness microstructures, such as upper bainite, martensite, and martensite-austenite-carbide (M-A-C) constituent, may form in the CGHAZ (Kim *et al*., 1991). Cooling rate is one of the important factors that determines the type of microstructure that forms in CGHAZ. Sundaram *et al.* (1987) found more martensite-type structure as well as acicular ferrite and a lower polygonal ferrite content in the HAZ obtained by using a lower heat input. Donald *et al.* (1952) studied the structure of the CGHAZ of low-carbon steel and they found that it contained a large proportion of pearlite with small ferrite grains. They also reported that Widmanstätten ferrite formed during an intermediate cooling rate. Similarly, Huang *et al*. (1994) reported that for SA516 Grade 70 steel, welded with a heat input of 4.5 kJ/mm, the main phase of the CGHAZ was Widmanstätten ferrite. Güral *et al*. (2007) reported that the microstructure of the HAZ near the fusion line contained coarse-grained polygonal ferrite and pearlite colonies.

2.3.3 Mechanical Properties

Increasing heat input can lead to increased productivity, but it can degrade the mechanical properties of the welded joint such as tensile strength and fracture toughness because high heat input slows the cooling rate and prolongs the cooling time of the weld metal, causing the grains to grow larger (Farrar and Harrison, 1987a). This is detrimental to the mechanical properties of the welded joint (Murray *et al*., 1996). Many researchers have studied the effect of heat input on the mechanical properties of welded joints. Their studies showed that an increase in heat input (or a decrease in cooling rate) reduced the toughness (Bhole and Billingham, 1983; Farrar and Harrison, 1987a; Sundaram *et al*., 1987; Moeinifar *et al*., 2011; Wang and Liu, 2002; Neves and Loureiro, 2004; Kim *et al*., 2005; Gharibshahiyan *et al*., 2011), hardness (Smith *et al*., 1989; Moeinifar *et al*., 2011; Neves and Loureiro, 2004; Yurioka *et al*., 1987; Gharibshahiyan *et al*., 2011) and tensile strength (Smith *et al*., 1989; Vercesi and Surian, 1998; Neves and Loureiro, 2004; Prasad and Dwivedi, 2008) of the welded joints. Optimum ductility and good toughness of the weld metal could be obtained by a microstructure consisting of mainly acicular ferrite (Lancaster, 1999; Dallam *et al*., 1985).

Bhole and Billingham (1983) reported that increasing heat input lowered the impact toughness for HSLA steel welds due to the formation of high temperature transformation products such as proeutectoid ferrite, side plate ferrite, and upper bainite. Farrar *et al*. (1974, 1987a, and 1987b) found that a high fraction of acicular ferrite was favorable in terms of toughness. However, the presence of martensite is considered to be

detrimental to toughness, as it could be a potential site for cleavage. Other unfavorable transformation products include polygonal ferrite, side plate ferrite, and aligned ferrite. These all have a larger grain size than acicular ferrite and may offer cleavage crack propagation paths (Farrar *et al*., 1974). Wang and Liu (2002) found that with 70% acicular ferrite and some coarse granular bainite (about 15%), the weld metal exhibited the best impact toughness property. An AF content of 80–90% in the as-deposited weld metal is necessary to obtain satisfactory toughness at low temperatures (Kim *et al*., 2005). The size of the HAZ gives an indication of its toughness and grain size. A high cooling rate (low heat input) would result in a narrow HAZ region, a fine grain size and, consequently, good toughness (Bhole and Billingham, 1983). Moeinifar *et al*. (2011) similarly reported that the toughness of the HAZ in X80 microalloyed pipe line steel decreased with increasing heat input. Very high cooling rates, however, would cause the formation of martensite or bainite, which lowers the toughness. Low cooling rates give rise to wide HAZ, large grain sizes, and inferior toughness (Moeinifar *et al*. 2011).

An increase in heat input caused a reduction of hardness in the WM and HAZ of steel RQT 601 because of microstructural changes and coarsening (Neves and Loureiro, 2004). With increasing heat input, the volume fraction of ferrite increased. Viano *et al*. (2000) found that coarsening of the ferrite phase took place by increasing heat input from 2 to 10 kJ/mm and, in turn, it reduced the hardness of the WM of SAW HSLA 80 steel. Yurioka *et al*. (1987) studied the hardness of the HAZ of different steels with carbon content varying from 0.05% to 0.73%. Their results showed that maximum hardness in the HAZ of all the steels decreased with increasing heat input. Moeinifar *et*

al. (2011) studied the influence of cooling rate on the hardness of the CGHAZ in SAW X80 steel and found that the increase in the fractional area of martensite/austenite particles due to high cooling rate (low heat input) was the main reason for the increase in the hardness of the CGHAZ.

Prasad and Dwivedi (2008) found that increased heat input and the resulting coarse-grained microstructure lowered the tensile and yield strengths of SAW HSLA steel. However, ductility was enhanced due to the coarsed grains. Neves and Loureiro (2004) reported similar results on SAW steel RQT 601. Vercesi and Surian (1998) also reported that tensile properties decreased with an increase in heat input for American Welding Society (AWS) A5.5-81 all-weld-metal.

2.3.4 Weld Bead Geometry

The relationship between heat input and weld bead geometry is complex because of the interrelationship between welding current, arc voltage and welding speed. In general, the size of the weld bead is proportional to the amount of heat input supplied. An increased energy supplied from the arc would promote both electrode and plate melting and thus produce a large weld bead. It is noted that only a portion of the heat input is used in melting the base metal and electrode, and some heat is lost through radiation, conduction, spatter and melting of the flux, or absorbed in the HAZ (Chandel, 1990).

Clark (1985) studied the weld bead geometry of manual metal arc welded Cr-Mo-V steel and found that the penetration area and reinforcement area were proportional to the

welding heat input. Lee *et al*. (2000) found that welding current had the greatest influence on the size of HAZ in SAW ASTM A36 steel with high currents causing a reduction in the size of the HAZ. Karadeniz *et al*. (2007) studied the effects of welding current, arc voltage and welding speed on the penetration of GMAW Erdemir 6842 steel. They showed that the depth of penetration increased linearly with both welding current and arc voltage. When welding speed increased, the penetration increased first and then decreased. However, the effect of welding current was approximately 2.5 times greater than that of arc voltage and welding speed on penetration. Farhat (2007) studied the effect of welding speed on the weld bead geometry on SAW API-5L X80 steel and the results showed that increasing the weld speed from 16.93 mm/s to 33.87 mm/s resulted in reductions in weld width, reinforcement, penetration depth, contact angle, deposition area, total area of the weld, and HAZ size in most of the weldments. Yang (2008) studied the effect of welding current and welding speed on the weld bead geometry on SAW SA516 and A709 steels and found that the reinforcement, penetration depth and HAZ size of SA516 and A709 welds increased with increasing welding current, but decreased with welding speed, the contact angle of SA516 and A709 welds decreased with increasing welding current and welding speed, and the bead width of SA516 and A709 welds decreased with travel speed but it was little affected by welding current.

To control the bead shape and weld metal chemistry, it is desirable to investigate the effect of the process variables on the electrode/plate/total melting efficiencies and dilution. Research has shown that process parameters of SAW such as welding current,

voltage, electrode diameter, electrode polarity and electrode extension have a considerable influence on the melting efficiencies of SAW and GMAW ASTM A36 steel (Chandel, 1990). Chandel (1990) showed that electrode melting efficiency increased with an increase in current and electrode extension, and with a decrease in arc voltage and electrode diameter. Plate melting efficiency of GTAW low carbon mild steel increased with increasing current and voltage (Chandel and Hang, 1996). Lee *et al*. (2000) also studied the melting efficiencies of SAW ASTM A36 steel and used the effect of welding parameters on the melting efficiencies to explain their effect on the HAZ size. Clark (1985) suggested that dilution was independent of the heat input but depended only slightly on the ratio of the bead width-to-bead height and strongly on the ratio of bead height to penetration depth. Palani and Murugan (2007) studied weld bead geometry of flux-cored arc welded (FCAW) IS: 2062 structural steel and showed that dilution slightly increased with an increase in welding current. All the works mentioned above are based on bead-on-plate welds.

Chandel *et al*. (1997) modelled the effect of welding current, electrode polarity, electrode diameter, and extension on the melting rate, bead height, bead width and weld penetration of SAW low carbon steel, using a constant heat input of 3.0 kJ/mm. Their results showed that bead height and weld penetration increased with an increase in welding current, while bead width decreased with it. Many other works (Benyounis and Olabi, 2008; Gunaraj and Murugan, 1999; Murugan and Gunaraj, 2005; Dhas and Kumanan, 2007; Juang and Tang, 2002; Kim *et al*., 2003; Nagesh and Datta, 2002; Rao *et al*., 2009; Palani and Murugan, 2007; Hrabe *et al*., 2009; Tarng and Yang, 1998)

using statistical and numerical approaches were carried out to predict and understand the effect of the welding parameters on the weld bead geometry.

2.4 Fatigue Properties of Welded Joints

Welded joints used in some practical applications, such as wind turbine towers, pressure vessels, and bridges, usually experience cyclic loads which may lead to fatigue failure. As such, fatigue properties should be taken into account in the design of welded structures.

Although the properties of the weld metal are good, fatigue problems can be caused when there is an abrupt change in the component, such as excessive reinforcement, undercut, slag inclusion and lack of penetration. It was reported that nearly 70% of fatigue cracking in industries occurs in the welded joint (Magudeeswaran *et al*., 2009). Welding process, filler metal, heat input and the number of weld passes will affect the mechanical properties, microstructure, weld bead geometry and discontinuities of the welded joints and, in turn, influence its fatigue properties (Gurney, 1968; Magudeeswaran *et al*., 2009).

2.4.1 Effect of Microstructure on Fatigue Properties of Welded Joints

The fatigue strength of metals usually increases with increasing tensile strength. However, for a given tensile strength, it is dependent to some extent on the microstructure of the metal (Forrest, 1962). The weld microstructure, especially the dendrite alignment, significantly affects the fatigue crack growth (Jang *et al*., 2010).

Jang *et al*. (2010) showed that fatigue cracks followed mostly the directions of austenite/ferrite boundary in 316L steel welds.

Forrest (1962) studied the influence of microstructure on the fatigue strength of steels and suggested that the low fatigue resistance of mixed microstructures may be attributed to coarse pearlite, free ferrite or retained austenite. The presence of about 10% of retained austenite reduced the fatigue strength of high strength steels (at 10^5 cycles) by 10-15%, but greater quantities had little effect (Forrest, 1962). Breen and Wene (1978) investigated the influence of microstructure on the fatigue properties of steels and the results are summarized in Figure 2.5. The σ_n/σ_u (fatigue limit or endurance limit / ultimate strength) ratios were approximately 0.5. The best fatigue properties were obtained with tempered martensite. When untempered martensite was included, the σ_n/σ_u ratio dropped to between 0.26 and 0.30.

2.4.2 Effect of Weld Geometry on Fatigue Properties of Welded Joints

Gurney (1968) demonstrated the importance of reinforcement shape to fatigue property by comparing the fatigue strength of butt-welded joints of steels with different contact angles (θ). In test, both the width (W) and the height (H) of the reinforcement were varied but the ratio H/W was maintained constant, which implied constant reinforcement angle (θ) and constant fatigue strength. However, by keeping W constant and varying H, fatigue strength was found to decrease as H increased (or as θ decreased). In view of the influence of weld reinforcement in determining fatigue strength, it became clear that a

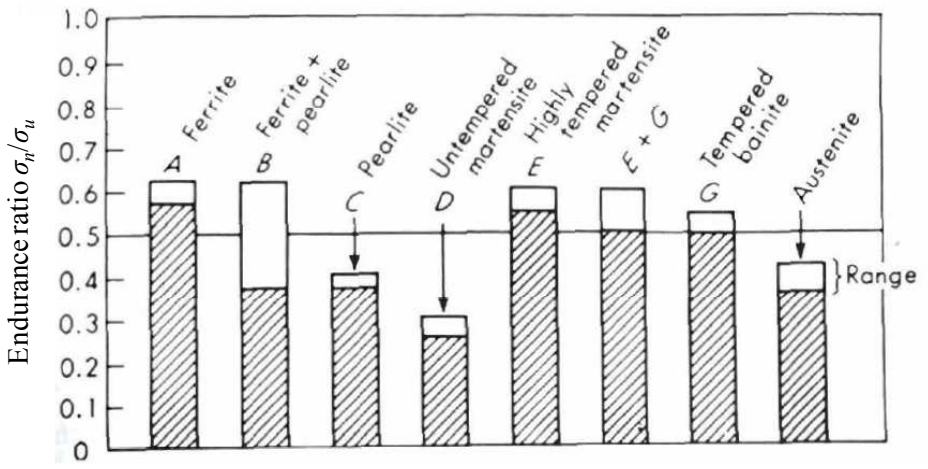

Figure 2.5. Effect of microstructure on endurance ratio for steel (Breen and Wene, 1978).

simple method of improving fatigue performance was to machine the reinforcement flush with the plate surface (Gurney, 1968).

Ninh and Wahab (1995a) studied the effect of weld geometry parameters on the fatigue properties of butt-welded joints of structural steels using finite element analysis (FEA). Their analysis showed that fatigue life and fatigue strength of the welded joints can be improved by modifying the reinforcement shape, including increasing the radius of weld toes and increasing the contact angle. Ninh and Wahab (1995b) also developed an analytical model to determine the effect of residual stresses and weld geometry on fatigue life of structural steels. They found that the fatigue life of the welded joint was substantially increased as the weld toe radius increased from 0.3 mm to 2.0 mm or as the contact angle increased from 160^o to 180^o. Ninh and Wahab (1998) later studied the fatigue strength and fatigue life of butt-welded joints of structural steels using FEA and found that fatigue strength and fatigue life were improved by either partly or totally eliminating the weld toe undercut. They also found that the fatigue strength at 2×10^6

cycles was increased 12% as the tip radius of undercut was decreased from 0.35 to 0.05 mm. In another study, Radhi and Barrans (2010) used finite element method to investigate the effects of weld toe radius on fatigue life of a butt-welded joint of S355JR steel. Weld toe radius contributes to stress concentration; increased weld toe radius reduces the stress concentration. It was reported that the fatigue life was increased 2.2 times as weld toe radius was tripled from 0.44 mm to 1.2 mm. Lee *et al*. (2009) experimentally demonstrated similar results for mild carbon steel that fatigue life increased with an increase in the contact angle and the weld toe radius.

2.4.3 Effect of Weld Defects on Fatigue Properties of Welded Joints

Welded structures generally contain built-in defects, such as lack of penetration, slag inclusion, porosity and misalignment. When these structures are subjected to the cyclic loading, fatigue crack might initiate from these defects, which could cause a reduction in fatigue strength between about 55% and 65% (Gurney, 1968).

A moderate degree of porosity, slag or lack of fusion in a weld does not reduce the fatigue strength (Newman, 1959). Onoro and Ranninger (1997) investigated the fatigue behavior of laser welds of HSLA steels and found that rough porosity in the fusion zone did not promote fatigue crack-initiation start points. Gurney (1968) reported that a lack of penetration defect severity over 1% could not be tolerated (only valid for the size of specimen used in laboratory investigation). Cicero *et al*. (2009) studied the lack of penetration defects in circumferential butt welds of tubular towers, in which fatigue properties were considered. They suggested that the maximum tolerable lack of

penetration defects was of the dimension of 2.9 mm for the wind tower with thickness of 35 mm. Fazzini *et al*. (2007) studied a 45 year-old gas pipeline which had a blowout due to sudden propagation of a pre-existing longitudinal crack at the double submerged arc seam weld. They found that fatigue cracks had propagated from a large embedded weld defect of lack of fusion to the surface of the pipeline.

Stress raisers on the surface of welded joints, such as undercut and excessive reinforcement, are frequent sources of fatigue cracks. Fatigue life and fatigue strength of butt-welded joints can be improved by decreasing the tip radius of weld undercut or eliminating it entirely (Ninh, 1995a).

2.4.4 Effect of Heat Input on Fatigue Properties of Welded Steel Joints

As discussed in Section 2.3, welding heat input affects the microstructure, hardness, toughness, tensile properties, and weld bead geometry of welded joints. These properties will, in turn, influence fatigue properties of the welded joints. However, there is dearth of information in the open literature on the effect of the heat input on the fatigue properties of welded steel joints.

2.4.5 Effect of Low Temperature on Fatigue Properties of Welded Joints

In cold regions of the world, welded structures such as bridges and wind towers work in the climatic temperature range of +20 to -60 °C (Kobrin *et al*., 1971). In general, these structures are fabricated of low-carbon structural steels rather than steels designed for

low temperature services. From a viewpoint of safety, it is necessary to study the fatigue behavior of welded joints at sub-zero temperatures.

Only a few studies of the effect of low temperature on fatigue properties of steels exist in the open literature (Forrest, 1962; Frost *et al.*, 1999; Verkin *et al*., 1983; Stephens *et al*, 2001; Shul'ginov and Matveyev, 1997). Forrest (1962) found that the fatigue strength of various steels increased with a reduction in temperature (see Table 2.1). The fatigue strengths of these steels were higher at -40 °C and -78 °C than at room temperature. The tensile strength also increased with a decrease in temperature, but not to the same extent as the fatigue strength. The increase in fatigue strength with decreasing temperature was usually greater for low-hardness materials than hard ones and was particularly appreciable for mild steel. Shul'ginov and Matveyev (1997) carried out fatigue testing of low-alloy steels and their butt-welded joints under the conditions of impact and sinusoidal loading at -60 °C and room temperature. They found that with a drop in temperature from room temperature to -60 °C, the fatigue strength of both base material and welded specimens increased under sinusoidal loading, but decreased under impact loading.

Although, almost without exception, the fatigue strength of a few steels was reported to generally increase at low temperatures (Forrest, 1962; Frost *et al.*, 1999), it is worth investigating the low temperature fatigue properties of ASTM A 709 Grade 50 steel and its welds in order to ensure that fatigue failures will not occur at such temperatures.

Table 2.1. A comparison of fatigue strengths at low temperatures with fatigue strengths at room temperature (Forrest, 1962).

Material	Average value of the ratio: $\frac{\text{Fatigue limit at low temperature}}{\text{Fatigue limit at room temperature}}$		Average value of the fatigue limit ratio: $\frac{\text{Fatigue limit}}{\text{Tensile strength}}$		
	-40 °C	-78 °C	Room temperature	-40 °C	-78 °C
Carbon steels	1.20	1.30	0.43	0.47	0.45
Alloy steels	1.06	1.13	0.48	0.51	0.48
Cast alloy steels	-	1.22	0.27	-	0.27
Stainless steels	1.15	1.21	0.52	0.50	0.57

CHAPTER 3

MATERIALS AND EXPERIMENTAL PROCUDURES

This chapter provides a description of the materials, welding process, and experimental procedures used in the research. All the welding operations were carried out by certificated welders of Hitachi Canadian Industries (HCI) Ltd., Saskatoon, Saskatchewan. Various difficulties were encountered during the testing, but the major challenge was conducting fatigue testing under sub-zero temperatures. The methods used for these tests are described in Section 3.3.6.

3.1 Material

The structural material studied in this research was ASTM A709 Grade 50 steel. It was supplied as normalized plates measuring 500 mm × 250 mm × 20 mm by HCI. The chemical composition of A709 steel shown in Table 3.1 was given in the mill test report (MTR) provided by HCI. The accuracy of the chemical composition values was verified internally using the PERKIN ELMER ELAN 5000 inductively coupled plasma mass spectroscopy (ICP-MS) facility located in Room 211, Geology Building, University of Saskatchewan, and the results are also presented in Table 3.1.

Table 3.1. Chemical composition of ASTM A709 Grade 50 steel (wt. %).

Element	C	Mn	P	S	Si	Cu	Ni
ICP-MS	N/A	1.3156	N/A	N/A	N/A	0.1703	0.0699
MTR	0.07	1.44	0.013	0.006	0.3	0.2	0.07
Element	Cr	Mo	Al	V	Nb	Ti	Ca
ICP-MS	0.1266	0.0122	0.0396	N/A	0.0529	N/A	N/A
MTR	0.12	0.01	0.028	0.007	0.047	0.003	0.0001

The filler wire used was 4.0 mm ESAB Spoolarc 81 (American Welding Society (AWS) EM12K) while the flux was ESAB OK 10.72 (AWS F7A6-EM12K-H8). The as-supplied chemical compositions of the filler rod and flux are given respectively in Tables 3.2 and 3.3.

3.2 Welding Procedure and Parameters

The edges of the A709 steel plates to be welded were first double-beveled as shown in Figure 3.1. Then, they were submerged arc welded using an ESAB CaB 300 welding machine (Figure 3.2) operated by HCI personnel. The welding parameters used are shown in Table 3.4. Identical heat inputs were used to weld one side of the plates, while four different heat inputs were used for the second side. A single pass was used for each side of all plates. Single-wire welding was used for the first side of all coupons (i.e., T1, T2, T3 and T4) and the second side of coupons T1 and T2, while tandem welding was used for the second side of coupons T3 and T4.

Table 3.2. Chemical composition of welding wire AWS No. EM12K.

Elements	C	Mn	Si	S	P	Cu	Others
wt.%	0.10	0.99	0.24	0.01	0.006	0.13	<0.50

Table 3.3. Chemical composition of flux ESAB 10.72.

Elements	SiO_2+TiO_2	CaO+MgO	Al_2O_3+MnO_2	CaF_2
wt.%	20	25	30	20

Table 3.4. SAW parameters used for A709 Grade 50 steel plates.

Plate ID	No. of Passes	Welder polarity	*I* (A)	*V* (V)	*S* (mm·s^{-1})	HI (kJ·mm^{-1})	Total HI (kJ·mm^{-1})
T1	1st side	DC	750	31.0	8.04	2.75	2.75
	2nd side	DC	800	32.1	8.04	3.03	3.03
T2	1st side	DC	750	31.0	8.04	2.75	2.75
	2nd side	DC	900	34.0	8.47	3.43	3.43
T3	1st side	DC	750	31.0	8.04	2.75	2.75
	2nd side	DC AC	800 700	33.0	11.43	2.19 1.92	4.11
T4	1st side	DC	750	31.0	8.04	2.75	2.75
	2nd side	DC AC	900 750	34.5	11.85	2.49 2.07	4.56

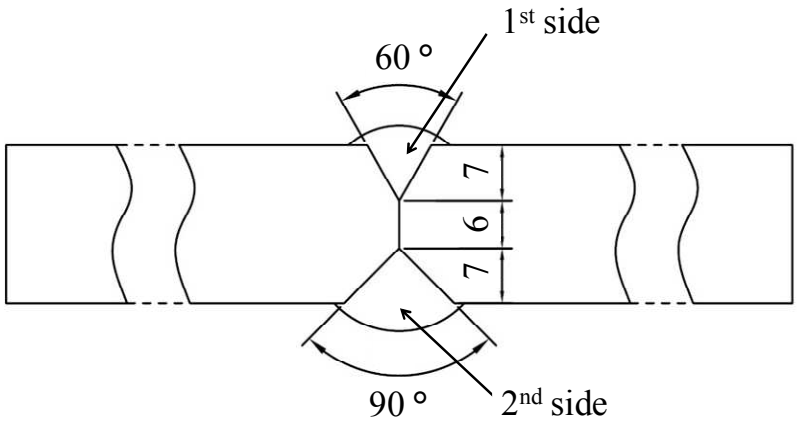

Figure 3.1. Joint geometry of weld coupons. (All dimensions in mm)

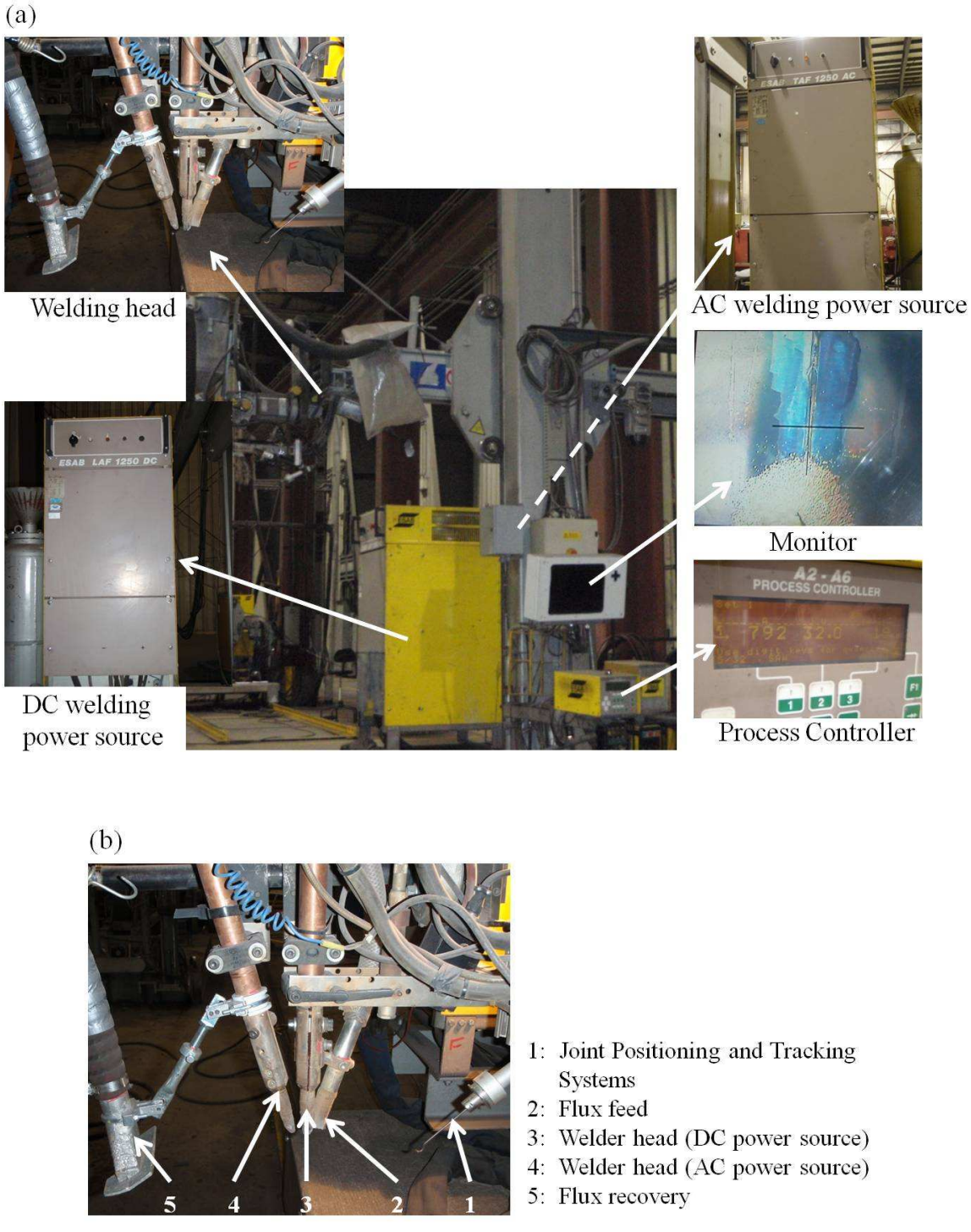

Figure 3.2. The SAW welding machine: (a) ESAB automatic welding machine and (b) components of the welding head.

3.3 Experimental Methods

Ultrasonic testing was carried out to screen the welded coupons. Weld geometry measurements, microhardness measurements, tensile and fatigue testing were performed to investigate properties of A709 Grade 50 steel and its weldments. Optical microscopy and scanning electron microscopy (SEM) were used to study the weld microstructures and the fractured surfaces of tensile and fatigue specimens.

3.3.1 Ultrasonic Testing

Surface defects such as undercut, cracks, and burn-through were visually inspected. Internal defects in the weldements, specifically the weld metal and the adjacent parent metal 2 mm on each side of the weld, were examined by HCI quality assessment inspector, with a Krautkramer USN 52L ultrasonic flaw detector (Figure 3.3(a)) using a 70^{o} transducer (Figure 3.3(b)) and Ultra Gel II couplant.

3.3.2 Metallographic Examination

The microstructures of the PM, FGHAZ, CGHAZ, WI, and WM zones of A709 Grade 50 welds were studied by metallographic examination. All the specimens used for metallographic examination were first ground using emery papers of different grit sizes and subsequently polished using 1 μm diamond paste on a nylon cloth followed by etching in 2% Nital solution. The microstructures of the specimens were observed using

Figure 3.3. (a) Krautkramer USN 52L ultrasonic flaw detector and (b) 70^{o} transducer.

a Nikon MA100 optical microscope equipped with PAX-it image analysis software (Figure 3.4), which is located in Room 2C26, Engineering Building, University of Saskatchewan. Using the area calculation of PAX-it, the proportion of ferrite and pearlite within the PM as well as the fraction of acicular ferrite and grain boundary ferrite within the WM can be estimated.

3.3.3 Weld Bead Geometry Measurements

A schematic diagram of an unbeveled, gapless submerged arc welded butt joint showing important physical parameters is used to describe the weld bead geometry and HAZ, and is shown in Figure 3.5. The parameters are the bead reinforcement (R), bead width (W), penetration depth (P), HAZ size (H), bead contact angles (θ_1 and θ_2), deposition area (A_d) that represents the portion of the WM contributed by the electrode, penetration area (A_p) that represents the proportion of the WM resulting from the melting of the base metal, and total molten area (A_t) (= A_d+A_p). These parameters are greatly affected by welding current, welding speed, and arc voltage, three of which control the heat input to a weld.

Figure 3.4. Nikon MA100 optical microscope equipped with software PAX-it.

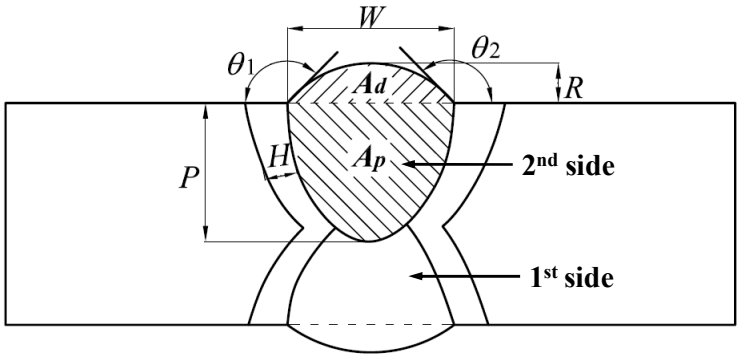

Figure 3.5. A schematic diagram of a typical SAW welded butt joint with no bevel or gap.

To ensure consistency of measured data, locations on the welds with severe surface defects such as burn-through and excessive reinforcement were avoided. After eliminating these defective sections of the plates, three transversely sectioned test specimens were cut at random from each plate. They were grounded using different grades of emery cloth and polished with 1 μm diamond paste, and then etched with 2%

nital solution to reveal the microstructure of the PM, WM and HAZ regions. They were examined using a Nikon MA100 inverted optical microscope. Digital images of the etched specimens were acquired and imported into the PAX-it image analysis software for calibration and subsequent weld bead geometry measurements. Since the welded joints studied in this work were bevelled but without a gap, the bead parameters A_d and A_p did not apply directly in calculating % dilution and melting efficiencies. Instead, areas A_d' and A_p' illustrated in Figure 3.6 were used for the calculations. Typical cross-sections of A709 steel welds prepared using different heat inputs are shown in Figure 3.7. Since the first sides of the welds were prepared using the same heat input only, the data measured from the second sides of the plates are reported here as they were welded using different heat inputs.

3.3.4 Hardness Measurements

Hardness measurements were carried out on polished and etched welded specimens using a Mitutoyo MVK-H1 Vickers microhardness tester (see Figure 3.8) , which is located in Room 2C26, Engineering Building, University of Saskatchewan. To measure the hardness, the indenter was pressed into the surface of the specimens using a load of 500 g and a resident time of 15 seconds. A measurement whose diagonal length values differed by more than 5μm was discarded to avoid excessive fluctuation. Transverse hardness readings were taken across the PM, FGHAZ, CGHAZ and WM, on both passes as shown in Figure 3.9. At least 15 readings were taken in each region. So, the hardness data reported in this thesis are averages.

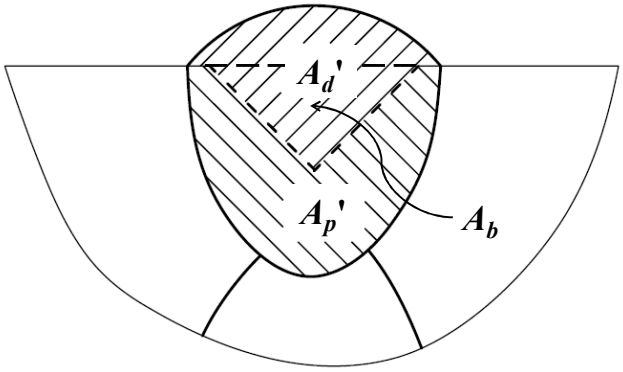

Figure 3.6. A schematic diagram showing deposition and penetration areas of a welded joint with bevel.

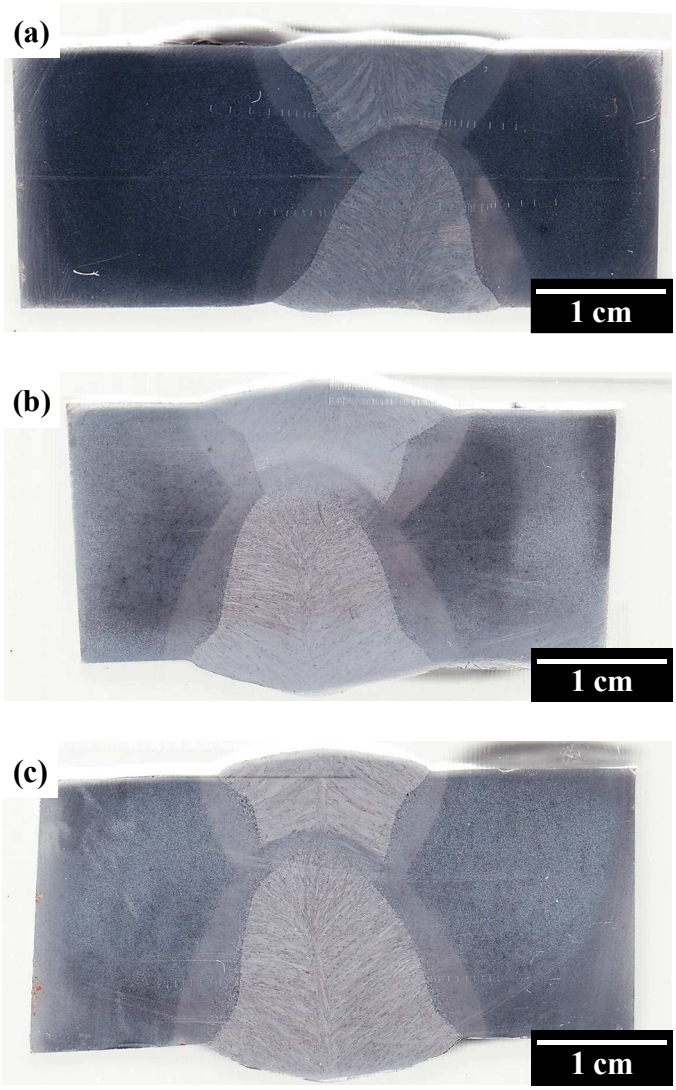

Figure 3.7. Typical cross-sections of A709 steel welds prepared using different heat inputs: (a) T1, (b) T2, (c) T3, and (d) T4.

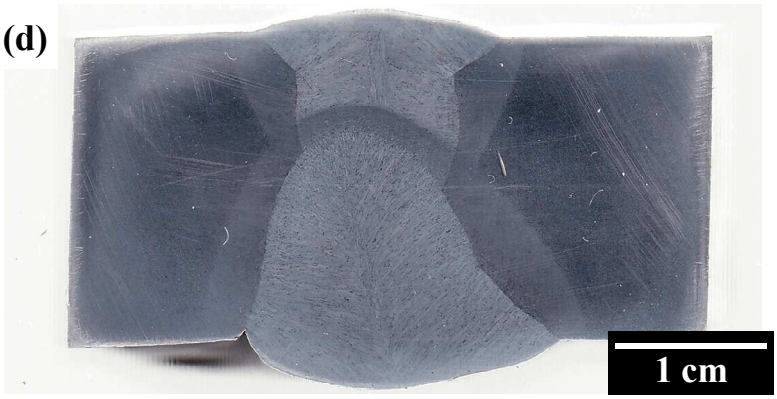

Figure 3.7 continued.

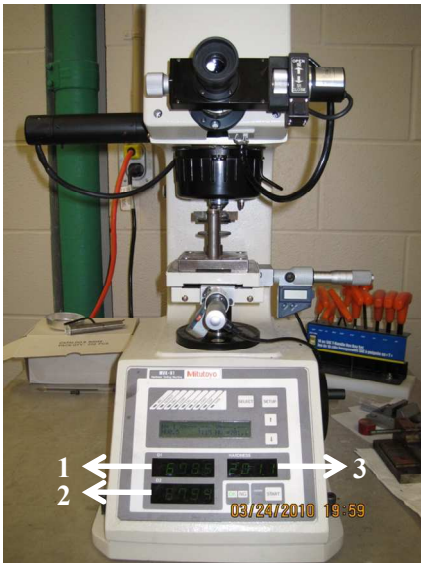

1: diagonal length value 1;
2: diagonal length value 2;
3: Vickers hardness number.

Figure 3.8. Mitutoyo MVK-H1 Vickers testing machine.

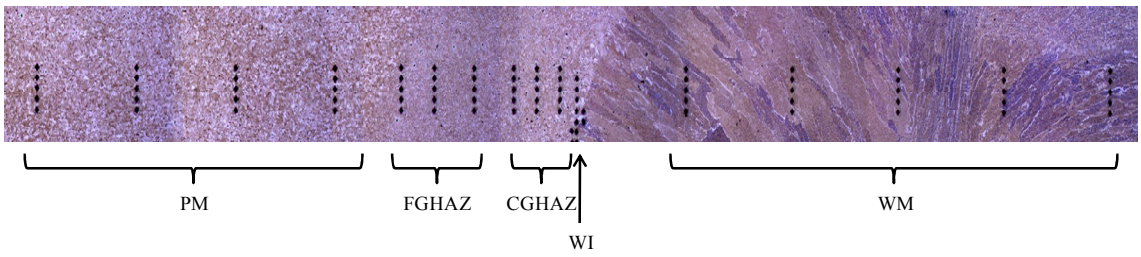

Figure 3.9. Locations of hardness measurements on the weldment.

3.3.5 Tensile Testing

Tensile tests were performed at room temperature using a computer-controlled Instron™ Universal Testing Instrument, Floor model 5500R, interfaced with a Bluehill software (Figure 3.10), which is located in Room 1A89, Engineering Building, University of Saskatchewan. The applied cross-head speed was 5 mm/min and the initial strain rate was 0.098 /min. A 50.8 mm extensometer was used to measure the extension of the specimens during testing. Stress vs. strain curves were obtained by the Bluehill software. Mechanical properties such as tensile strength, yield strength, tensile strain at maximum load, and Young's modulus were determined automatically by the software. The gauge length of each specimen was measured before and after testing and percent elongation was calculated. The tensile strength results were also used to estimate the fatigue limit because fatigue limit of carbon steels is 50% to 60% of the tensile strength (Dowling, 1999).

Tensile test specimens were prepared according to ASTM A370 standard (2009). Figure 3.11 shows the dimensions of a typical tensile test specimen. Specimens cut from the PM and welded plates were tested. Three longitudinal and three transverse specimens were machined from the PM in order to ascertain the effect of rolling directions on the tensile properties. Three specimens were tested for each heat input and parent metal. Specimens were cut from the welded plates perpendicular to the weld bead direction as shown in Figure 3.12. The specimens were also etched with 5% Nital solution after testing to reveal the WM and HAZ zones and to determine where they broke.

Figure 3.10. Instron™ Universal testing machine, Floor model 5500R, interfaced with a Bluehill 5500 system.

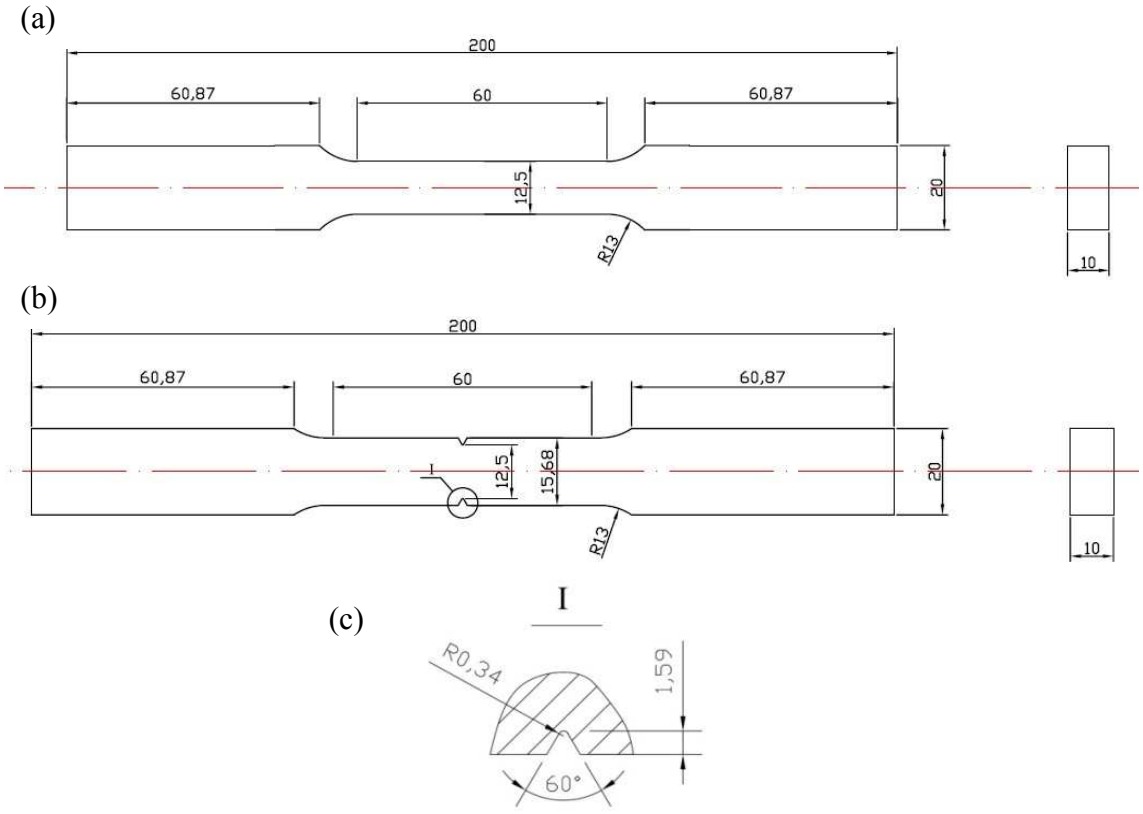

Figure 3.11. Tensile test specimens: (a) dimensions of unnotched for parent and welded metals, (b) dimensions of notched for parent metal only, and (c) dimensions of V-notch. (All dimensions in mm)

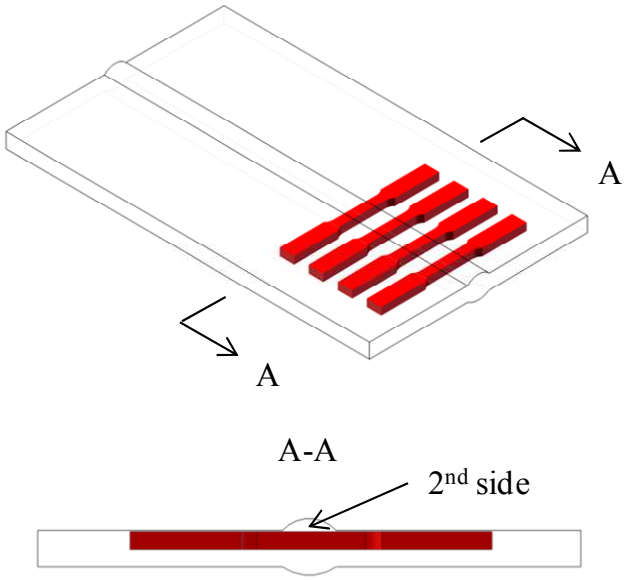

Figure 3.12. Machining of tensile specimens.

3.3.6 Fatigue Testing

There are three major approaches to analyzing fatigue failures, namely: stress-based approach, strain-based approach and fracture mechanics approach (Dowling, 1999). To study the fatigue strength of ASTM A709 Grade 50 steel and its welds, the stress-based fatigue life method was used for this project. Stress-life relations are used mainly to assess high cycle fatigue and to model the initiation of fatigue cracks (De Jesus *et al.* 2007). The stress-based approach to the fatigue analysis works well for situations in which only elastic stresses and strains are present (Lee *et al.*, 2005).

Fatigue specimens were machined in accordance with ASTM Standard E466 (2007). Figure 3.13 shows unnotched parent metal and welded specimens used in fatigue testing and their dimensions. The fatigue specimens from the welded plates were cut perpendicular to the weld bead direction as shown in Figure 3.14. All the welded fatigue

(a)

(b)

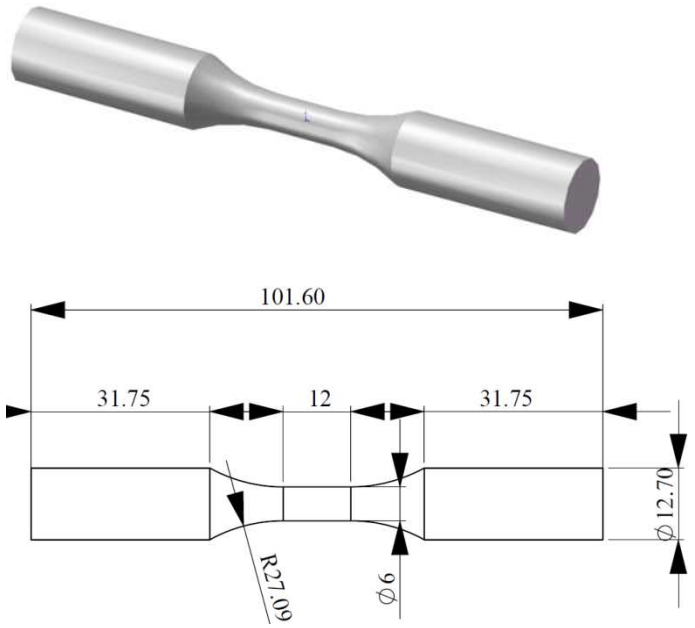

Figure 3.13. Fatigue specimen: (a) unnotched parent & welded metals specimen and (b) dimensions of unnotched specimen. (All dimension in mm).

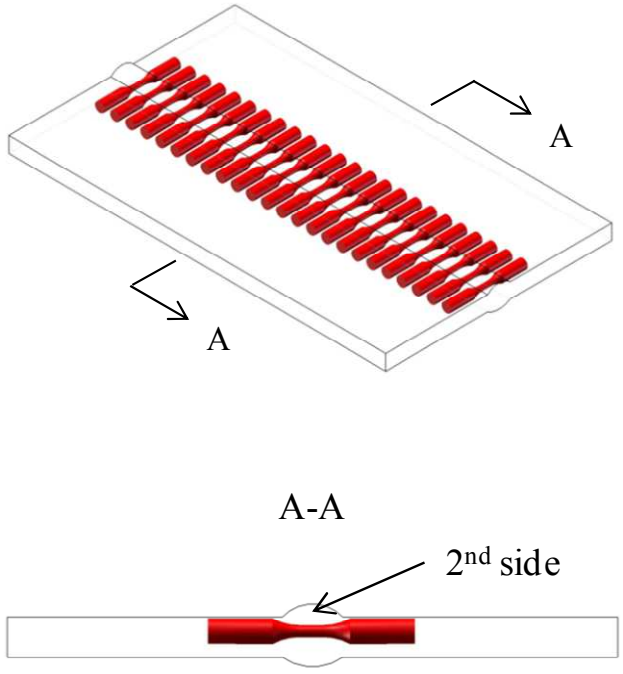

Figure 3.14. Fatigue specimen machining.

specimens were machined from the second side (the side which the heat input varied) of the welded plates and included the WM, HAZ and PM.

Stress concentration is one of the most important factors affecting the fatigue life of any component or structure. The tensile strength of a butt-welded joint is generally not less than that of the base material. Fatigue cracking of a good welded joint usually initiates from the teo of the weld bead, which has high stress concentration (Frost, 1999). Stress concentration of the welded joints is caused by the weld bead shape (e.g., reinforcement) and exists in weld defects (e.g., undercut and internal cavities that may not be detected by non-destructive inspections). To apply fatigue analysis to the welds, an appropriate value of the stress concentration factor needs to be selected. In this study, circumferential V-notches were made in the middle of the cylindrical fatigue test specimens to introduce stress concentration (K_t = 2.25) which closely represents actual butt-welded joints (K_t = 2.58). Calculations of stress concentration factors (K_t) for butt-welded joints and V-notched cylindrical specimens are summarized in Appendices A1 and A2. Notched specimens used in the fatigue testing and their dimensions are shown in Figure 3.15. The dimensions of the V-notch of the fatigue specimens were the same as those of the tensile specimens as shown in Figure 3.11 (c) except that the depth of the V-notch of the fatigue specimens was 1 mm. Only parent metal fatigue specimens were notched due to the limitation imposed by the number of welded plates supplied.

(a)

(b)

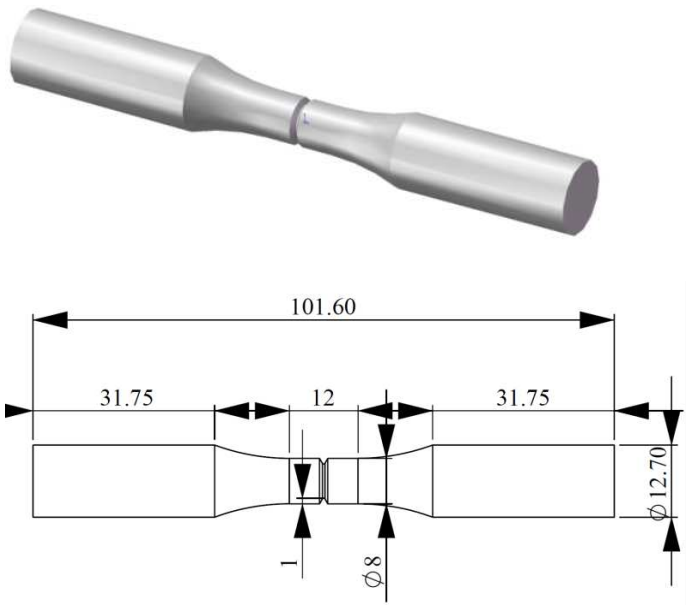

Figure 3.15. Fatigue specimen: (a) notched specimen and (b) dimensions of notched specimen. (All dimension in mm).

To investigate the fatigue properties of ASTM A709 Grade 50 steel and its welds, specimens were subjected to cyclic loading conditions to induce fatigue failure. A Krouse rotating cantilever beam machine (see Figure 3.16), located in Room 2C19, Engineering Building, University of Saskatchewan, was used to perform the fatigue testing by producing alternating tensile and compressive stresses. Cylindrical fatigue specimens were clamped into the Krouse machine using a set of two freely rotating collets. One of these collets was connected to a DC motor, while the other was connected to a load arm. Using a sliding weight, a moment was applied to the specimen at the end of the load arm. The bending moment was related to the applied stress (equation 3.1) and was calculated by equation 3.2.

$$\sigma = \frac{32M}{\pi d^3} \tag{3.1}$$

Figure 3.16. Krouse rotating cantilever beam machine.

$$M = \frac{\pi \sigma d^3}{32} \tag{3.2}$$

where M is the bending moment and scale beam reading in inch pounds, d the diameter of the specimen, and σ the desired stress. To convert the unit to N·m, the value of M was divided by 8.85666. σ is the bending stress at the minimum section of the specimen in Pa. d is the diameter of the minimum section of the specimen in m. Therefore, the maximum and minimum stresses for a cyclic loading could be determined by:

$$\sigma_{\max} = \frac{32M}{8.85666\pi d^3} \tag{3.3}$$

$$\sigma_{\min} = -\frac{32M}{8.85666\pi d^3} \tag{3.4}$$

The stress amplitude (σ_a) is given by (Dowling, 1999)

$$\sigma_a = \frac{\sigma_{\max} - \sigma_{\min}}{2} = \frac{32M}{8.85666\pi d^3} \tag{3.5}$$

This study investigated the fatigue property of ASTM A709 Grade 50 steel at -20 ^{o}C and -30 ^{o}C. To obtain -20 °C and -30 °C, the first method tried was to design an insulated chamber surrounding the specimen part of the fatigue machine and inlet cold air into the chamber. However, the lowest temperature that could be reached inside the chamber was only -5 °C because the supply of cold air was not enough and cold leaked away through the load arm which was connected to the specimen. The second method was to place the whole fatigue machine in a temperature-controlled cold room (Room 1B30) in Engineering Building, University of Saskatchewan. Fatigue testing at -20 ^{o}C was conducted successfully. However, other practical problems arose during testing at -30 ^{o}C, either the motor or the weight got frozen once the testing was carried out at -30 °C. So, I was able to successfully test only one or two fatigue specimens at each stress amplitude level at -30 °C. Specimens and loading conditions were the same for both room temperature and low temperatures testing.

3.3.7 Fractography

The fracture surfaces of tensile and fatigue specimens were examined in a Hitachi TM3000 scanning electron microscope (SEM) and a JEOL JSM-6010LV SEM. The secondary electron detector was used in the SEMs to provides information about surface topography. The fracture surfaces of fatigue specimens were also examined in an Ancansco Stereomicroscope (Serial number: OT6850, located in Room 2C25,

Engineering building, University of Saskatchewan) interfaced with a QCapture Pro 6.0 software. Valuable information regarding the mechanism and nature of the fracture, such as fatigue striations and inclusions, were obtained through this examination.

CHAPTER 4

RESULTS AND DISCUSSION

The results obtained from the various experiments described in Chapter 3 are presented and discussed in this chapter. The analysis of the results show the effect of heat input on microstructure, weld bead geometry, hardness, tensile and fatigue properties of ASTM A709 Grade 50 steel welds.

4.1 Effect of Heat Input on Microstructures of ASTM A709 Grade 50 Steel Weld

A typical optical macrograph of submerged arc welded (SAW) ASTM A709 Grade 50 steel joint is shown in Figure 4.1. The three usual zones of the welded joint, i.e., the parent metal (PM), heat-affected zone (HAZ) and weld metal (WM) are clearly shown and demarcated with distinct boundaries. Figure 4.2 shows typical optical micrographs obtained from the different weld zones of SAW A709 Grade 50 steel joint produced using a heat input of 3.43 kJ/mm. The microstructure of PM shown in Figure 4.2 (a) was characterized by two microconstituens: ferrite (light etched) and pearlite (dark etched). The fraction of ferrite and pearlite was calculated using the area calculation module of PAX-it image analysis software. The results showed that there was about 7% pearlite and 93% ferrite in the PM. Using the inverse lever rule, the carbon content of A709 steel

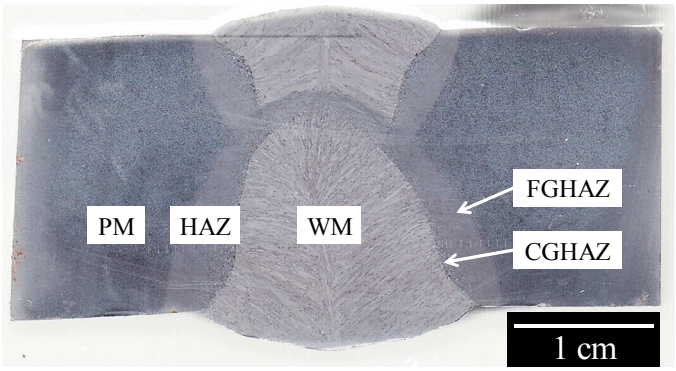

Figure 4.1. Typical weld zones of SAW welded A709 Grade 50 steel.

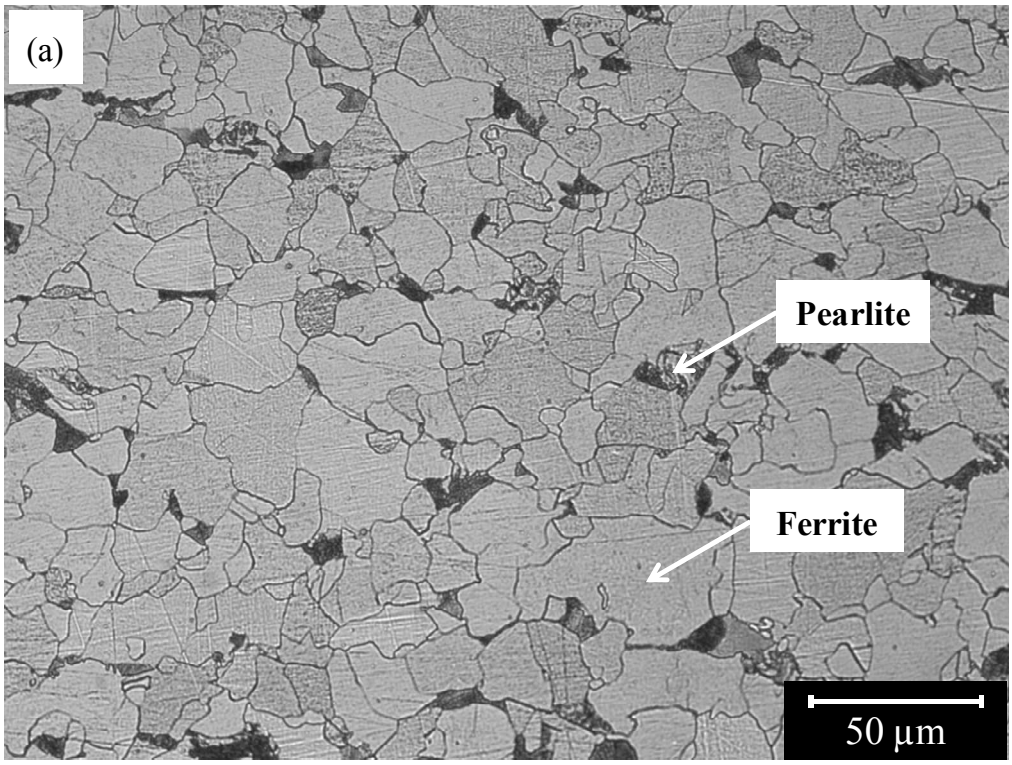

Figure 4.2. Typical microstructures obtained from different weld zones of SAW welded A709 Grade 50 steel joints produced using a heat input of 3.43 kJ/mm: (a) PM, (b) FGHAZ, (c) CGHAZ, (d) and (e) WM.

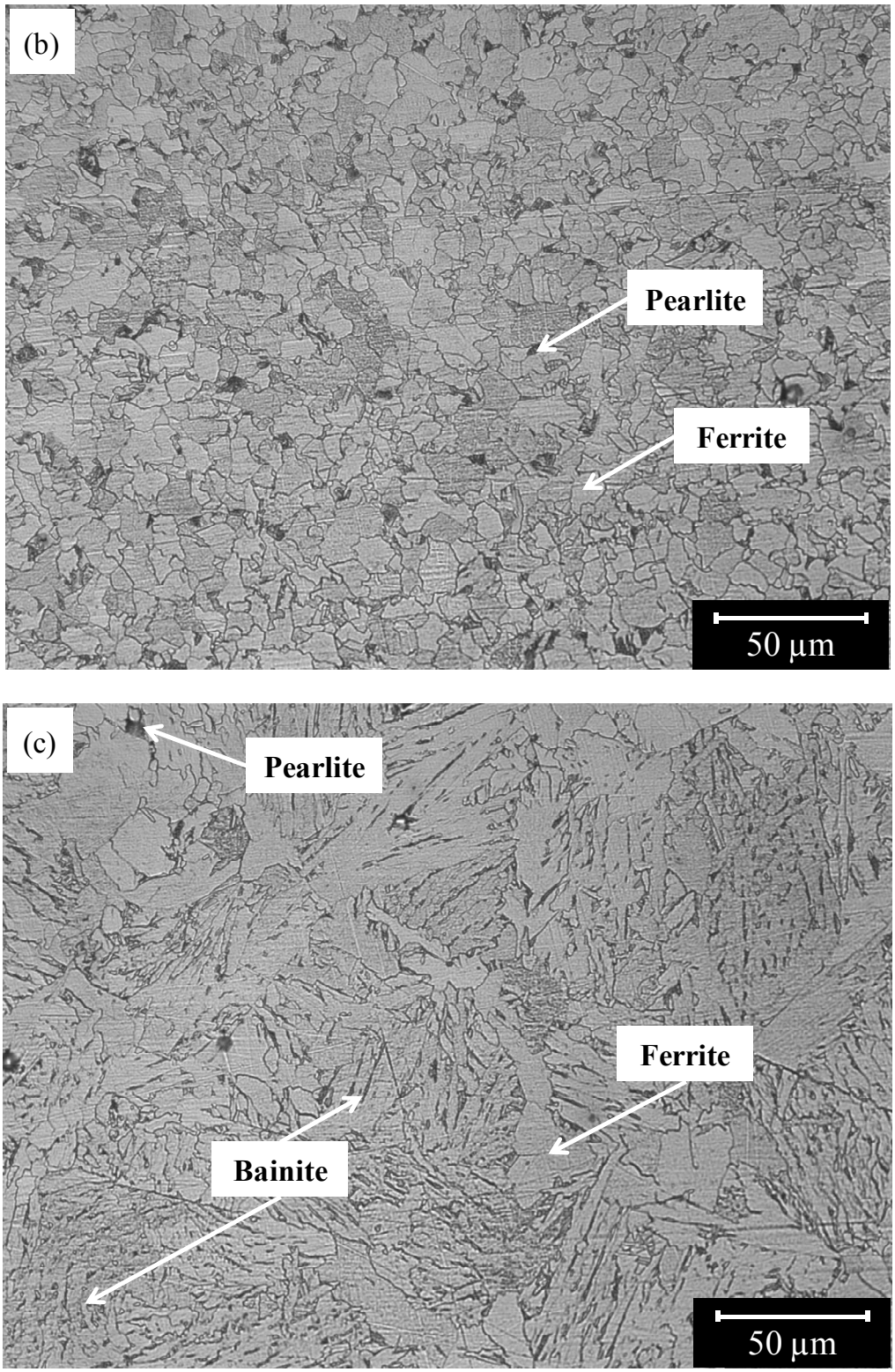

Figure 4.2 continued.

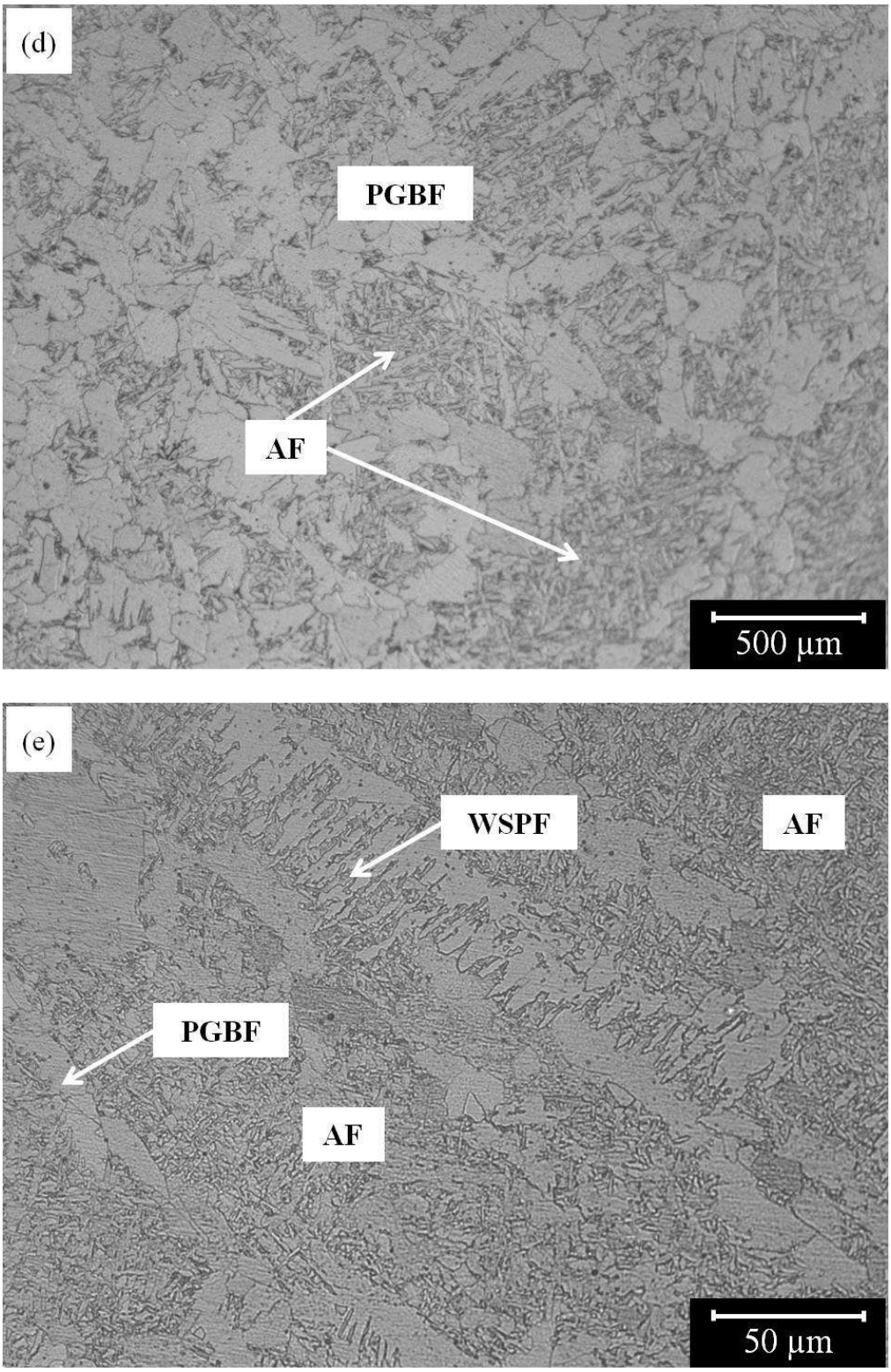

Figure 4.2 continued.

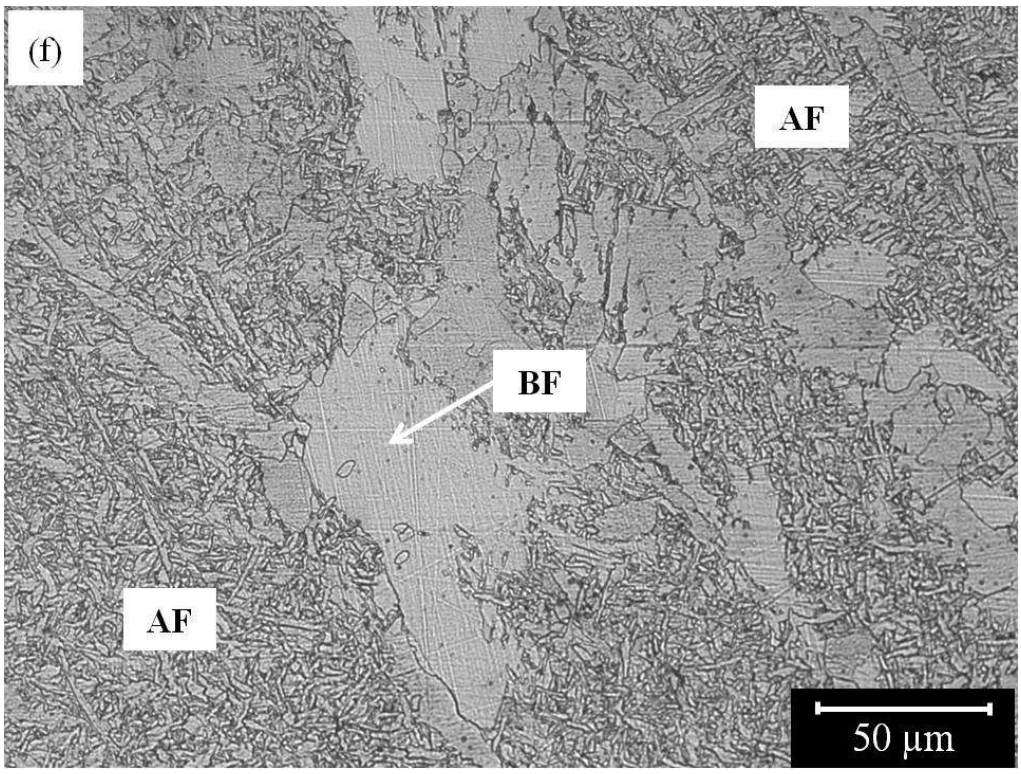

Figure 4.2 continued.

was determined to be 0.074%, which is close to the value of 0.07% given in the MTR (Table 3.1). The microstructure of the fine-grained heat-affected zone (FGHAZ) shown in Figure 4.2 (b) was also characterized by ferrite and pearlite. However, the grains in this zone were much finer than those in PM because they reached the temperature (700 – 950 °C) where the grain refinement occurred. The microstructure of the coarse-grained heat-affected zone (CGHAZ) shown in Figure 4.2 (c) and (d) was obtained near the weld interface and consisted of bainite, ferrite, pearlite and acicular ferrite (AF). No martensite was found in the CGHAZ possibly due to the very low carbon content of the parent steel. In the WM shown in Figure 4.2 (e) and (f), the principal microstructures were AF, polygonal grain boundary ferrite (PGBF), block ferrite (BF), and

Widmanstätten side plate ferrite (WSPF). AF was formed intragranularly, which results in randomly oriented short ferrite needles (Dallam *et al*., 1985). This interlocked nature as well as the fine grain size of the AF accounts for high toughness of the WM. Grains in the WM are mostly of coarse columnar structures and grow in a direction perpendicular to the WM/HAZ interface since this is a direction of the maximum temperature gradient and thus the maximum driving force for the solidification (Kou, 1987). Figure 4.3 shows SEM micrographs of the WM and HAZ of as-polished welded joint. Inclusions (indicated by arrows) were observed.

Figure 4.4 shows optical micrographs of WMs of SAW A709 Grade 50 steel joints produced using different heat inputs. Comparing these micrographs, it can be seen that the largest grains were obtained in the WM that was produced using the highest heat input. Figures 4.5 and 4.6 show the proportions of AF and GBF within the WMs, respectively. As can be seen from Figures 4.5 and 4.6, the high heat input appeared to slightly reduce the amount of AF within the WM and increase the amount of the GBF.

Figure 4.7 shows optical micrographs of CGHAZ of SAW A709 Grade 50 steel joints produced using different heat inputs. As can be seen from the figure, high heat input resulted in coarser microstructures. The observations made in this study about how the microstructures of the WM and CGHAZ changed with heat input are consistent with many other previous works (Harrison and Farrar, 1987; Dallam *et al*., 1985; Kim *et al*., 2005; Prasad and Dwivedi, 2008).

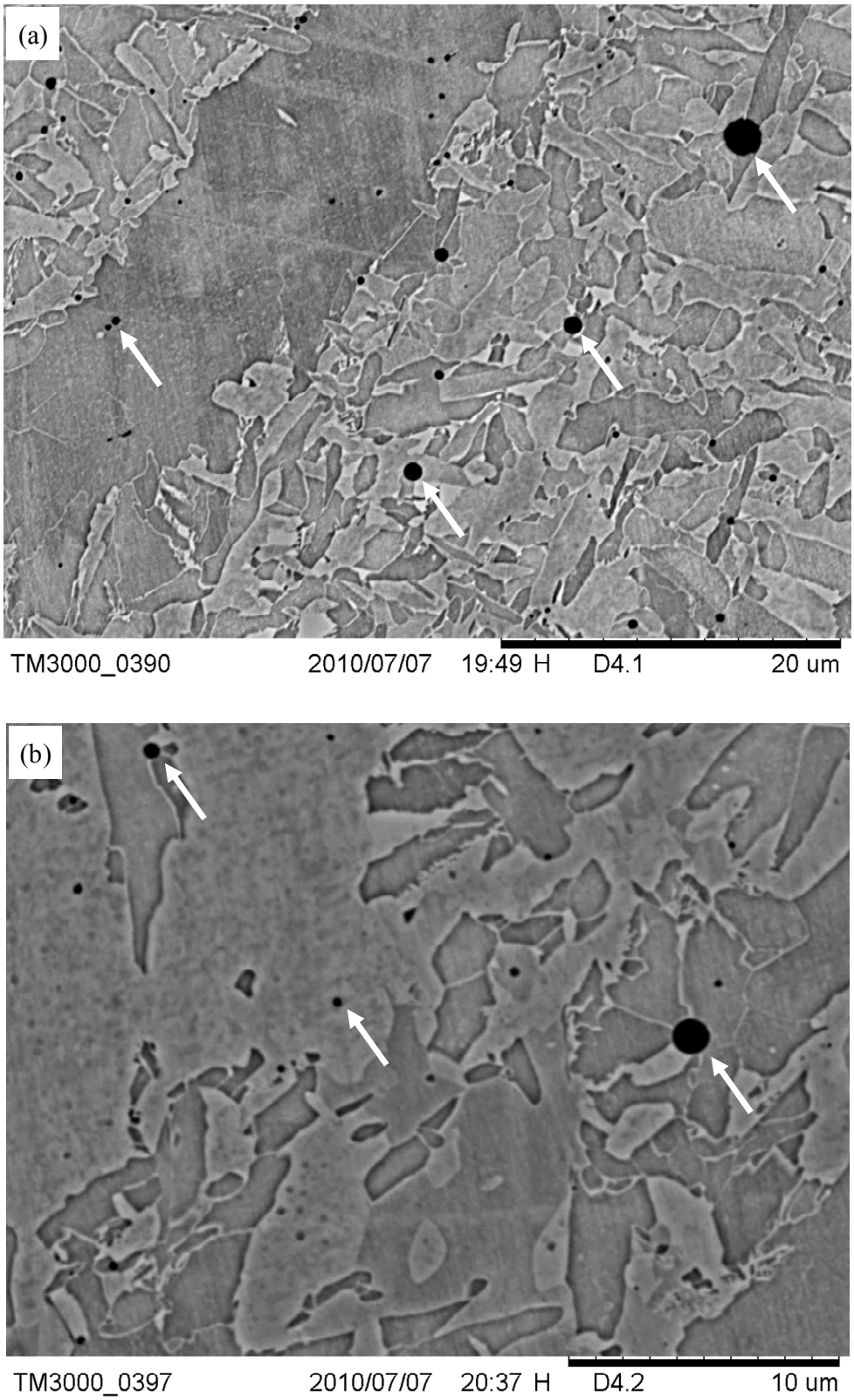

Figure 4.3. Secondary electron SEM micrographs from an as-polished welded joint: (a) the WM and (b) the HAZ.

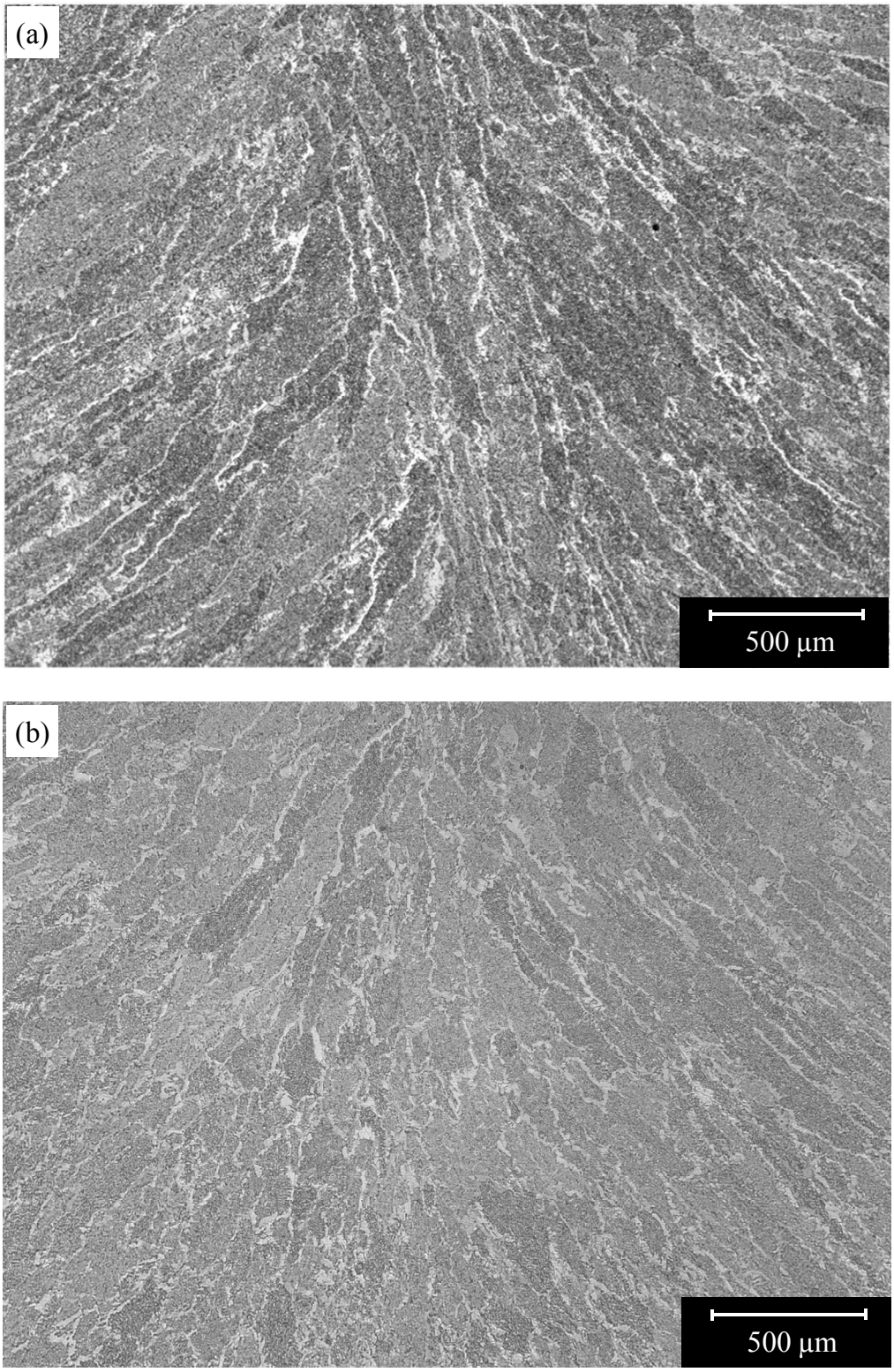

Figure 4.4. Optical micrographs of the WMs of welded ASTM A709 Grade 50 steel joints produced using (a) 3.03 kJ/mm, (b) 3.43 kJ/mm, (c) 4.11 kJ/mm, and (d) 4.56 kJ/mm heat input.

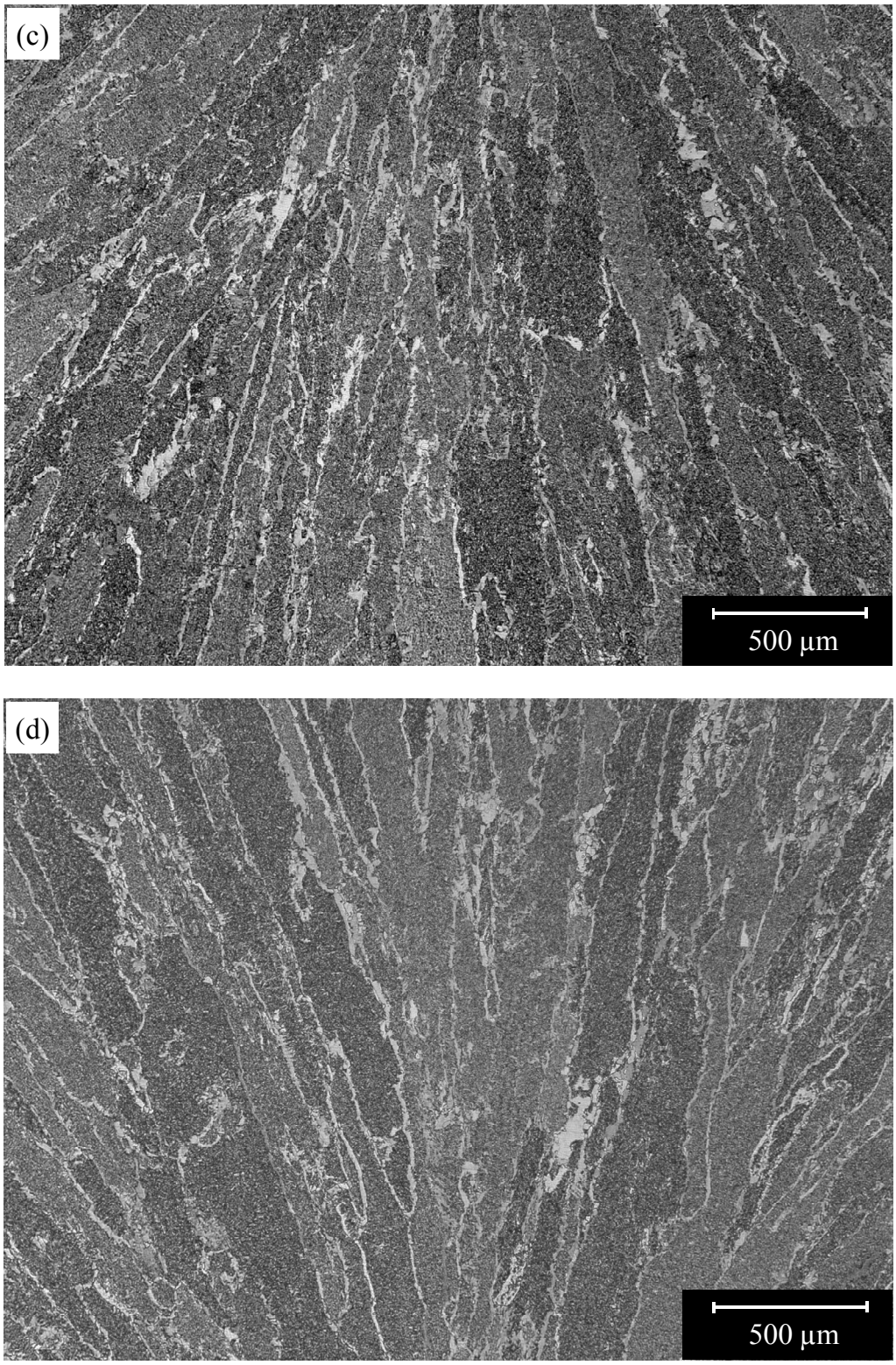

Figure 4.4 continued.

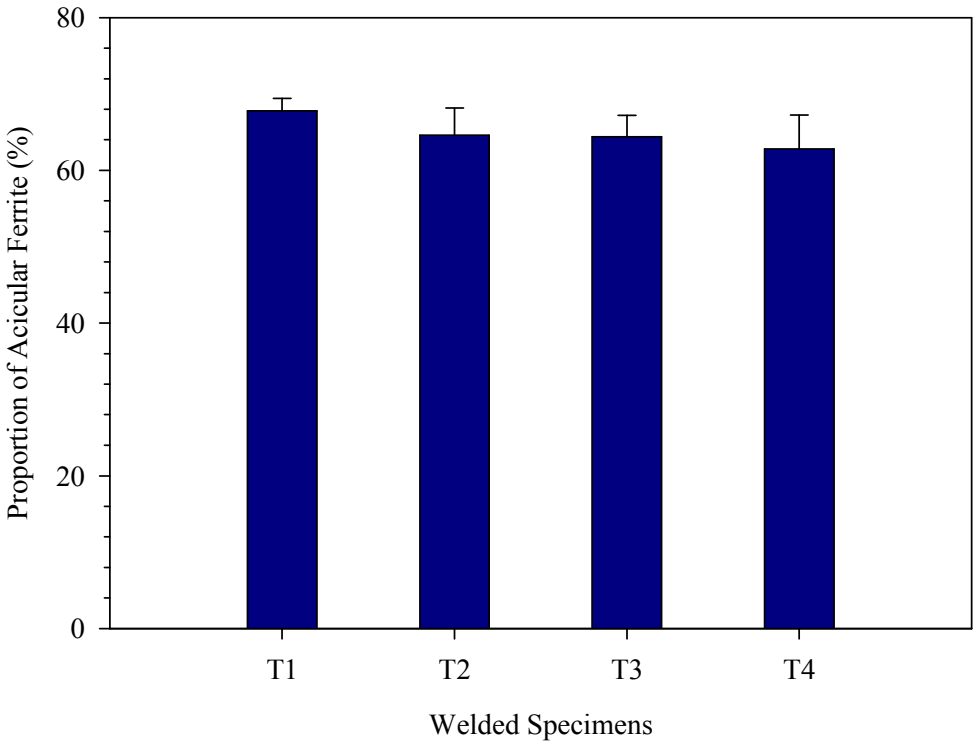

Figure 4.5. Proportion of acicular ferrite within the WM of welded A709 steel specimens. (T1: 3.03 kJ/mm, T2: 3.43 kJ/mm, T3: 4.11 kJ/mm, and T4 4.56 kJ/mm).

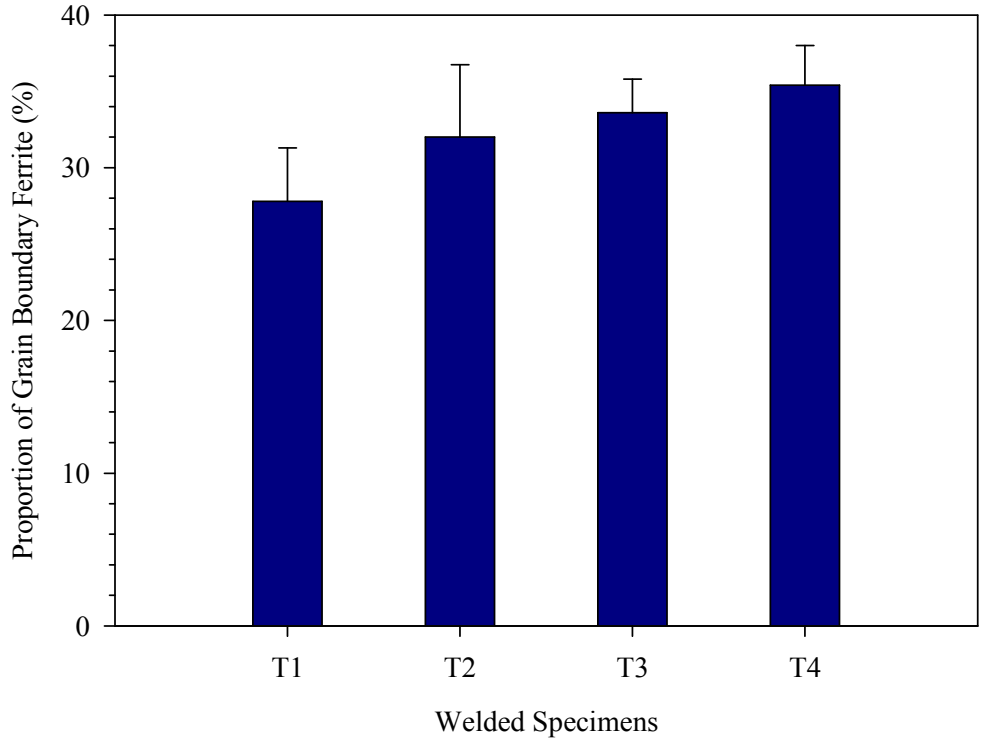

Figure 4.6. Proportion of grain boundary ferrite within the WM of welded A709 steel specimens. (T1: 3.03 kJ/mm, T2: 3.43 kJ/mm, T3: 4.11 kJ/mm, and T4 4.56 kJ/mm).

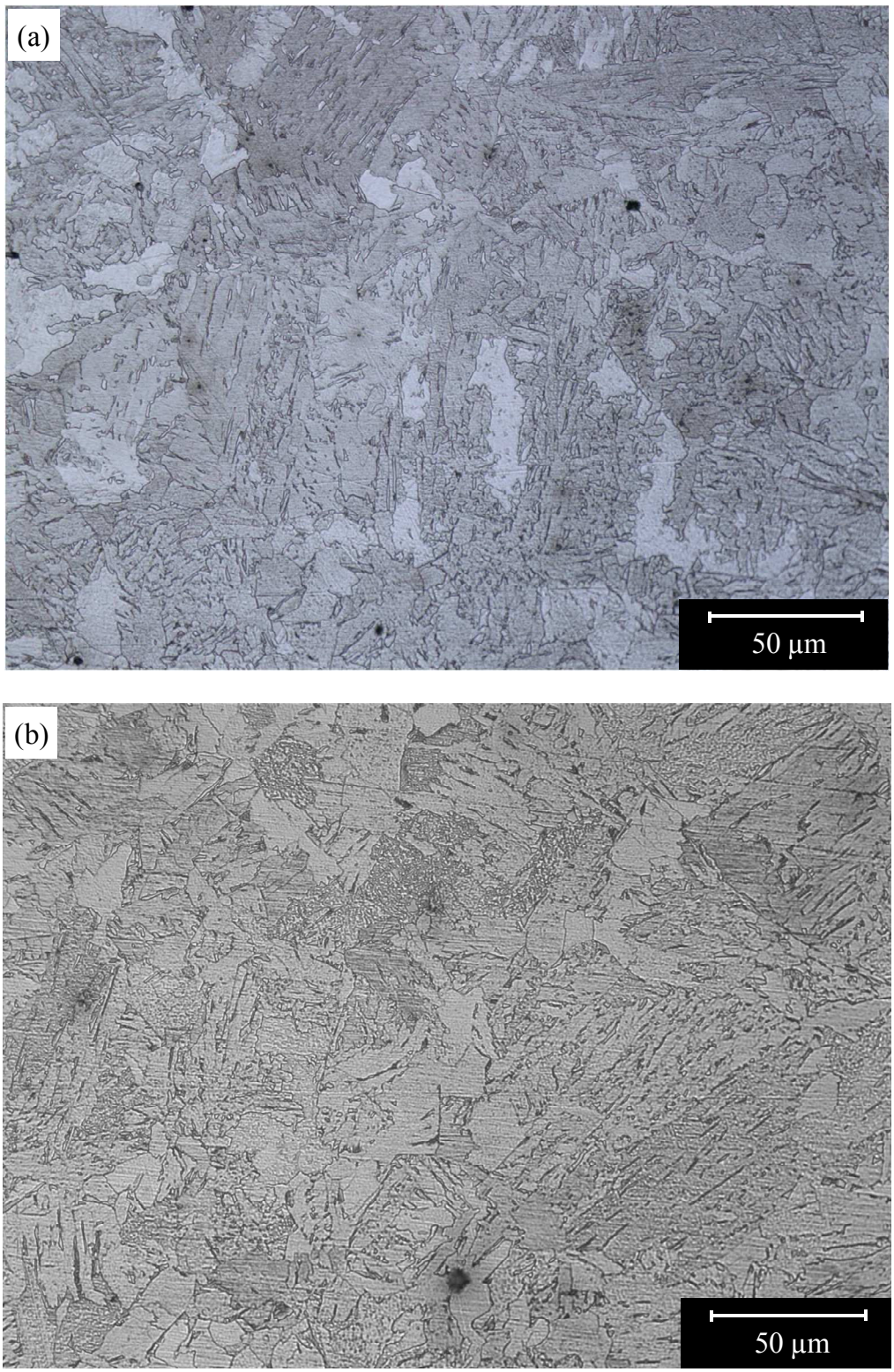

Figure 4.7. Optical micrographs of the CGHAZs of welded ASTM A709 Grade 50 steel joints produced using (a) 3.03 kJ/mm, (b) 3.43 kJ/mm, (c) 4.11 kJ/mm, and (d) 4.56 kJ/mm heat input.

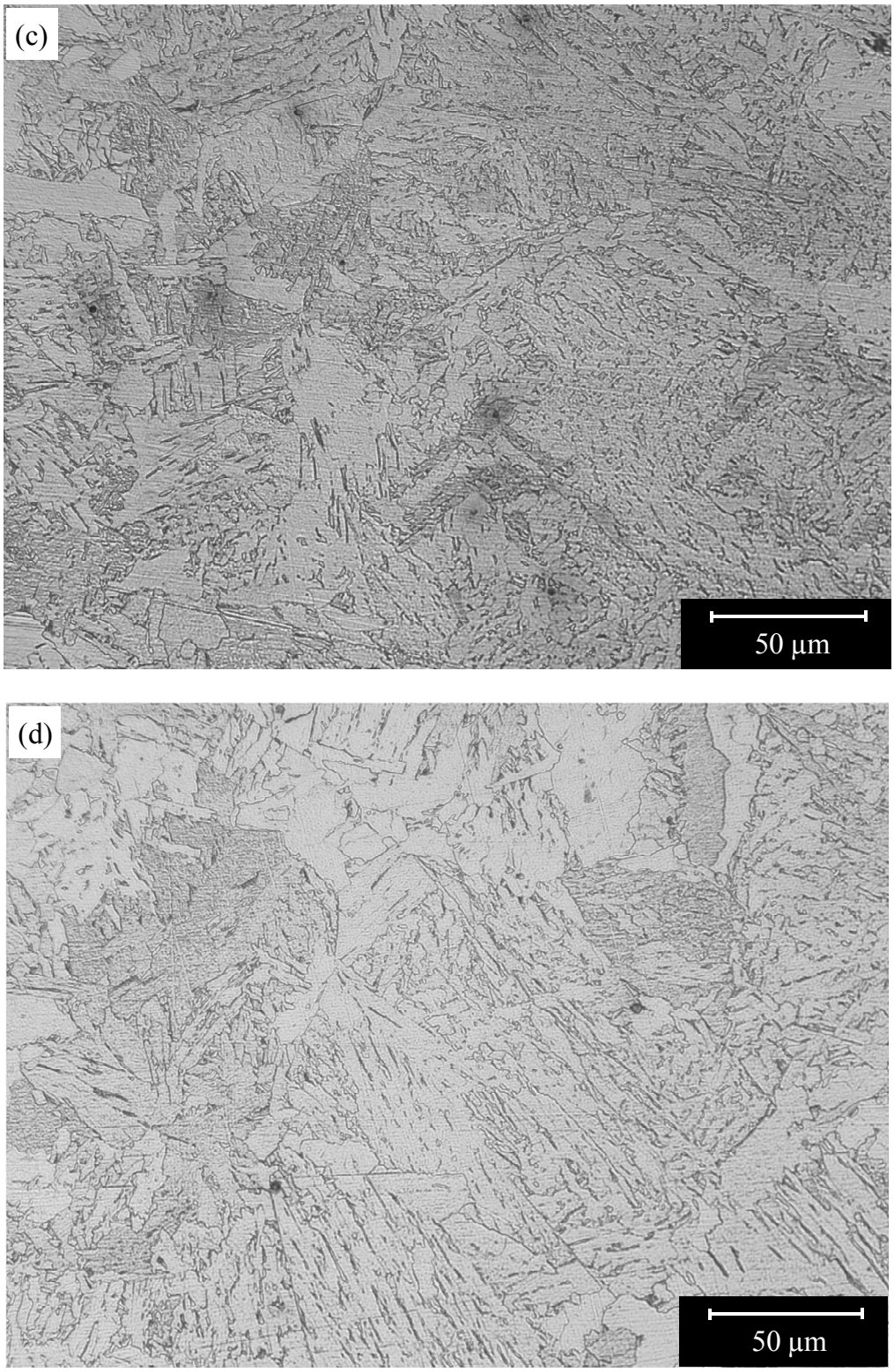

Figure 4.7 continued.

4.2 Effect of Heat Input on Weld Bead Geometry of ASTM A709 Grade 50 Steel Weld

4.2.1 Weld Bead Geometry

Figure 4.8 shows the effect of heat input on the penetration depth (P), HAZ size (H), bead width (W), bead reinforcement (R), contact angle (θ), penetration area (A_p'), deposition area (A_d'), and total molten area (A_t) obtained for the second pass of weldments. θ is the average of θ_1 and θ_2. Solid lines in the graphs are the fitted curves (trend lines), while dotted curves represent the variation tendency. Error bars are the standard deviation of the measurements. It can be seen that with the increase in heat input, P, H, W, R, A_p', A_d', and A_t (Figures 4.8(a)-(g)) increased, while θ (Figure 4.8 (h)) decreased.

In a typical arc welding process, both plate and electrode melting are expected to increase with increasing heat input. Plate melting is related to the P, H and A_p', while weld bead shape and A_d' are related to electrode melting (Gunaraj and Murugan, 1999). High heat input would produce a large molten metal pool in the fusion zone and hence large A_p' as shown in Figure 4.8 (e). As cooling rate varies inversely with heat input, the molten metal would remain liquid metal for a long time at high heat input, causing deep penetration (P) and large heat transfer to parent metal. The latter of which would give rise to a large HAZ size (H). Therefore, as shown in Figure 4.8 (a), penetration increased with heat input for both single wire- and tandem wire-welded specimens. Compared to single wire welds the tandem wire-welded plates have higher heat input,

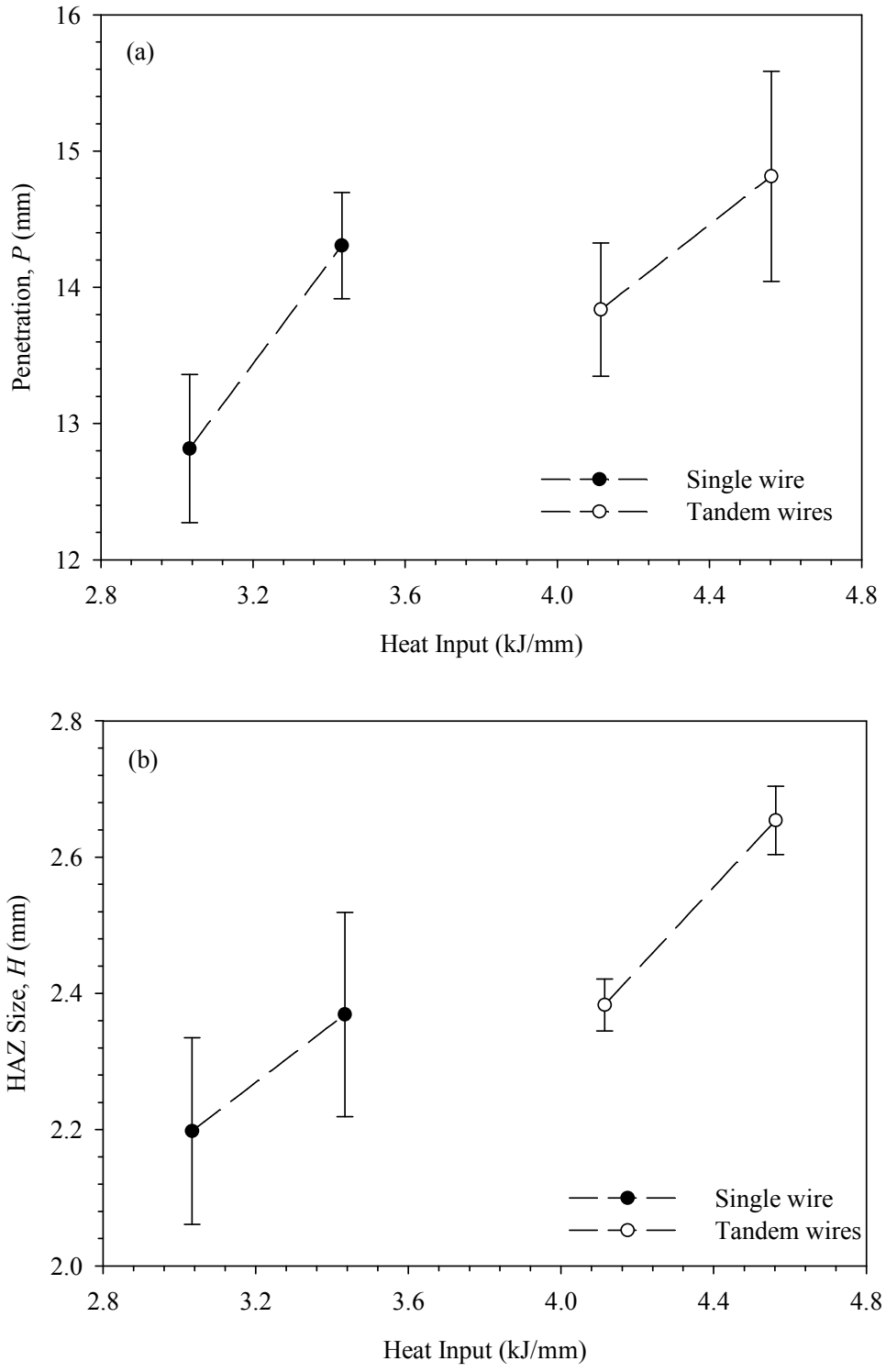

Figure 4.8. Effect of heat input on (a) penetration depth, (b) HAZ size, (c) bead width, (d) bead reinforcement, (e) penetration area, (f) deposition area, (g) total molten area, and (h) contact angle of A709 steel welded joints.

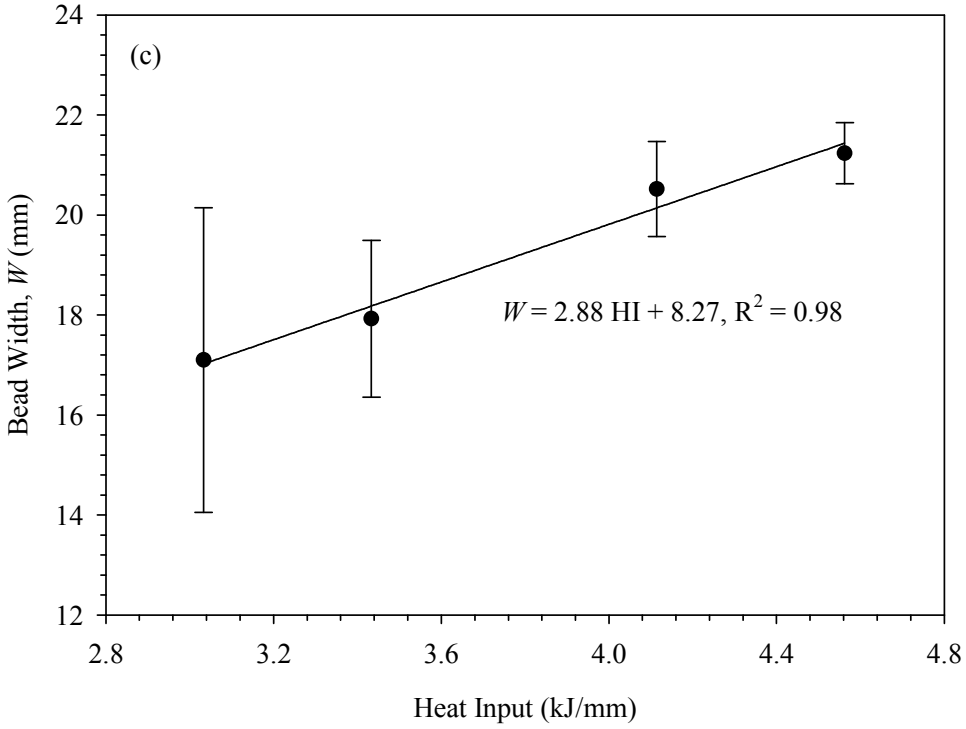

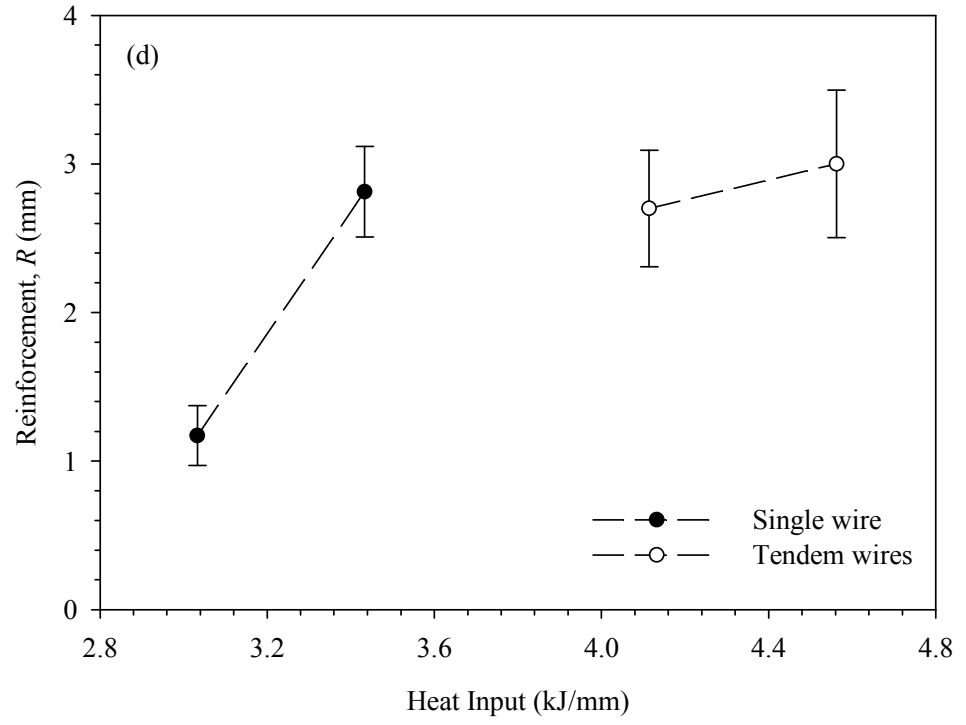

Figure 4.8 continued.

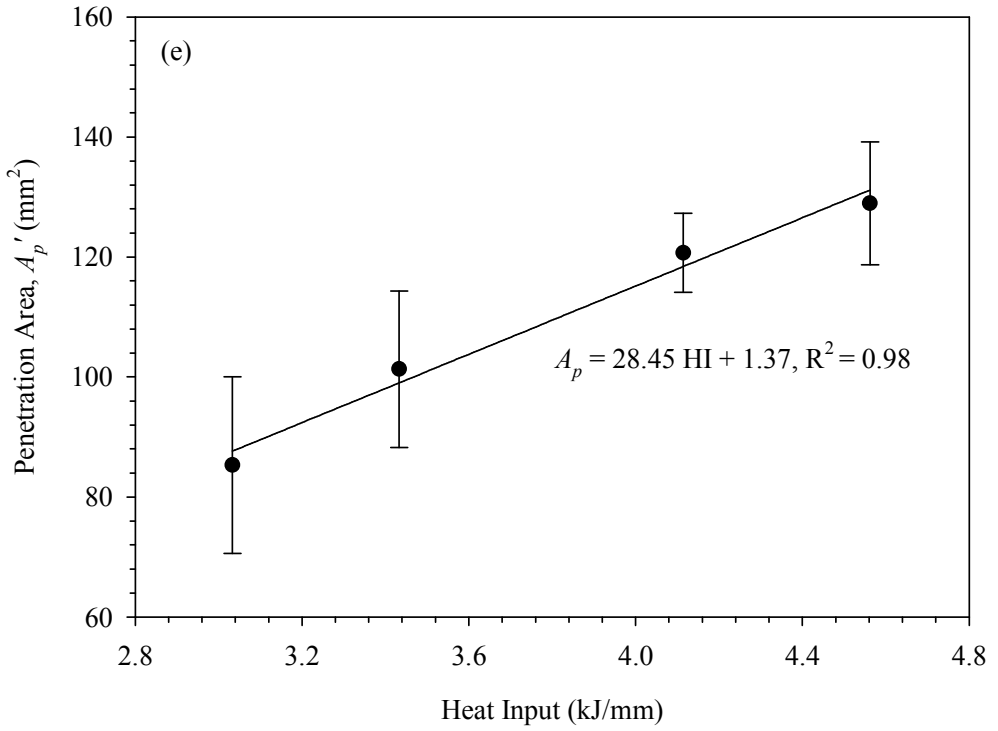

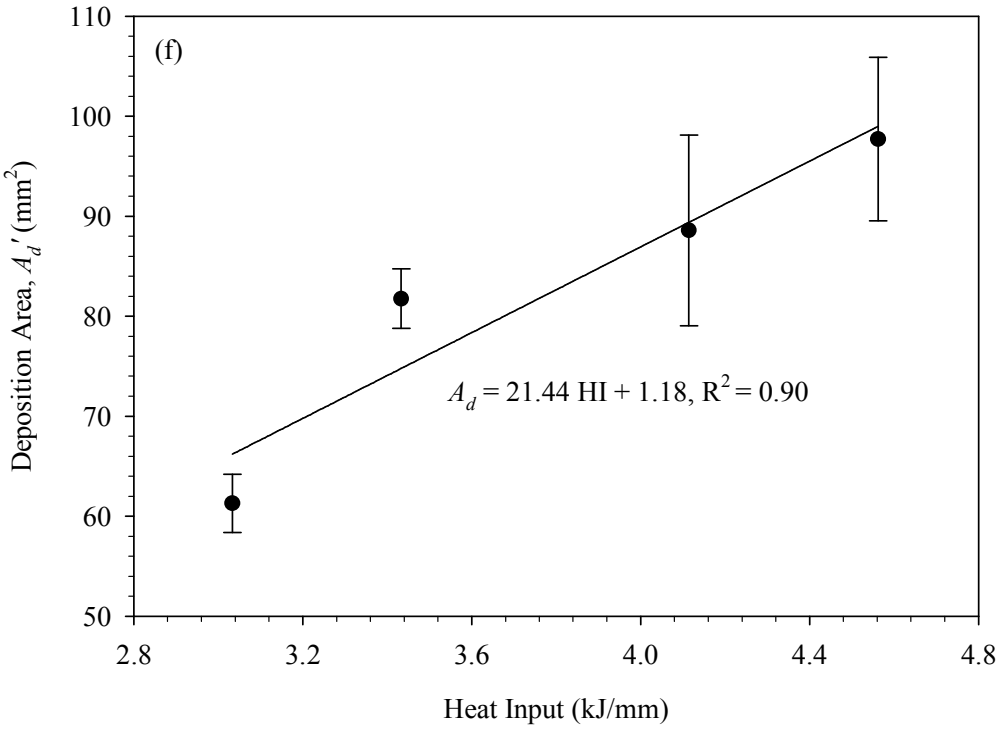

Figure 4.8 continued.

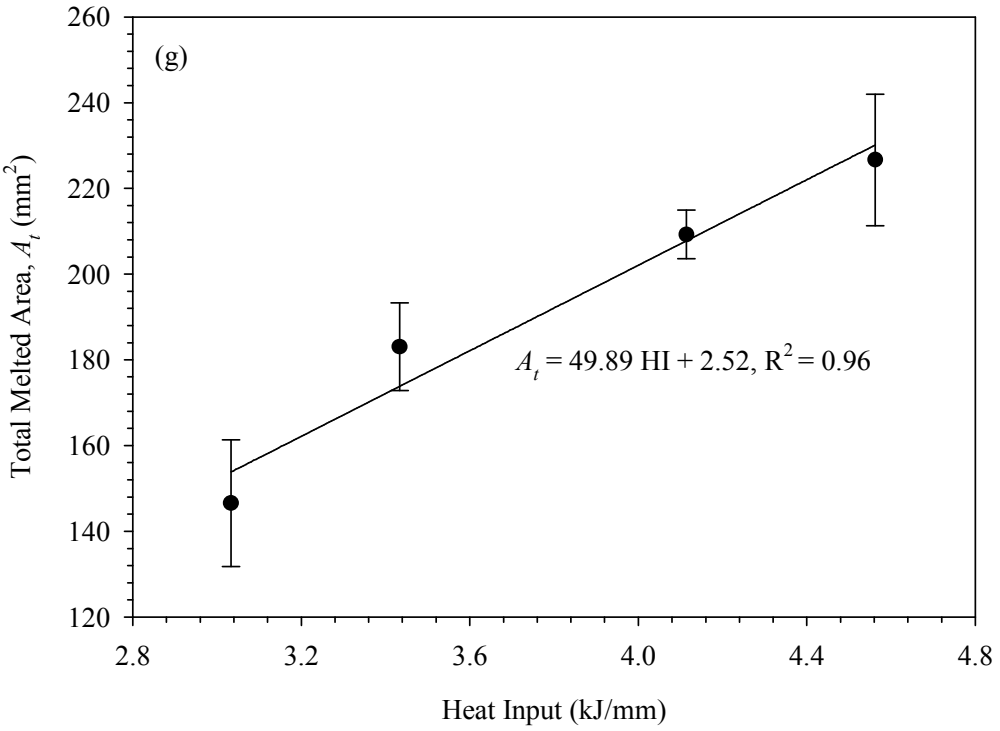

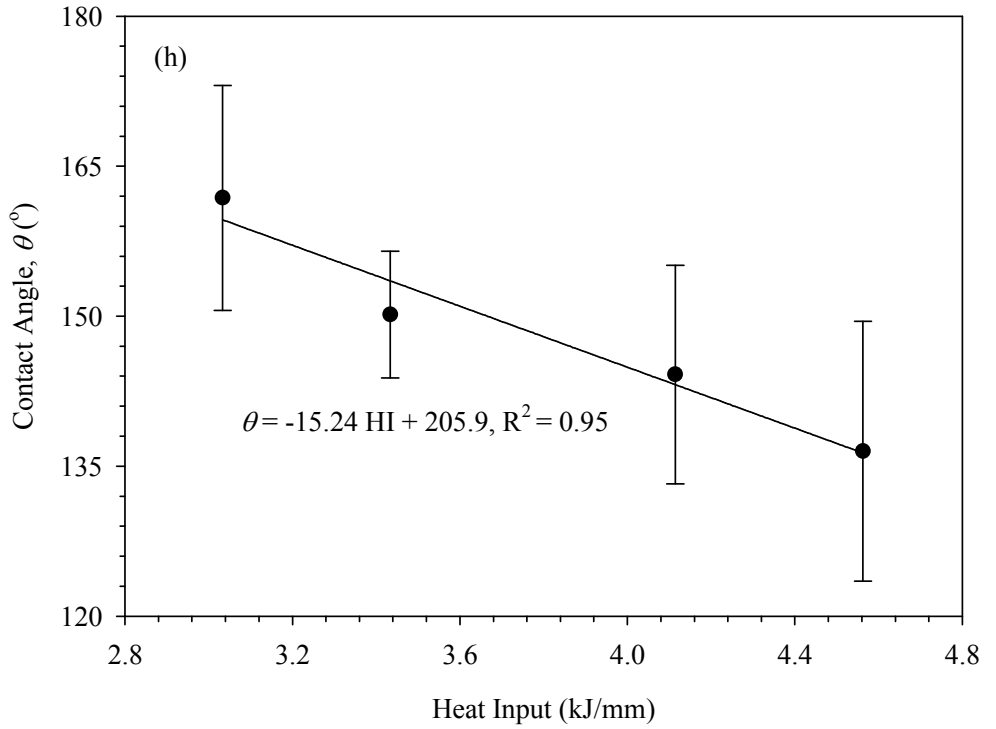

Figure 4.8 continued.

although, much higher welding speed was used during the welding process (See Table 3.4). According to the work of Yang (2008) who studied single-wire SAW, the effect of welding speed on penetration is greater than that of welding current. Therefore, it makes sense that the penetration depth of plates welded with a heat input of 4.11 kJ/mm was lower than that of plates welded with the heat input of 3.43 kJ/mm. However, with further increase heat input to 4.56 kJ/mm, the penetration of tandem wire-welded plates increased. The same trend was observed for the HAZ size as shown in Figure 4.8 (b).

Increased electrode melting resulting from increase of heat input would change the weld bead shape parameters such as W, R and θ. To explore how heat input affected them, we made a simple assumption that the shape of the top surface of deposition area (A_d') in Figure 3.6 is an isosceles triangle with R as its height. Then using trigonometric relations and area formula, we obtained a relationship between A_d, R, W, and θ. For a right-angled triangle,

$$A_d = \frac{1}{2} RW \Rightarrow R = \frac{2A_d}{W} \tag{4.1}$$

where $A_d = A_d$' - A_b, was the same for all the plates and represents the cross-sectional area of bevelled section. For an isosceles triangle with θ as its exterior angle, we have

$$\tan(180-\theta) = \frac{R}{(W/2)} \Rightarrow R = \frac{W \times \tan(180-\theta)}{2} \tag{4.2}$$

Since A_d increased with increasing heat input, it is clear from equation (4.1) that R would also increase with it. Figure 4.8 (d) shows that R increased with heat input, but θ decreased with it because the value of tan (180-θ) decreases with increasing θ. Therefore, as shown in Figure 4.8 (h), contact angle θ decreased with increasing heat input.

4.2.2 Percent Dilution and Melting Efficiencies

The fusion area is controlled by the bead width-to-depth ratio, $W/(R+P)$ (Chakravarti *et al*., 1985). This ratio is an important parameter for assessing the quality of a welded joint. It relates to the percentage dilution. Figure 4.9 shows the effect of heat input on the bead width-to-depth ratio. As can be seen, it varied very little with increasing heat input.

Percent dilution was calculated using equation (4.3) (Lancaster, 1999):

$$\%\,\text{Dilution} = \frac{\text{weight of parent metal melted}}{\text{total weight of fused metal}} \times 100 = \frac{A_p'}{A_t} \times 100 \qquad (4.3)$$

where A_p' and A_t keep the original meanings. Figure 4.10 shows the effect of heat input on percent dilution for the steel welds. The average percent dilution obtained in this study was 57%, which is in a reasonable agreement with the value reported in (Clark, 1985). As can be seen from the figure, it is reasonable to conclude that percent dilution remained practically unchanged as heat input increased. This behavior is similar to the

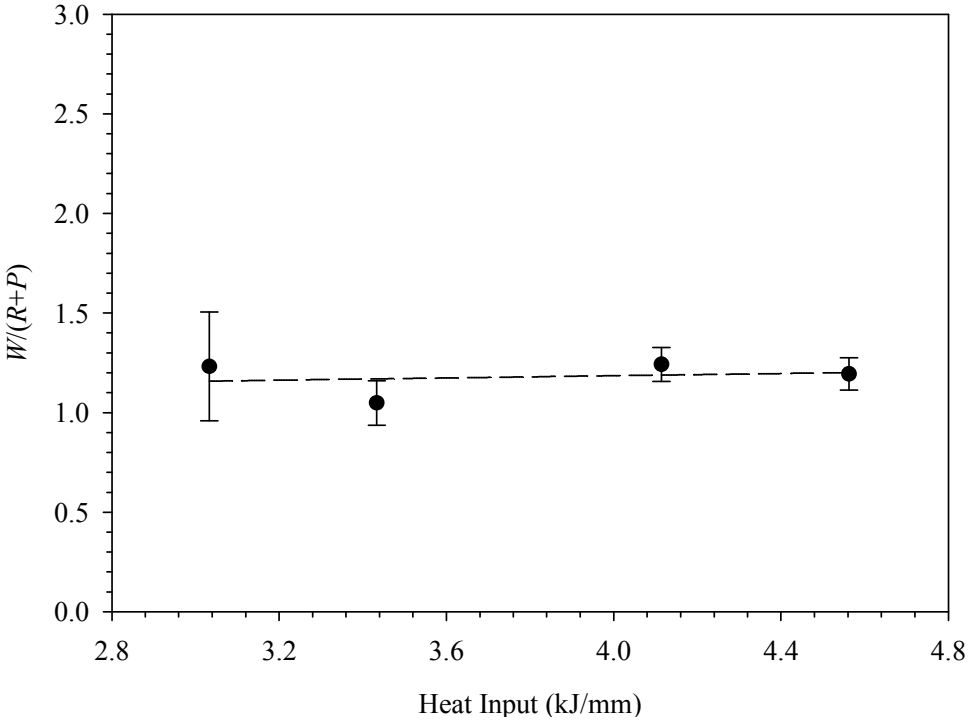

Figure 4.9. Effect of heat input on the ratio of bead width to depth.

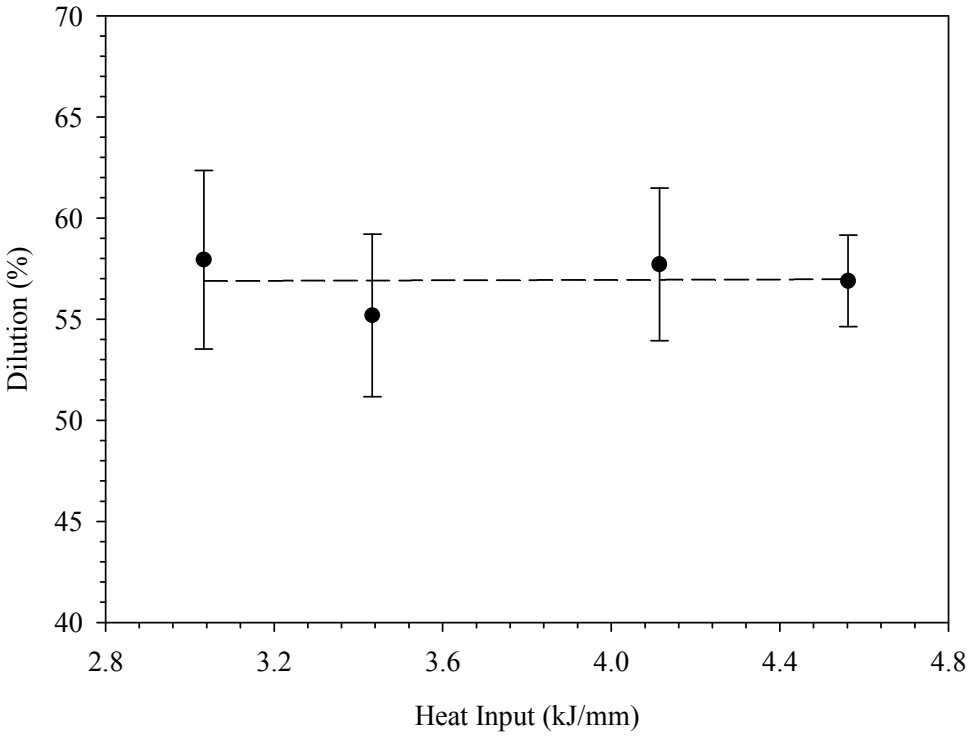

Figure 4.10. Effect of heat input on percent dilution of A709 steel welded joints.

relationship between bead width-to-depth ratio and heat input. The practical implication of this is that it could be possible to predict the relationship between percent dilution and heat input from the bead width-to-depth ratio versus heat input plot.

The effect of heat input on plate melting, electrode melting, and total melting efficiencies (E_{pm}, E_{em}, and E_{tm}, respectively) is shown in Figure 4.11. In this work, these melting efficiencies were calculated using the equations developed in (Chandel, 1990).

$$E_{em}(\%) = \frac{100 A_d^{'}}{0.0854 \times 1000 \mathrm{HI}} \tag{4.4}$$

$$E_{pm}(\%) = \frac{100 A_p^{'}}{0.0854 \times 1000 \mathrm{HI}} \tag{4.5}$$

$$E_{tm}(\%) = \frac{100 A_t}{0.0854 \times 1000 \mathrm{HI}} \tag{4.6}$$

where A_d', A_p', A_t and HI retain their original meanings.

The results show that E_{em} increased from 23% to 28% for the single wire welding while it remained practically at approximately 25% for the tandem wire welding. For the SAW process, electrode melting is mainly affected by welding current, welding speed, electrode diameter, electrode polarity, and electrode extension. For bead-on-plate welding, it was reported that E_{em} increased with increasing welding current when other

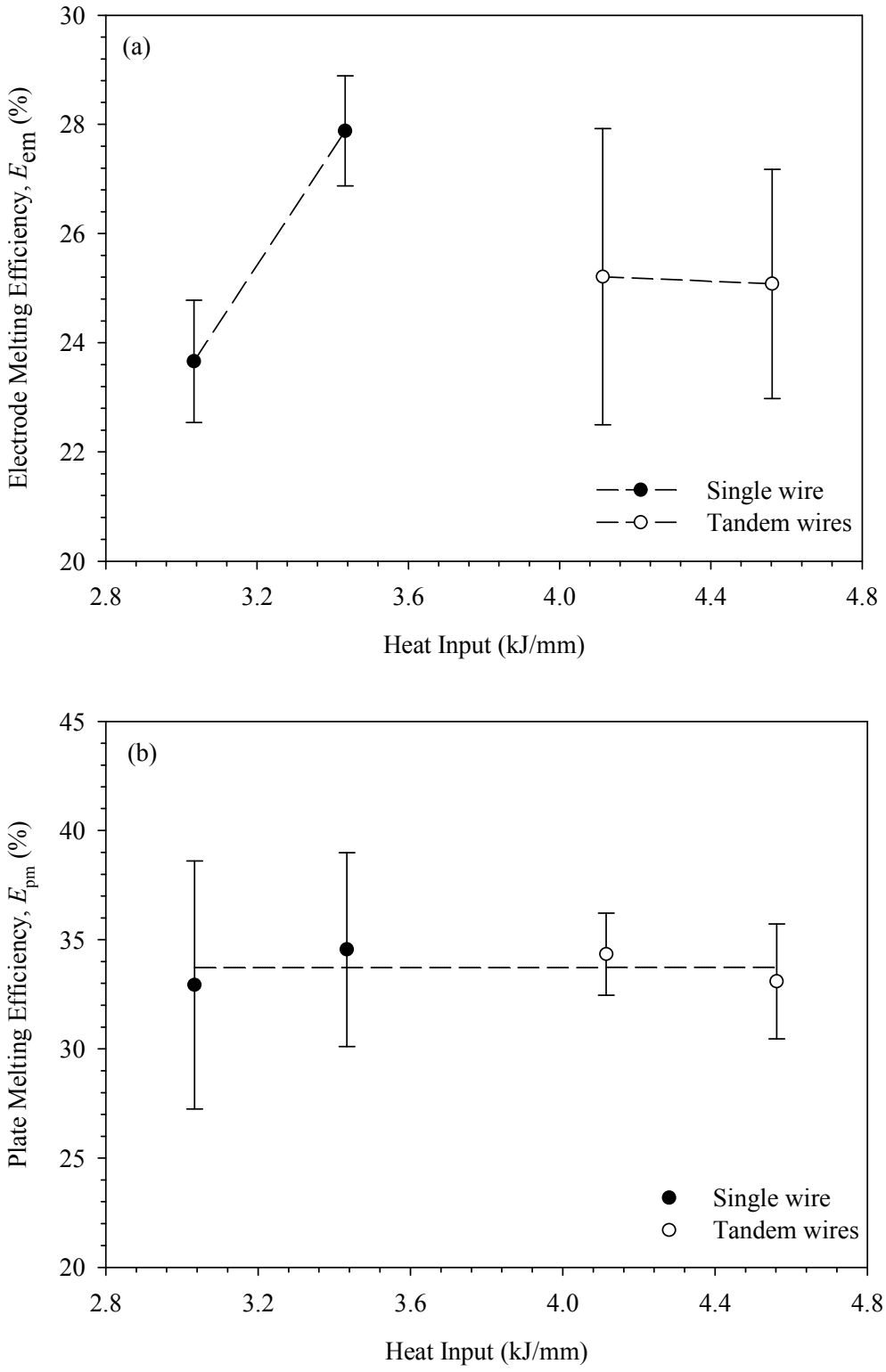

Figure 4.11. Effect of heat input on (a) plate melting efficiency and (b) electrode melting efficiency of A709 steel welded joints.

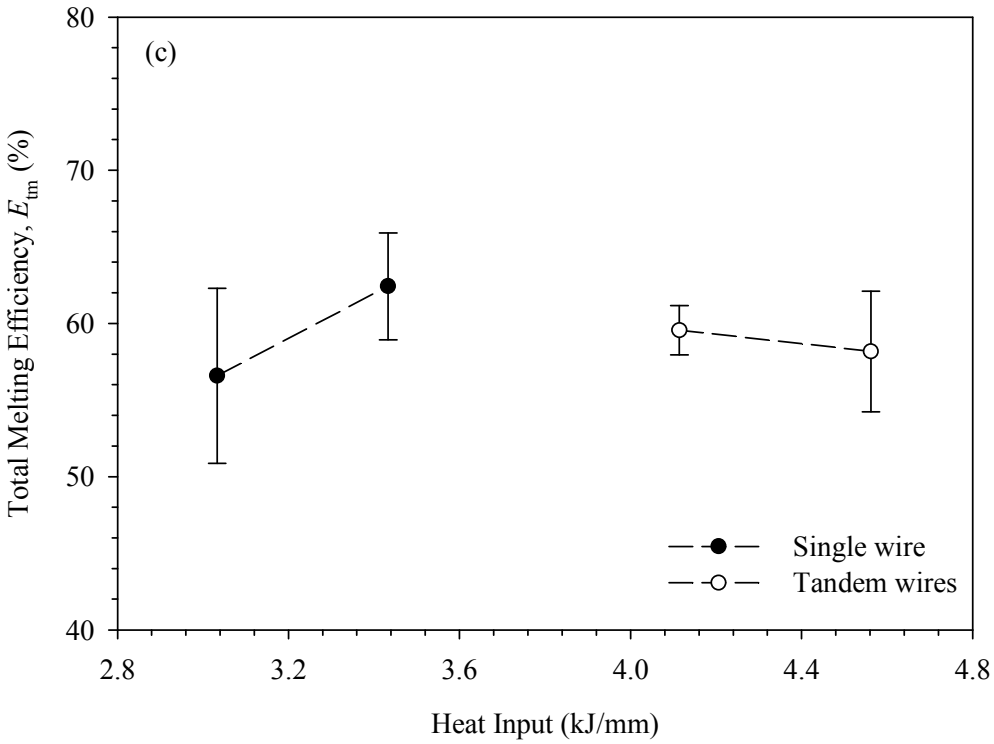

Figure 4.11 continued.

parameters remain unchanged (Lee *et al*. 2000, Chandel, 1990). The E_{em} of T2 was greater than that of T1 because its welding current was higher than that of T1. According to this line of argument, the E_{em} of T3 and T4 should be higher than that of T1 and T2 because the welding currents and heat inputs used for them were higher than those of T1 and T2. However, the results showed that E_{em} of T3 and T4 was lower than that of T2 but higher than that of T1. The plausible reason is that the higher welding speed used for T3 and T4 led to lower E_{em} in this study. The welding speed of T3 and T4 were much higher than those of T1 and T2. Thus the combined effects of high heat input and the high welding speed could be either increased or reduced E_{em}.

E_{pm}, with values that ranged from 33% to 34.5%, did not change appreciably with heat input for both single wire and tandem wire welding. It was reported in (Lee *et al*. 2000) that E_{pm} increased with welding current, but decreased with welding speed. As shown in Table 3, the welding current and welding speed of T4 were higher than those of T1. The net effect of the increase in both welding current and welding speed was that E_{pm} did not change appreciably with heat input.

E_{tm} varied from 56% to 63% for the single-wire welding, but changed only slightly for the tandem wire welding. Although, E_{tm} is the sum of E_{em} and E_{pm}, it appears from this study that E_{pm} had a greater influence on it than E_{em}.

4.3 Effect of Heat Input on the Transverse Hardness of ASTM A709 Grade 50 Steel Weld

Figure 4.12 (a)-(d) shows the variation of hardness with distance from the weld center for welded ASTM A709 Grade 50 steel specimens produced using different heat inputs. It can be seen that the hardness of the welded joints decreased from the CGHAZ to the PM. In the CGHAZ, the hardness dropped from the area near the weld interface to the FGHAZ. On the contrary, the hardness of the WM did not change much. By calculating the average hardness values in each zone, it was found that the WM had the highest hardness, followed by CGHAZ, FGHAZ, and the PM. Yang (2008) also reported the same trend in the variation of hardness with distance from the weld center for ASTM A709 Grade 50 steel and ASME SA516 Grade 70 steel.

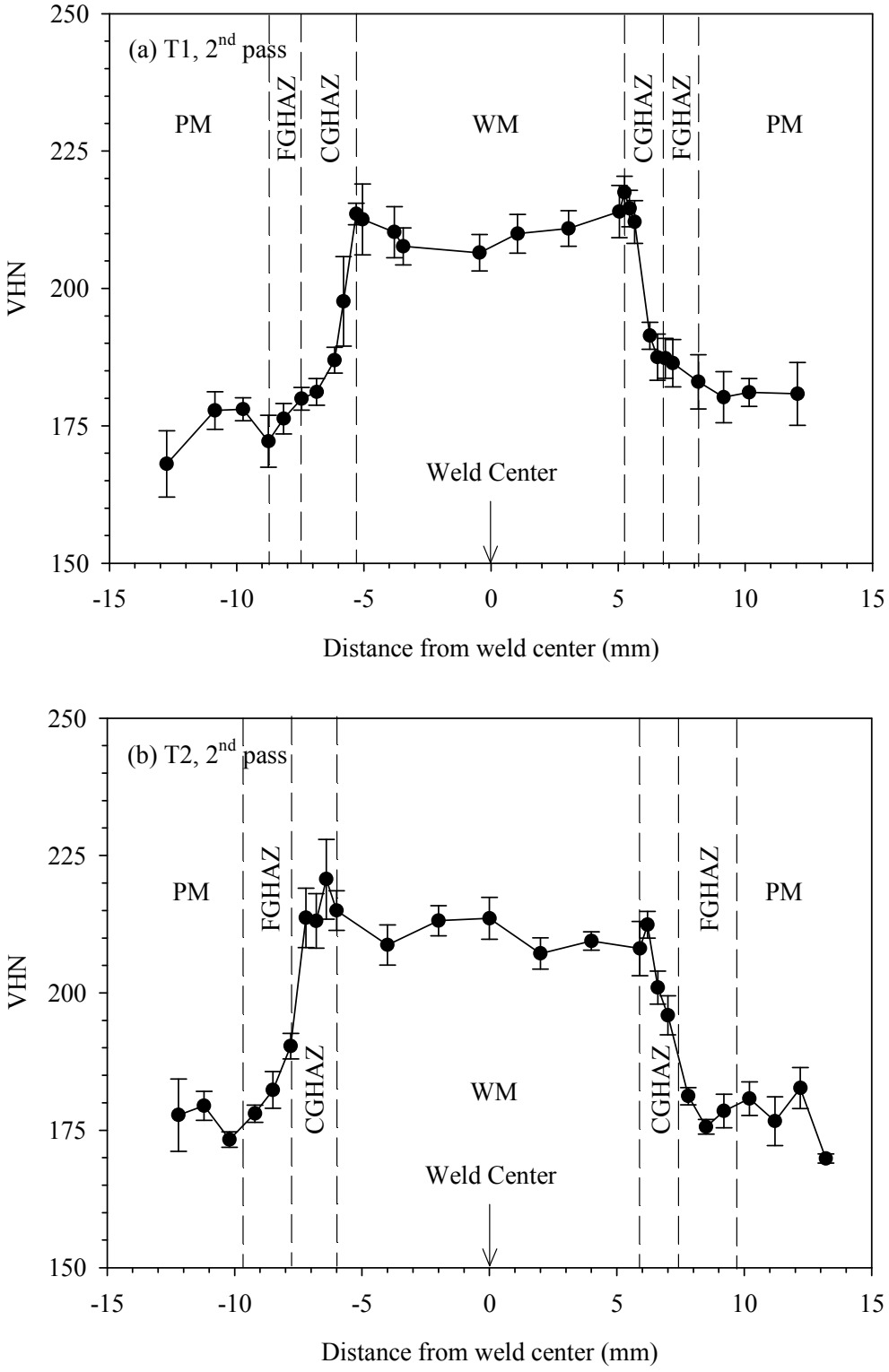

Figure 4.12. Variation of microhardness with distance from the weld center for the specimens produced using (a) 3.03 kJ/mm, (b) 3.43 kJ/mm, (c) 4.11 kJ/mm, and (d) 4.56 kJ/mm heat input.

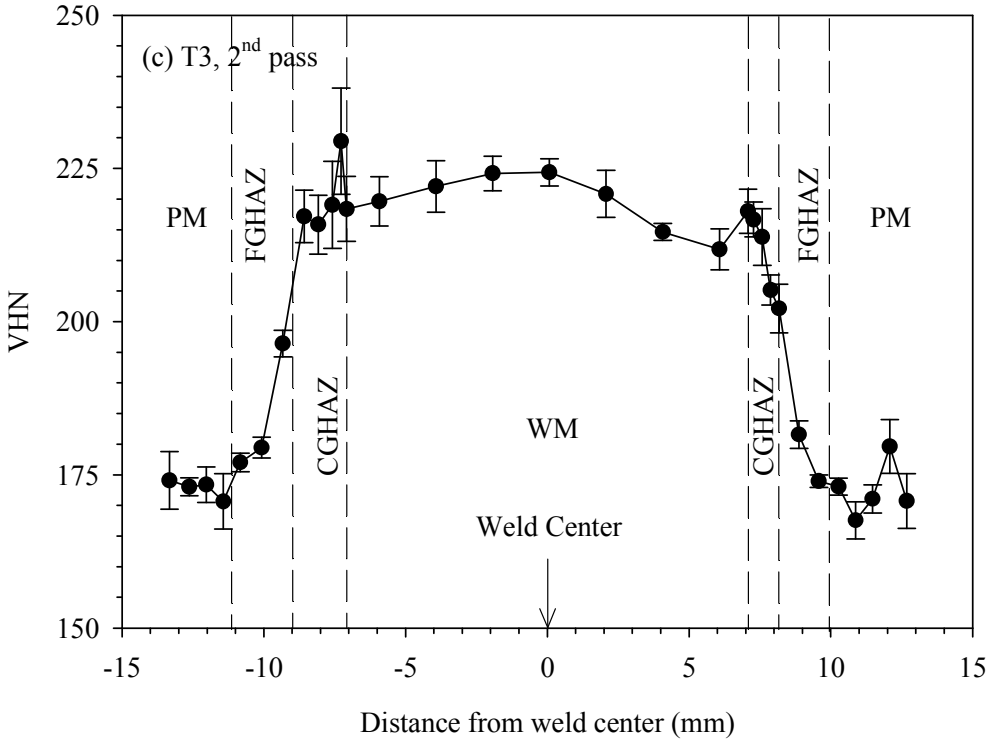

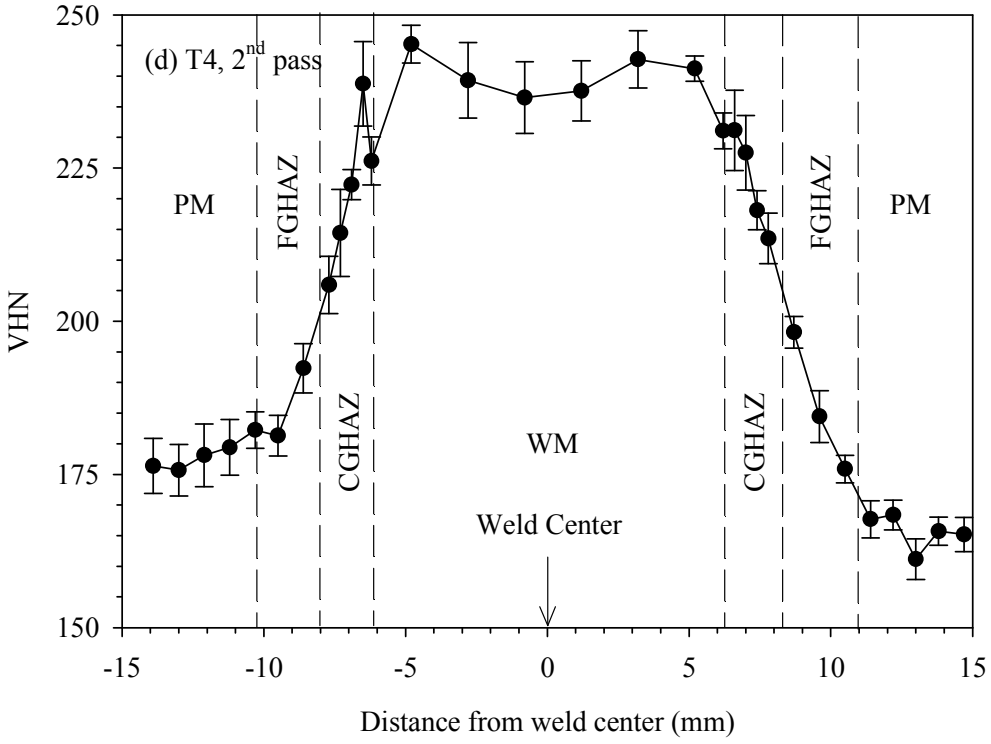

Figure 4.12 continued.

The trend of hardness variation with the distance from the weld center can be explained by looking at the microstructures of each zone (see Figure 4.2). The WM has the highest hardness due to the presence of a large quantity of acicular ferrite. As a result of high cooling rate in the CGHAZ near the weld interface, bainite or pearlite could form in this zone. So, the hardness of the CGHAZ near the weld interface was very close or even higher than that of the WM. Compared to the PM, the microconstituents within FGHAZ are the same as those in the PM, except that the grain size of these microconstituents in the FGHAZ is smaller than those of the PM. Thus, the hardness of the FGHAZ is generally greater than that of the PM but lower than that of the CGHAZ.

Figure 4.13 presents the variation of the average hardness of the WM, CGHAZ, FGHAZ and PM with heat input. With an increase in heat input from 3.03 to 4.56 kJ/mm, the mean hardness increased by ~14% in the WM, but did not change appreciably in the CGHAZ, FGHAZ and PM.

It was reported that an increase in heat input reduced the hardness of WM because of the increase in volume fraction of ferrite (Viano *et al*., 2000) or coarsening of ferrite (Yurioka *et al*., 1987; Neves and Loureiro, 2004). However, in the present study, the measured WM hardness increased even when there was coarsening of ferrite and a slight increase in the volume fraction of grain boundary ferrite in the WM. The reason is unknown and necessitates further investigations. Previous research showed that high heat input led to a decrease in hardness of the CGHAZ because the low cooling rate associated with it reduced the amount of martensite formed (Moeinifar *et al*., 2011).

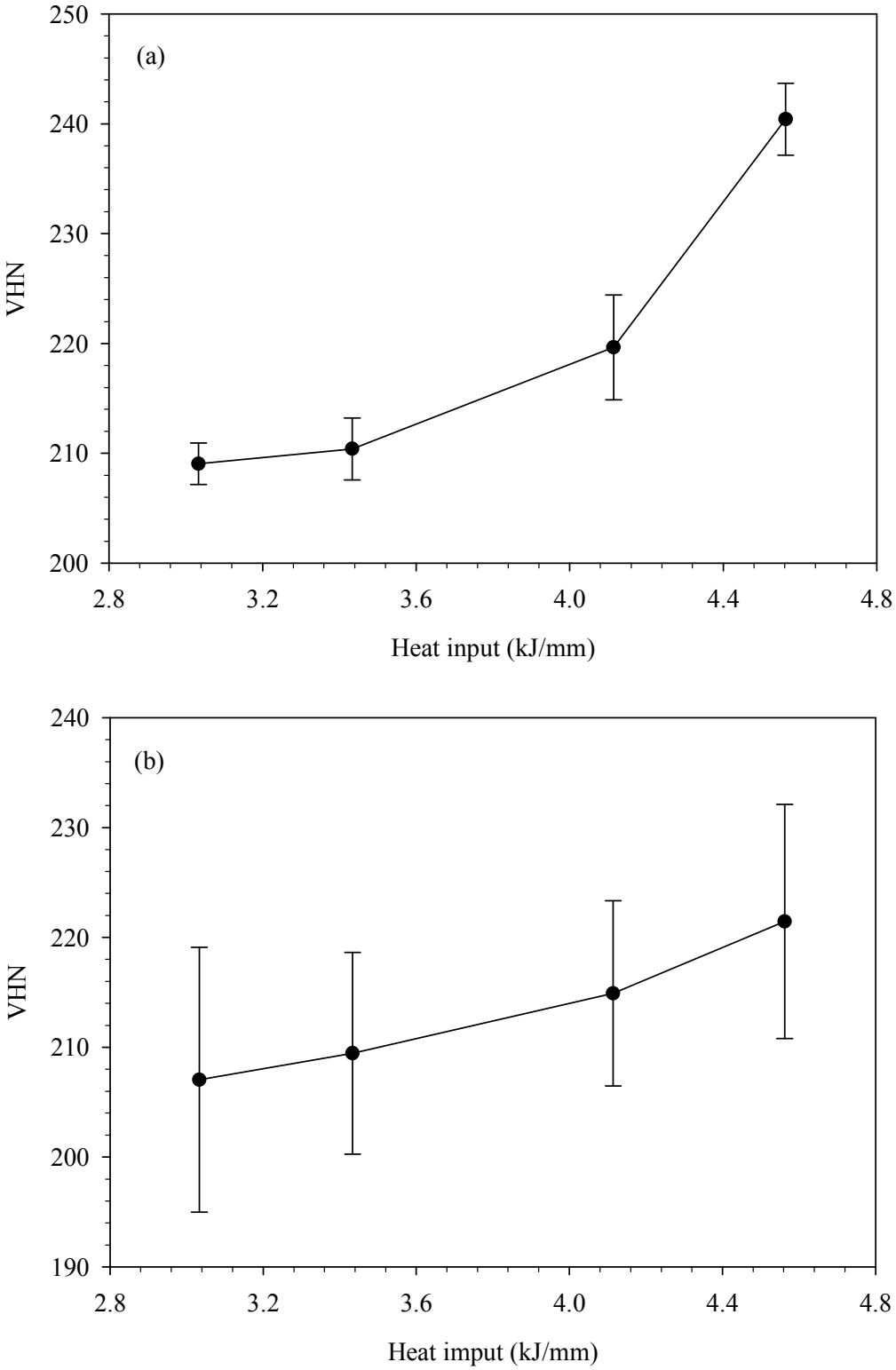

Figure 4.13. Variation of average hardness with heat input: (a) WM, (b) CGHAZ, (c) FGHAZ and (d) PM.

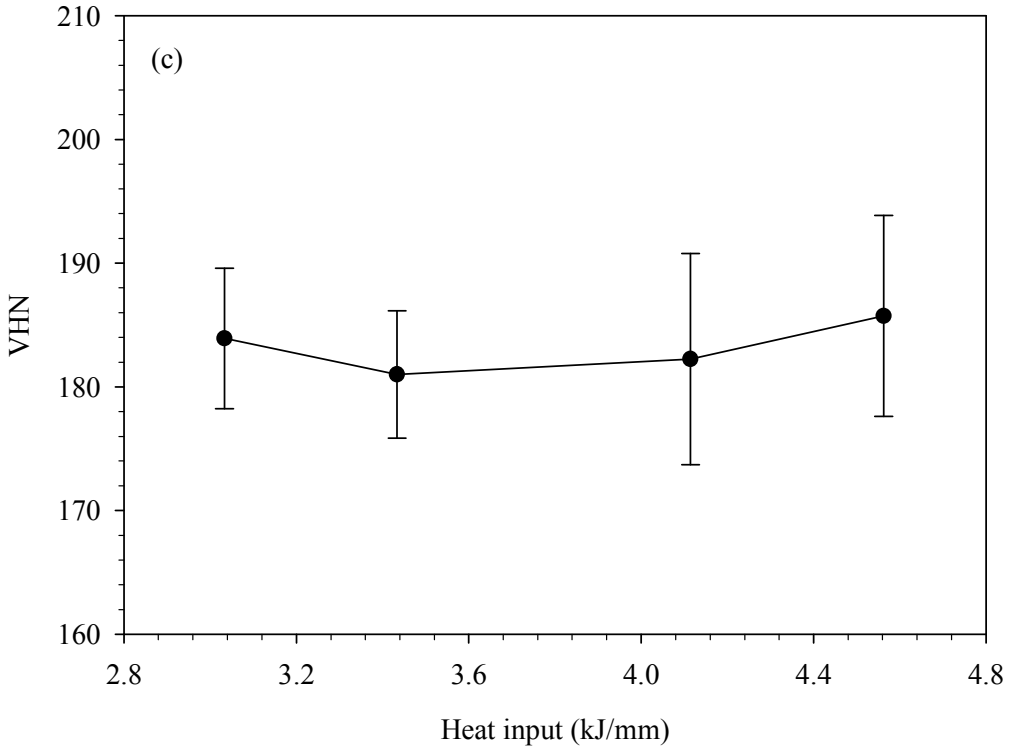

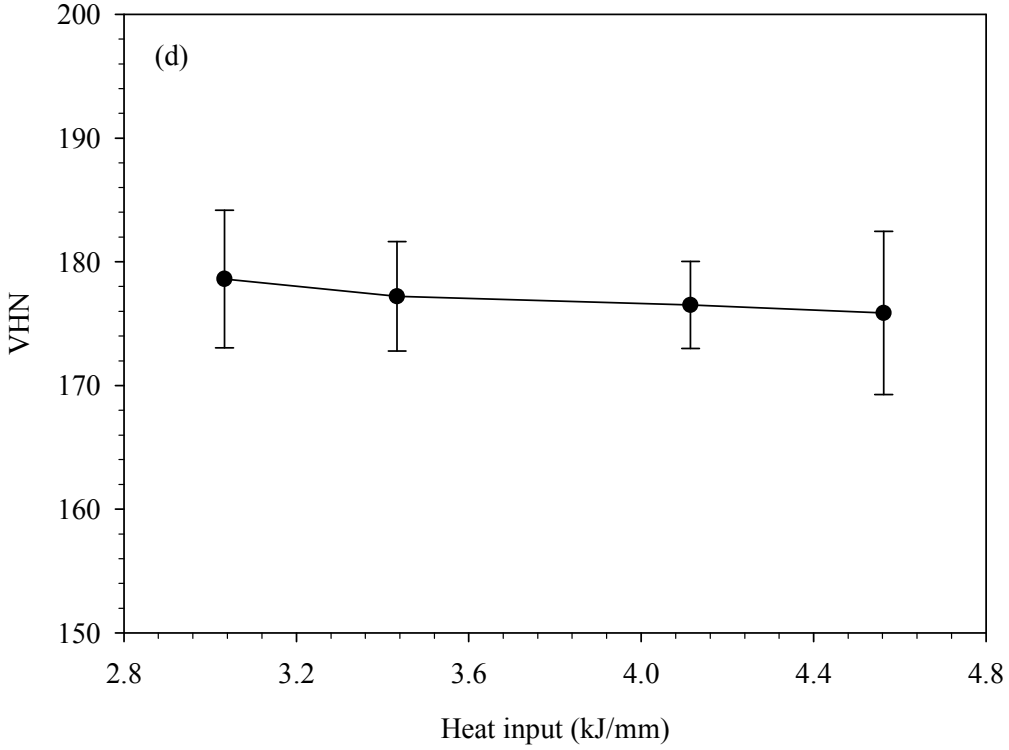

Figure 4.13 continued.

However, in the present study, the carbon contents of the parent metal and the electrode were 0.07 wt.% and 0.1 wt.%, respectively, and so no martensite formed (Figure 4.7). Therefore, the hardness of the CGHAZ did not change much with increase in heat input (the error bars overlapped). The reason why heat input had little effect on the hardness of the PM and FGHAZ could be because under different heat input conditions the cooling rate of the FGHAZ remained virtually unchanged due to its relatively long distance from the WM, and in the PM there was no metallurgical change during the welding process.

4.4 Effect of Heat Input on Tensile Properties of ASTM A709 Grade 50 Steel Weld

Typical stress-strain plots obtained for unnotched and notched tensile test specimens of the PM of the ASTM A709 Grade 50 steel are shown in Figure 4.14. The mechanical properties extracted from the plots are summarized in Table 4.1. The average tensile strength of the unnotched specimens of ASTM A709 Grade 50 steel was 496.7 MPa in the longitudinal direction, and 502.7 MPa in the transverse direction. Therefore, there is no appreciable difference in strength between the two directions. Typical values of the fatigue limit for steels are around 50%-60% of the tensile strength. Based on the average tensile strength obtained from the tensile tests, the applied minimum reversed stress in the fatigue test would be between 250 MPa and 300 MPa.

For the notched specimens, the average percent elongation was 16.1% and the average area reduction was 38.9%. The yield and ultimate strengths of the notched specimens were higher than those of unnotched specimens. This was because the cross-sectional

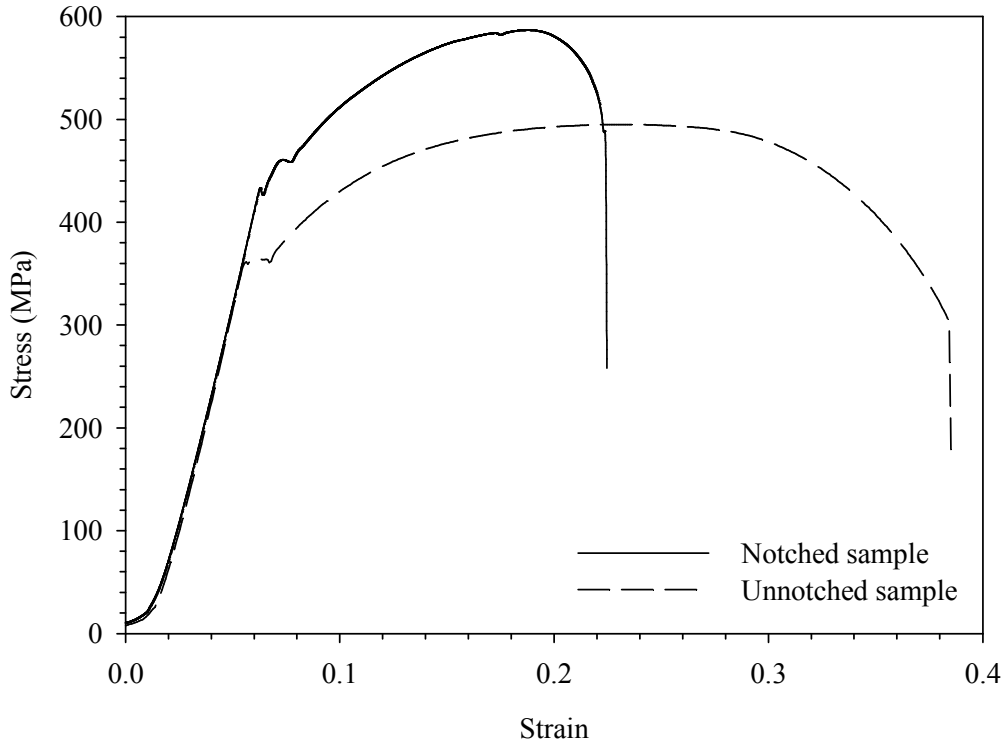

Figure 4.14. Typical stress-strain curves obtained for ASTM A709 Grade 50 steel tensile specimens.

Table 4.1. Summary of tensile properties.

Specimens	Elongation in 2" (%)		Area Reduction (%)		Yield Strength, offset 0.2% (MPa)		Ultimate Tensile strength (MPa)	
	Ave.	S.d.	Ave.	S.d.	Ave.	S.d.	Ave.	S.d.
PM_L	36.01	0.08	72.18	0.27	362.29	3.55	496.66	2.13
PM_T	35.43	1.10	71.02	1.42	366.78	0.73	502.70	0.27
PM_N	16.09	0.15	38.90	1.36	432.57	4.23	591.46	4.40

Ave. = Average value, S.d. = Standard deviation, PM_L = Unnotched specimens in longitudinal direction, PM_T = Unnotched specimens in transverse direction, PM_N = Notched specimens in transverse direction.

area of the notched specimens outside the notch was larger than that of the unnotched specimens (see Figure 3.11) and so the notched specimens could handle more load than the unnotched ones. However, the loads dropped very quickly once the maximum load was reached because of the stress raiser provided by the notch as shown in Figure 4.14.

Figure 4.15 shows typical stress-strain curves for transverse specimens submerged arc welded with four different heat inputs. A comparison of the tensile and yield strengths of the parent metal and welded specimens is shown in Figure 4.16. It can be seen from these figures that both the tensile and yield strengths remained practically unchanged as heat input increased. The tensile strength of welded and unwelded specimens varied from 485 MPa to 503 MPa, while the yield strength changed from 367 MPa to 394 MPa. A comparison of the percent elongation of the parent metal and welded specimens is shown in Figure 4.17. The elongation of the welded specimen was a combination of the elongation of the welded joint and that of the parent metal. The elongation of the WM and HAZ regions was less than that of the parent metal (Yang, 2008). Therefore, the elongation of the welded specimen was less than that of the parent metal.

Typical fracture locations on the parent metal and welded tensile specimens are shown in Figures 4.18 and 4.19, respectively. By etching with 5% Nital, the WM zones of the welded specimens were revealed. It could be observed that all the specimens fractured in the parent metal. Since all the welded specimens broke in the parent metal, it makes sense that the tensile and yield strengths of welded specimens were almost the same as those of the unwelded parent metal specimens. Yang (2008) and Hall (2010) also observed that the fracture occurred in the PM of the transverse weld tensile specimens. However, Prasad and Dwivedi (2008) found the transverse tensile specimens broke in the WM for the SAW HSLA steel, as the WM was weaker than the HAZ and PM. Neves and Loureiro (2004) found the specimens failed in the HAZ for the SAW steel RQT 601 because the HAZ of the welds was in the undermatch condition.

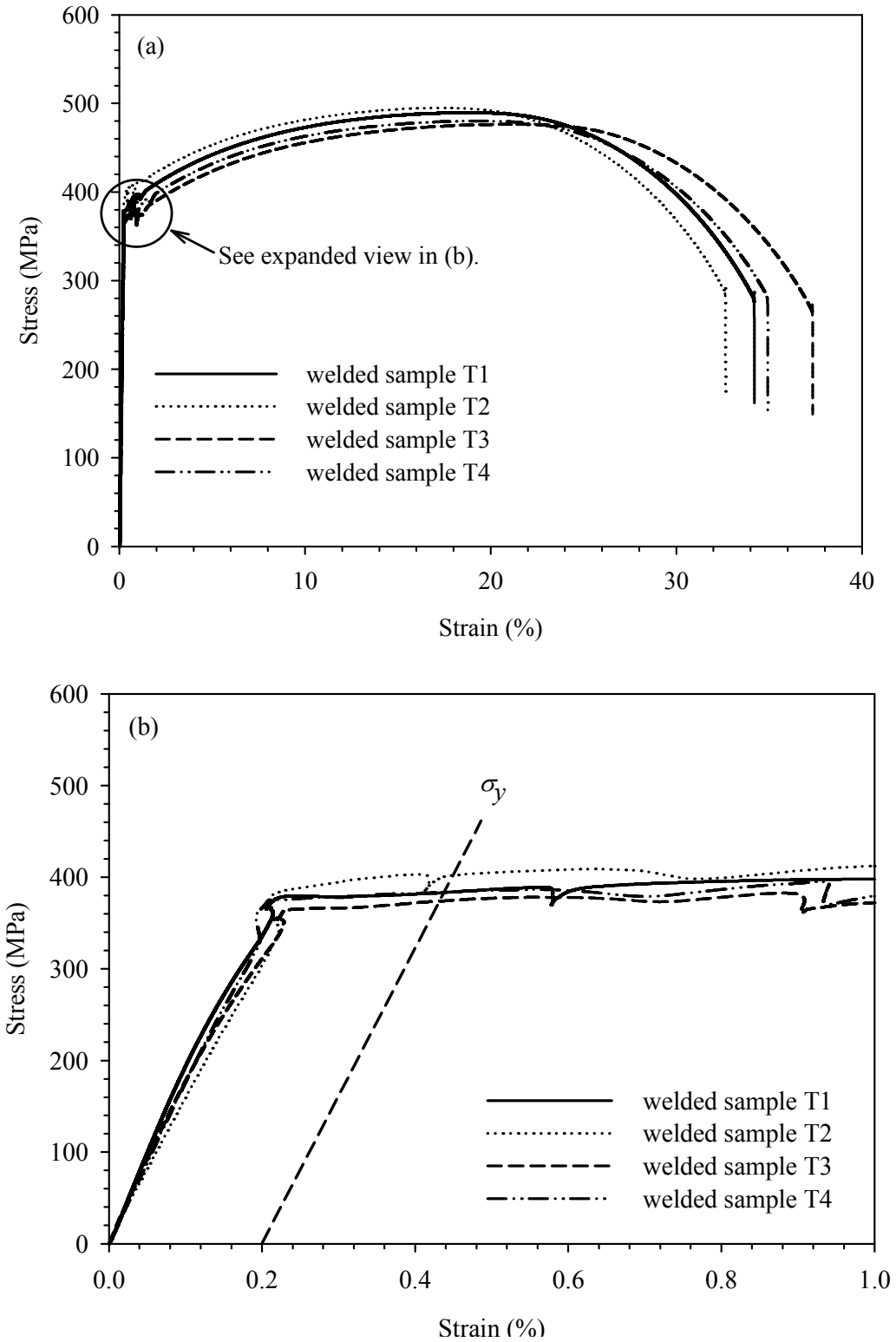

Figure 4.15. Typical stress-strain curves of SAW welded A709 Grade 50 steel: (a) stress-strain curves of welded specimens with different heat input and (b) expanded view of (a).

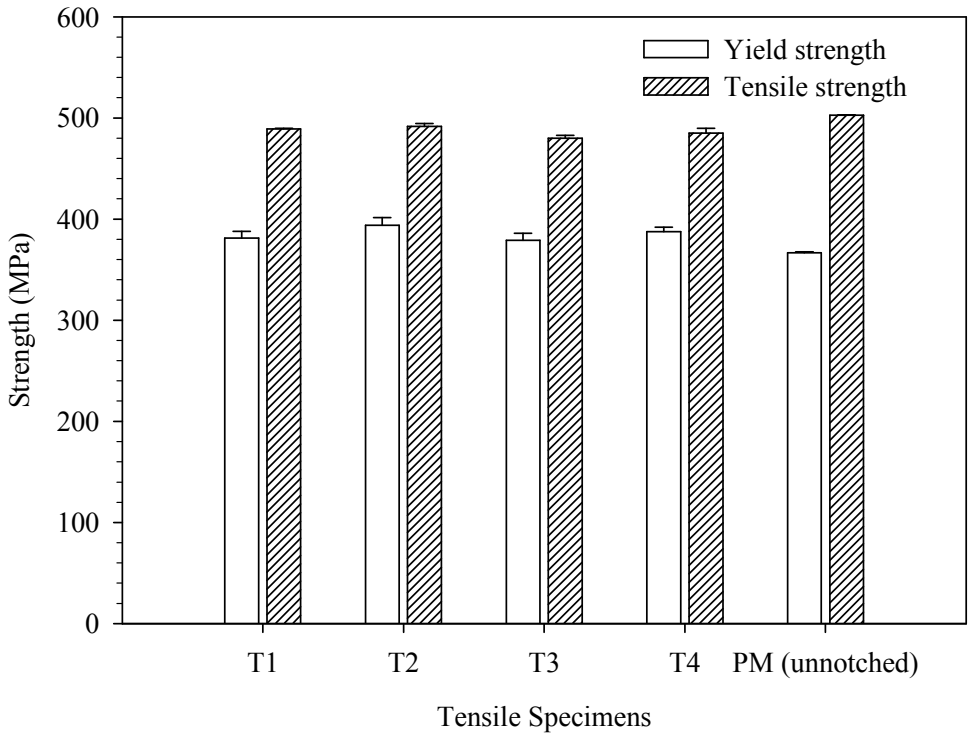

Figure 4.16. Tensile and yield strengths of welded/unwelded specimens.

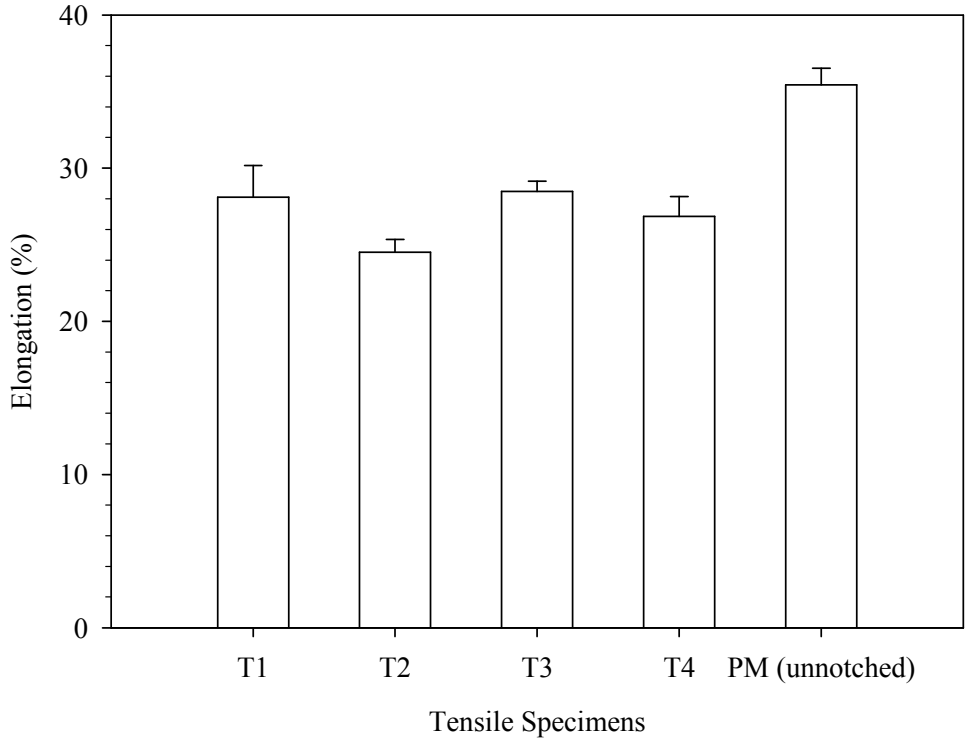

Figure 4.17. Percent elongation of welded/unwelded specimens.

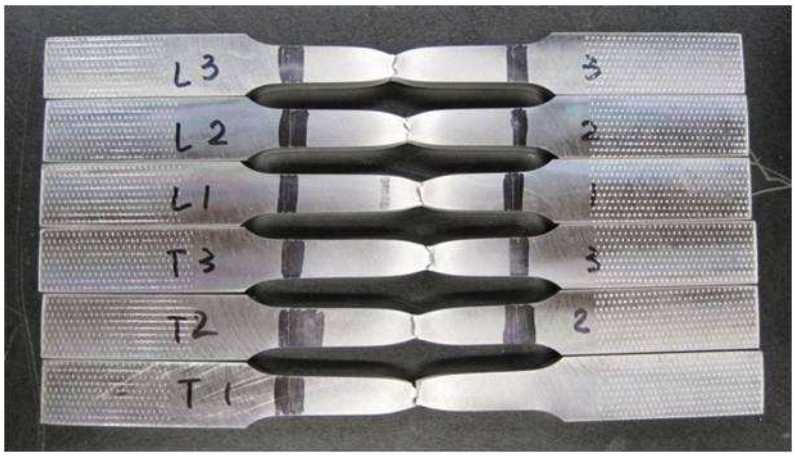

Figure 4.18. Fractured unnotched tensile specimens of the PM.

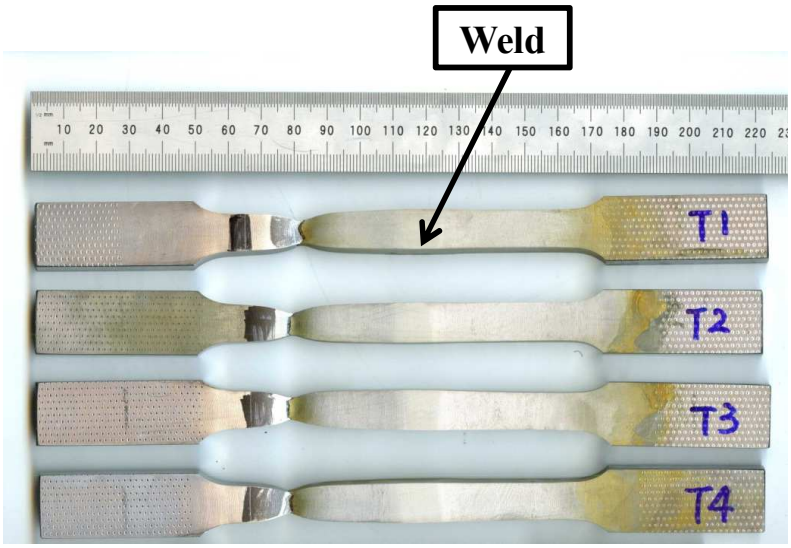

Figure 4.19. Fractured welded tensile specimens.

Typical SEM micrographs of fracture surfaces of tensile specimens for the PM and transverse welded joints are shown in Figure 4.20. As can be seen, for both the PM and welded specimens, similar ductile fracture surfaces were observed and consisted of many spherical dimples and some inclusions. Prasad and Dwivedi (2008) studied the SEM gractographs of tensile fractured surfaces which located in the WM and showed that the increase in the heat input increased area fraction of ductile fracture.

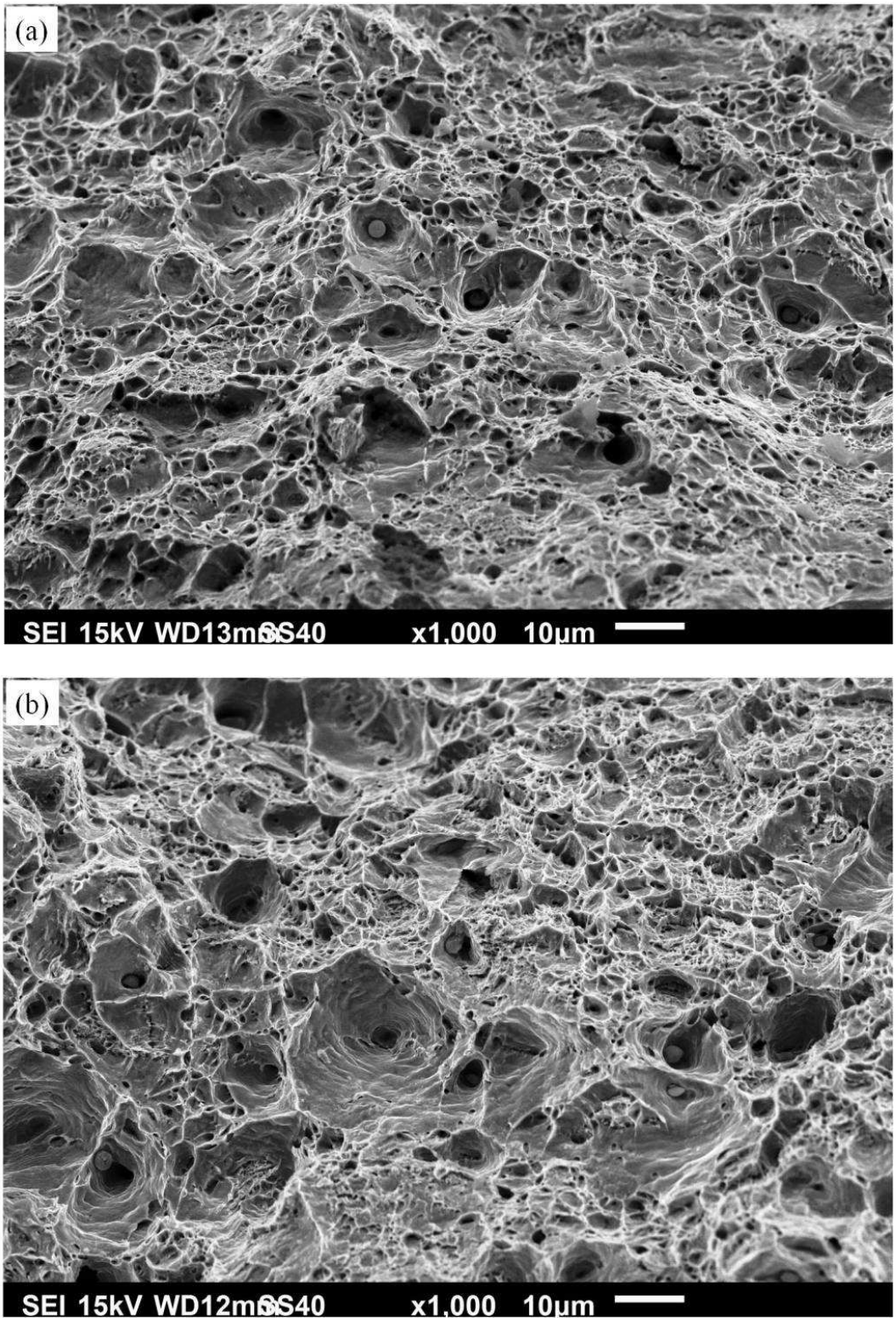

Figure 4.20. Typical SEM micrographs of fracture surfaces of tensile specimens: (a) the PM and (b) welded specimen (T1).

4.5 Fatigue Properties of ASTM A709 Grade 50 Steel and its Welds

High-cycle fatigue testing for unwelded (including unnotched and notched) and welded ASTM A709 Grade 50 steel was performed by a cantilever-type rotating bending fatigue machine operating at a frequency of 120 Hz at room and sub-zero temperatures (-20 °C and -30 °C) in laboratory air. Since the tensile strength (σ_u) of ASTM A709 Grade 50 steel was approximately 500 MPa and the estimated fatigue limit was between 250 MPa and 300 MPa, stress amplitudes (σ_a) varying from 250 MPa (50% of σ_u) to 425 MPa (85% of σ_u) were applied for the fatigue testing, and the mean stress (σ_m) was 0.

4.5.1 Fatigue Properties of A709 Steel at Room Temperature

Figure 4.21 shows the stress amplitude (σ_a) vs number of cycles to failure (N_f), i.e., *S-N* curve, for ASTM A709 Grade 50 steel. It can be seen that at first the stress amplitude rapidly dropped as the number of cycles increased, but the curve then flattened out and a small decrease in stress amplitude produced a large increase in number of cycles to failure. Generally, *S-N* curve can be expressed by a Basquin-type of relationship (Dowling, 1999):

$$\sigma_a = \sigma'_f \left(N_f\right)^b \tag{4.7}$$

where σ'_f is the fatigue strength coefficient and b the fatigue strength exponent. The values of σ'_f = 871.78 MPa and b = -0.070 were obtained from regression analysis of the

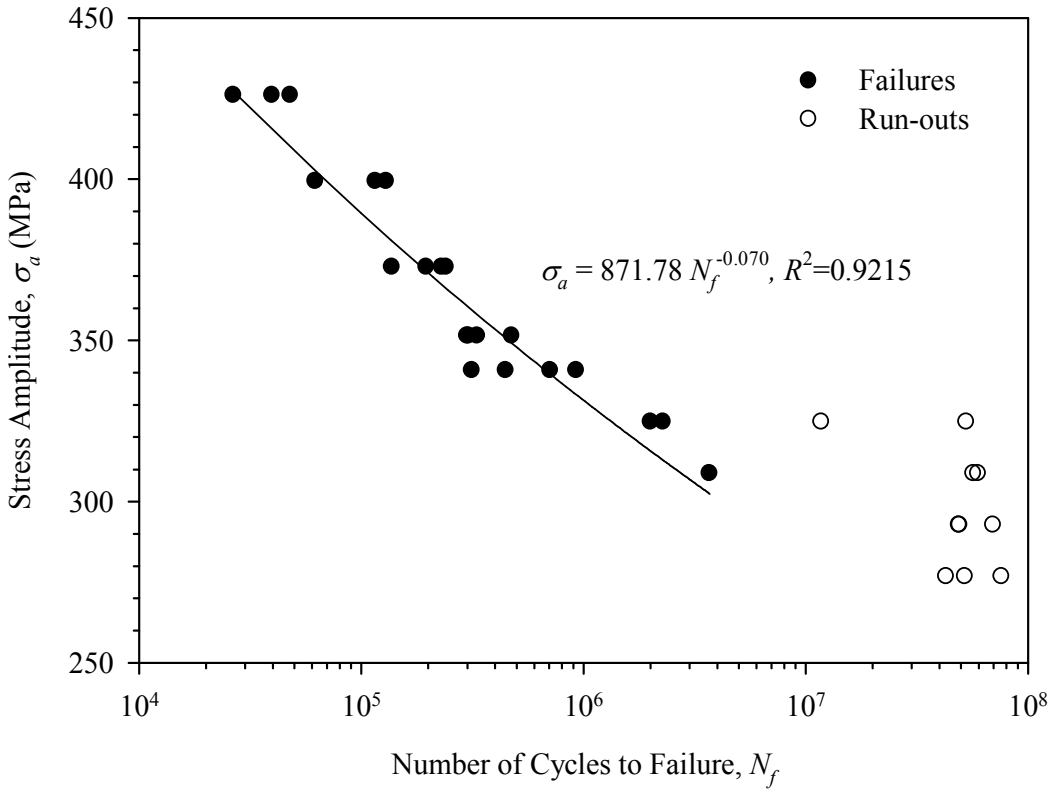

Figure 4.21. *S-N* plot for unnotched ASTM A709 Grade 50 steel specimens tested at room temperature.

S-N data shown in Figure 4.21. The test run-outs were excluded from the regression analysis (Chen *et al*., 2007). This is close to results reported by Chen *et al*. (2007) that σ'_f = 851 MPa and b = -0.069 for ASTM A709 Grade 70W steel, another steel grade in the A709 series.

The fatigue limit (or endurance limit) (σ_n) is defined as the stress amplitude level below which fatigue failure would not ordinarily take place (Dowling, 1999). As illustrated in Figure 4.21, two run-outs and one failure at about 3.7×10^6 cycles were obtained at the stress amplitude of 309 MPa and three run-outs at 293 MPa, indicating that the fatigue limit was between 293 MPa and 309 MPa. The endurance ratio (σ_n/σ_u) was about 0.6.

Another method for determining fatigue limit of steels and alloys is to use the fatigue strength at 2×10^6 cycles (Gurney, 1968; Magudeeswaran *et al*., 2007; Miki *et al*., 2002). According to this method, a fatigue limit of 315 MPa was obtained for ASTM A709 Grade 50 steel, which is close to the range of 293 MPa to 309 MPa obtained in the present study.

The total fatigue life, shown in Figure 4.21, actually, is the sum of number of cycle for fatigue crack initiation and fatigue crack propagation (Pook, 2007). However, most of the lives of metallic specimens are associated with the crack initiation stage (Frost, 1999; Pook, 2007). For small specimens, near the fatigue limit, up to 90% of the fatigue life is contributed by crack initiation, while at high stress amplitude levels, crack propagation becomes important.

Typical SEM fractographs obtained from the fracture surface of a typical fatigue specimen of the parent metal of ASTM A709 Grade 50 steel, which failed at 3.7×10^6 cycles at the stress amplitude of 309 MPa, are shown in Figure 4.22. Fatigue failure usually occurs in three stages, namely, crack initiation, crack propagation and fracture. The fatigue crack propagation stage (area 1) and fracture stage (area 2) are identified in Figure 4.22 (a). Striations shown in Figure 4.22 (b) were the main features of the crack propagation stage and revealed the presence of marks left by the progress of the fatigue fracture from every cycle. By counting the number of striations within given certain length, average striation spacing values within the counting area were obtained (see Figure 4.22 (b)). Figure 4.22 (c) shows a dimple rupture, which was the feature of the last stage of the fatigue failure.

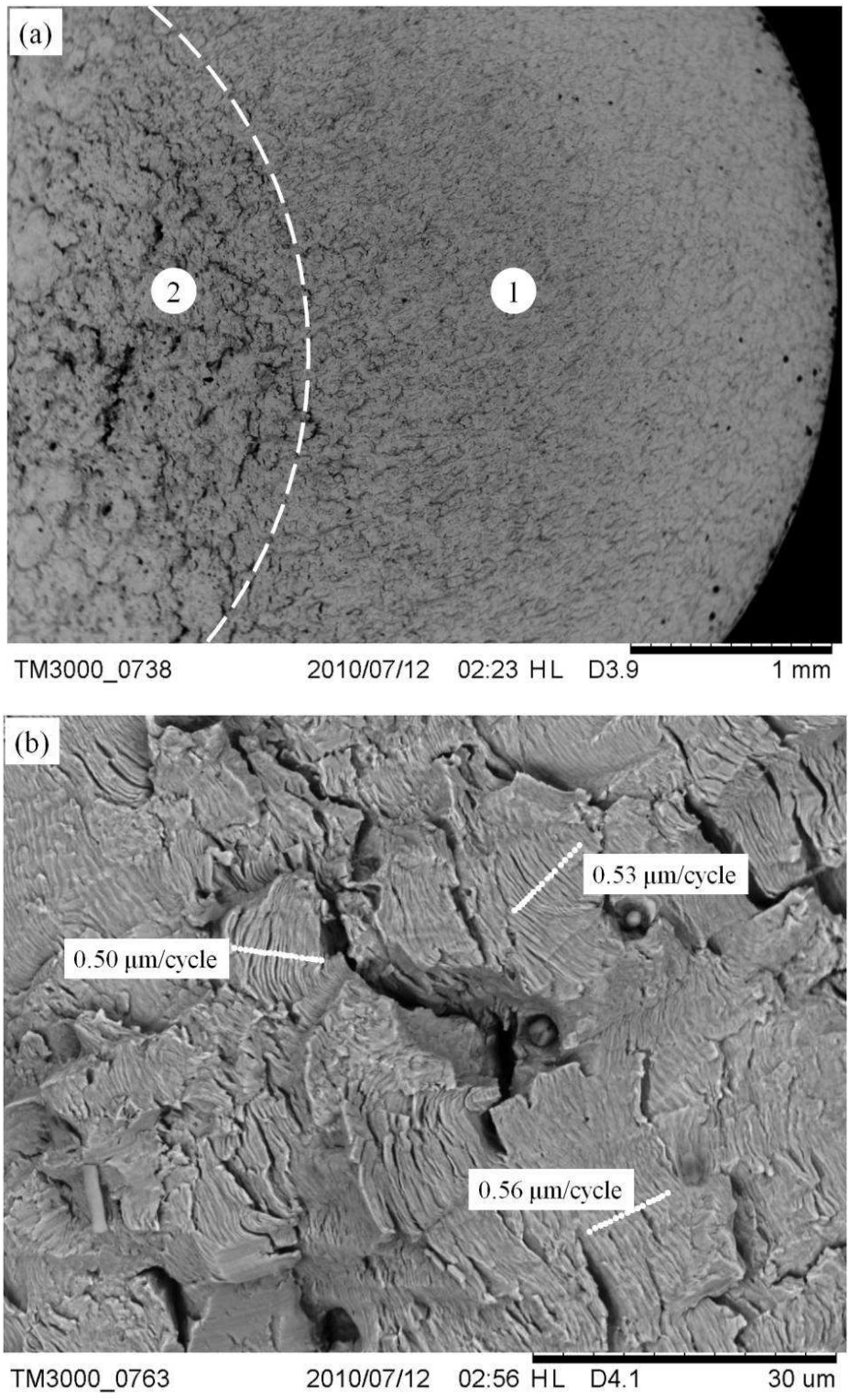

Figure 4.22. Secondary electron SEM fractographs obtained from the fracture surface of a fatigue specimen of the parent metal tested at room temperature: (a) an overview showing area 1, crack propagation stage and area 2, fracture stage, (b) fracture surface within area 1, and (c) fracture surface within area 2.

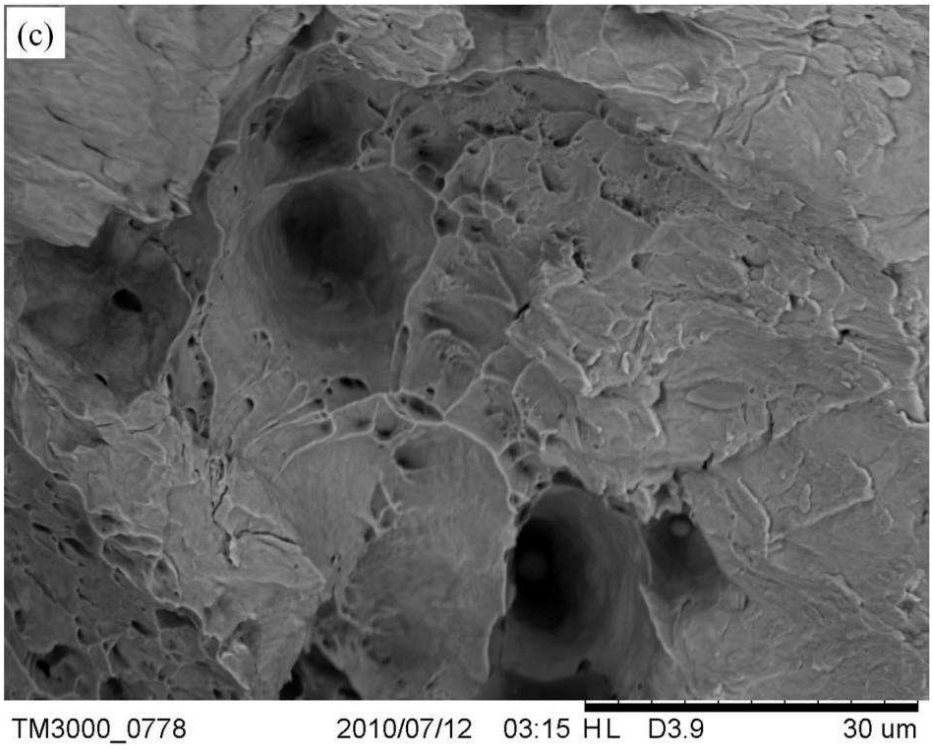

Figure 4.22 continued.

Figure 4.23 shows optical macrographs of fracture surfaces of fatigue specimens of the parent metal tested under different stress amplitude levels. As can be seen, the fracture surface of specimens tested under low stress amplitude condition was rougher than that of specimens tested at high stress amplitude. Additional SEM fractographs and optical macrographs of fracture surfaces of fatigue specimens are presented in Appendix B.

4.5.2 Effect of Notch on Fatigue Properties of A709 Steel at Room Temperature

Figure 4.24 shows *S*-*N* curves for the unnotched and notched specimens of the parent metal of ASTM A709 Grade 50 steel. The stress amplitude of the notched specimens was calculated by the nominal stress without consideration of the stress concentration effects. The values of σ'_f = 1471.1 MPa and b = -0.144 were obtained for *S*-*N* curve of

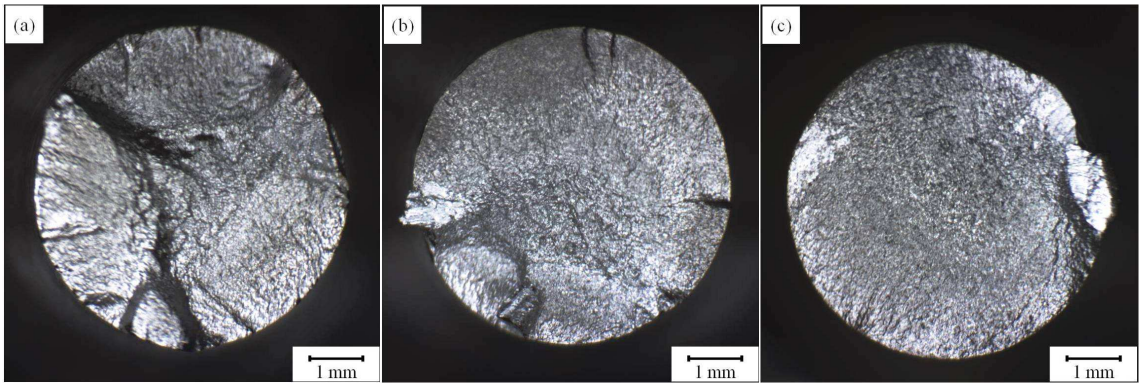

Figure 4.23. Optical macrographs showing fracture surfaces of fatigue specimens of the parent metal of ASTM A709 Grade 50 steel: (a) failed at 2.6×10^4 cycles at the stress amplitude of 426 MPa, (b) failed at 2.4×10^5 cycles at the stress amplitude of 373 MPa, and (c) failed at 2.3×10^6 cycles at the stress amplitude of 325 MPa.

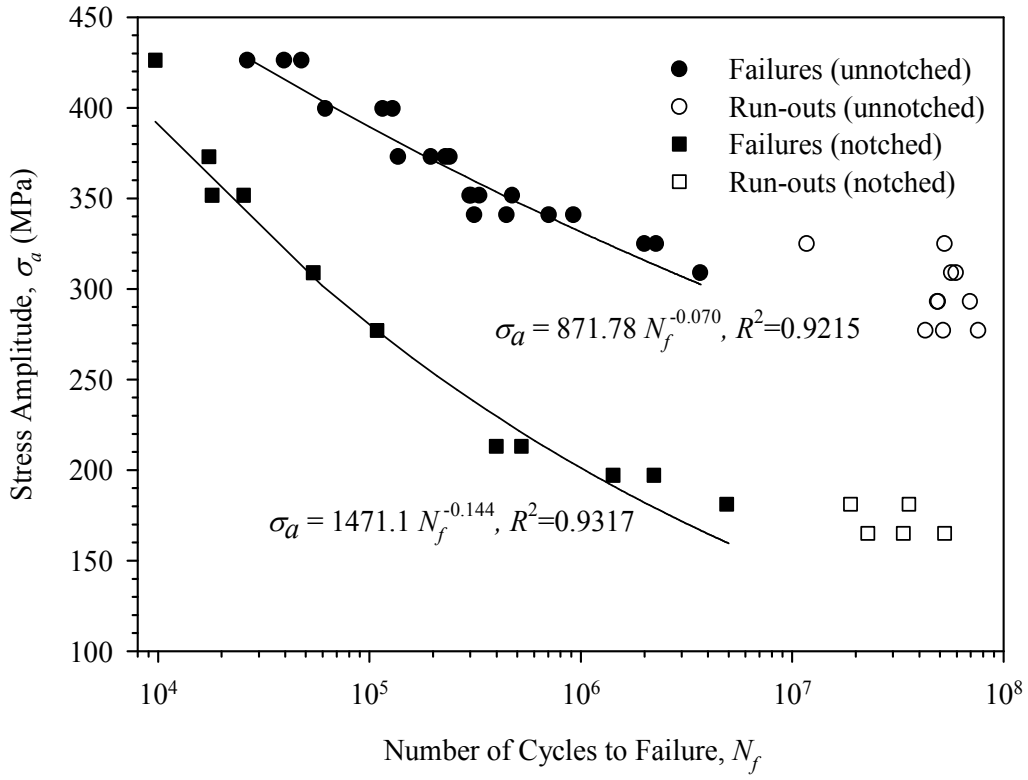

Figure 4.24. *S-N* plots for unnotched and notched ASTM A709 Grade 50 steel specimens at room temperature.

the notched specimens (Table 4.2). There were two run-outs and one failure at about 4.0×10^6 cycles at a stress amplitude of 165 MPa and three run-outs at 180 MPa, suggesting that the fatigue limit of notched specimens was between 165 MPa and 180 MPa.

Compared to the unnotched specimens of the parent metal, the notched ones had shorter fatigue life at the same stress amplitude. Fatigue strengths at 2×10^6 cycles for unnotched and notched specimens were 315.7 MPa and 190.8 MPa, respectively (Table 4.2). This indicates that the fatigue stress concentration factor was K_f = 315.7 MPa / 182.1 MPa = 1.73, which is close to the calculated fatigue stress concentration factor of 1.79 (see Appendix A).

The fatigue life of the notched specimen represents the sum of the number of cycles required to initiate a fatigue crack and the number of cycles required to propagate it to final failure. For small stress concentration factors, K_t, fatigue life is dominated by crack initiation, just like the unnotched specimen. For large K_t, notch root might be the site of initiation of a fatigue crack, and thus fatigue life is then dominated by fatigue crack propagation.

Typical SEM images obtained from a fracture surface of a notched fatigue specimen of the parent metal are shown in Figure 4.25. Optical micrographs of fracture surfaces for notched specimens tested at different stress amplitude levels are shown in Figure 4.26. Fatigue crack propagation stage (area 1) and fracture stage (area 2) can be identified in

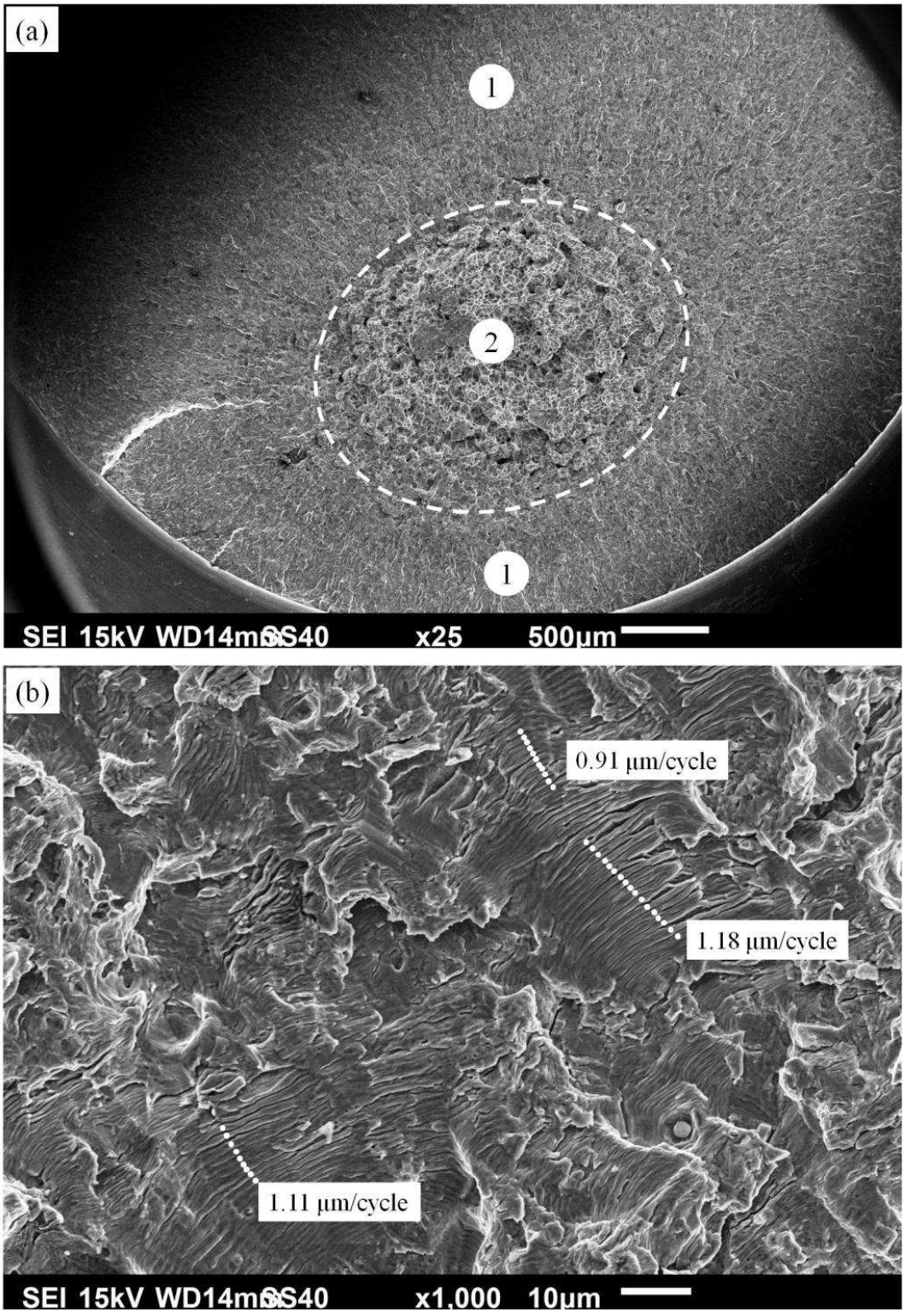

Figure 4.25. Typical secondary electron SEM fractographs from a fracture surface of notched fatigue specimen of the parent metal at room temperature: (a) an overall look showing crack propagation stage and fracture stage, (b) fatigue fracture surface showing striations, and (c) ductile fracture surface.

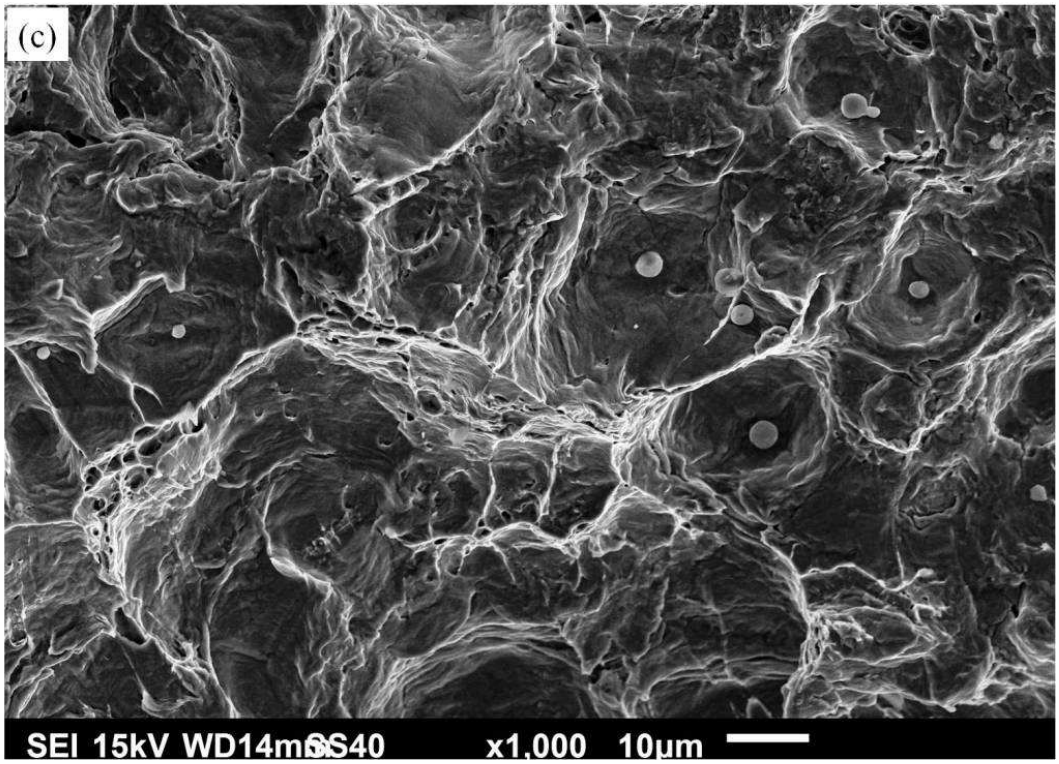

Figure 4.25 continued.

Table 4.2. Fatigue properties of unnotched and notched specimens obtained at room teperature.

Specimens	Fatigue strength coefficient, σ'_f (MPa)	Fatigue strength exponent, b	Fatigue strength at 2×10^6 cycles (MPa)
PM (unnotched)	871.78	-0.070	315.7
PM (notched)	1471.1	-0.144	182.1

Figure 4.25 (a). Crack nucleation occurred at several locations, which could be observed in Figure 4.26. Figure 4.25 (b) shows a typical topography having radial ridge pattern parallel to the crack propagation direction. The striations shown in Figure 4.25 (b) had an average striation spacing of 1.07 μm. A ductile rupture, which is the last stage of fatigue failure, is shown in Figure 4.25 (c).

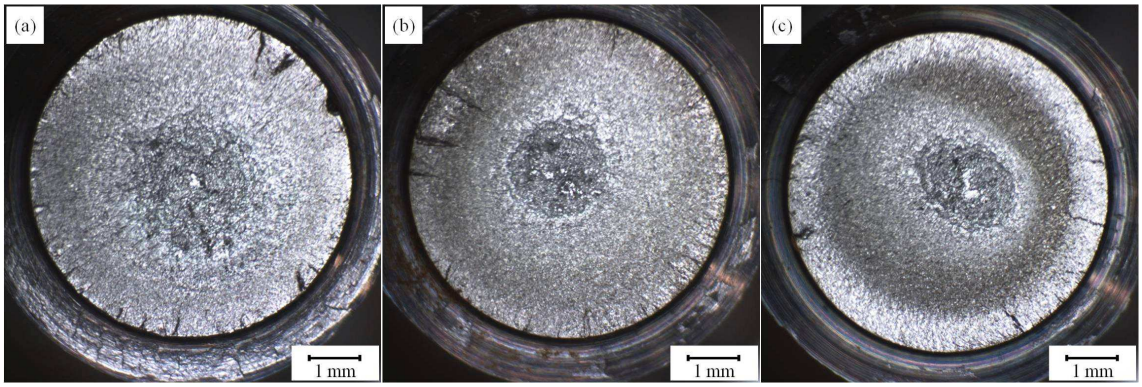

Figure 4.26. Fracture surfaces of notched fatigue specimens: (a) failed at 1.8×10^4 cycles at the stress amplitude of 352 MPa, (b) failed at 5.2×10^5 cycles at the stress amplitude of 213 MPa, and (c) failed at 1.4×10^6 cycles at the stress amplitude of 197 MPa.

4.5.3 Effect of Heat Input on Fatigue Properties of Welded A709 Steel at Room Temperature

The *S-N* curves obtained at room temperature for welded specimens produced using four different heat inputs are shown in Figure 4.27. The values of constants σ'_f and b obtained from these *S-N* curves are summarized in Table 4.3. The fatigue strengths of the welded specimens at 2×10^6 cycles are also listed in Table 4.3. As can be seen in Table 4.3, the fatigue strength of the welded specimens changed slightly from that of the unwelded PM, suggesting that heat input did not have an appreciable effect on the fatigue strength of SAW ASTM A709 Grade 50 steel joints at room temperature. Previous research works have shown that the fatigue strength of welded steel joints was appreciably affected by the weld bead geometry (Gurney, 1968; Ninh and Wahab, 1995a; Ninh and Wahab, 1995b; Ninh and Wahab, 1998; Lee *et al*., 2009). However, weld bead geometry did not play a role in this study because of the way the welded fatigue specimens were cut off from the welded plates. As shown in Figure 3.14, the welded fatigue specimens were machined from the second side of welded plates and included the WM, HAZ and

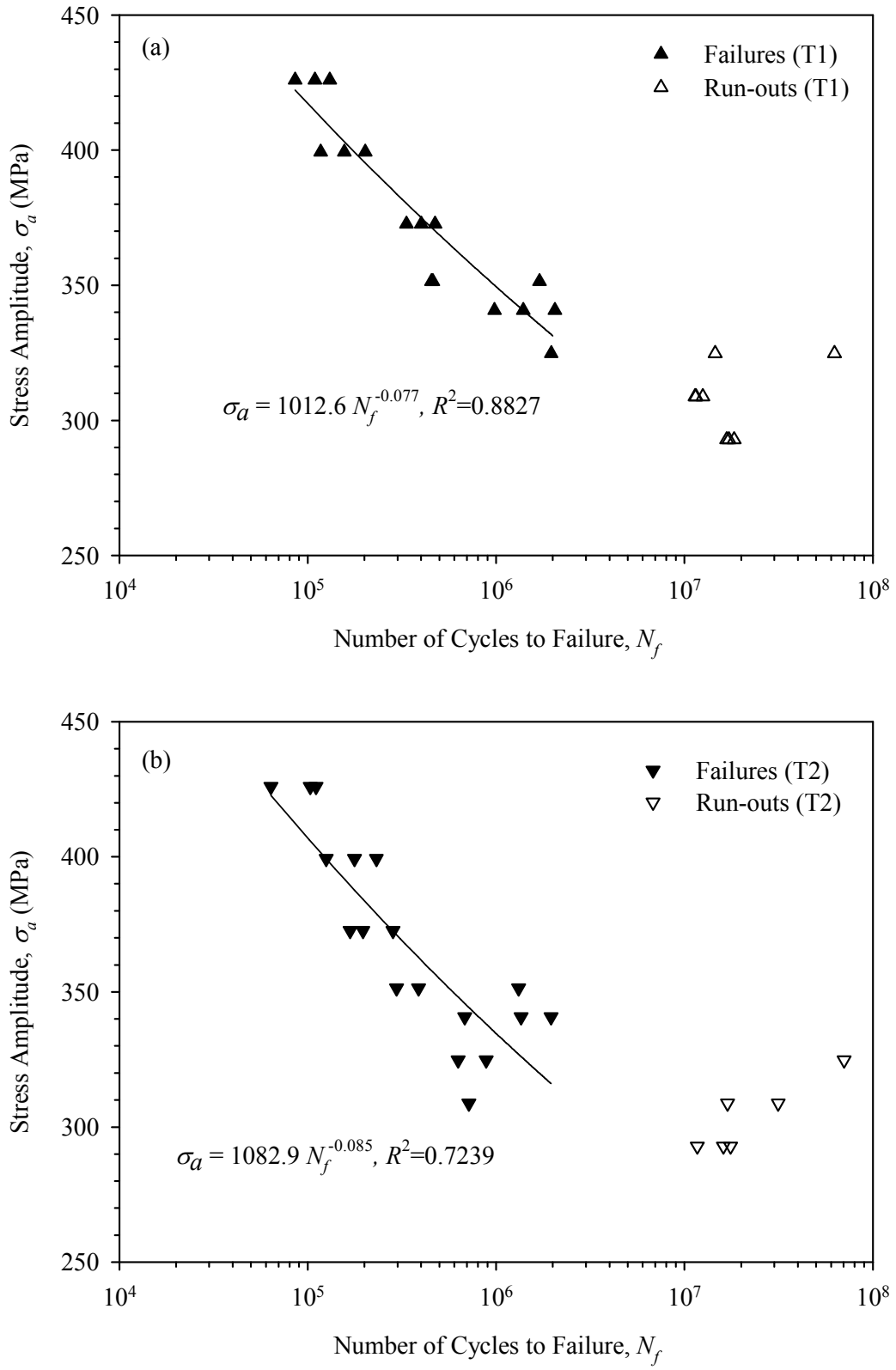

Figure 4.27. *S-N* plots for welded ASTM A709 Grade 50 steel specimens at room temperature: (a) T1, (b) T2, (c) T3, and (d) T4.

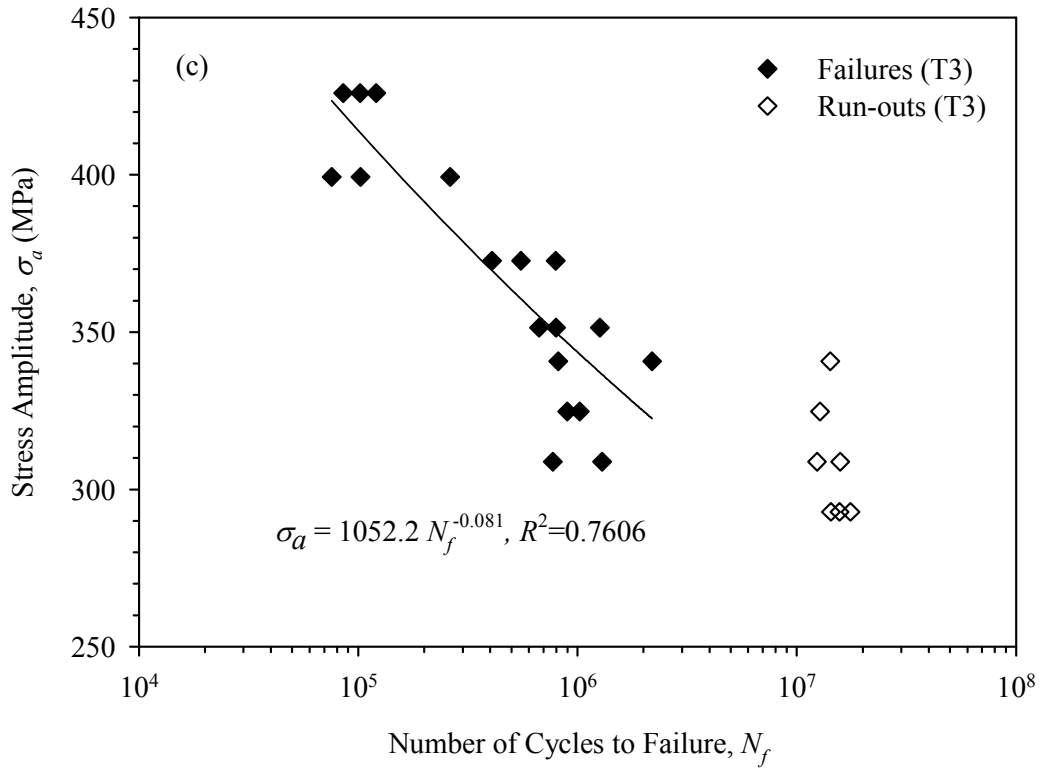

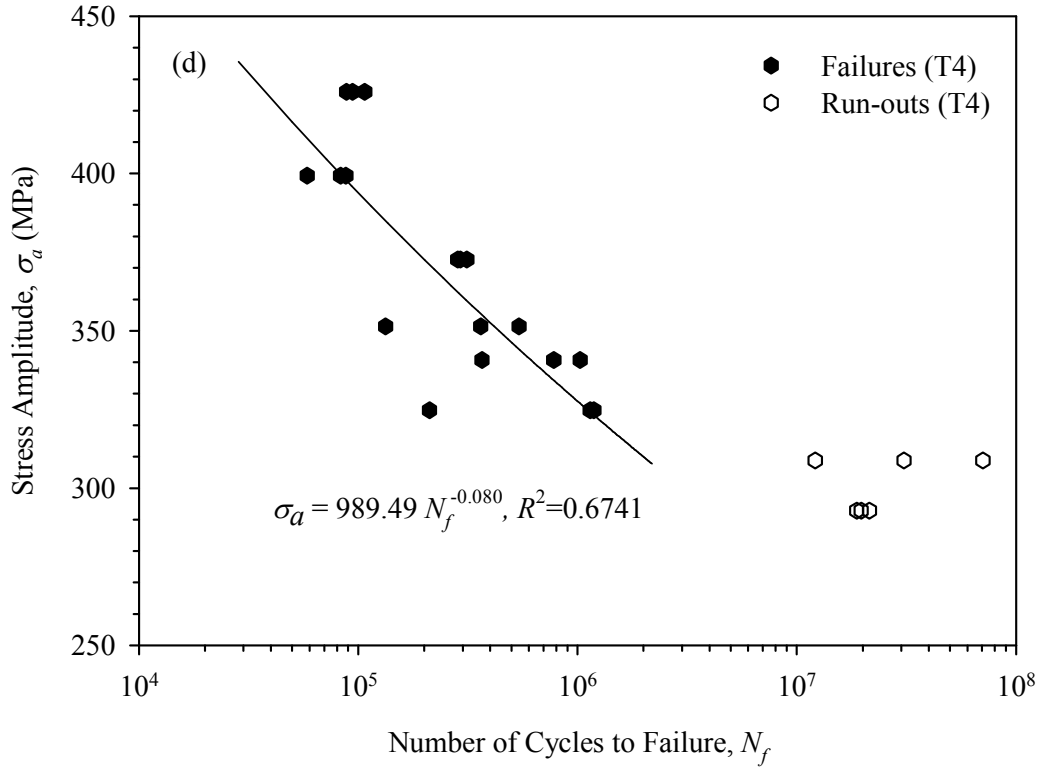

Figure 4.27 continued.

Table 4.3. Fatigue strengths of parent metal specimens and welded specimens at room temperature.

Specimens	Fatigue strength coefficient, σ'_f (MPa)	Fatigue strength exponent, b	Fatigue strength at 2×10^6 cycles (MPa)	Fatigue strength difference (%)
PM (unnotched)	871.78	-0.070	315.7	-
T1	1012.6	-0.077	331.3	4.94%
T2	1082.9	-0.085	315.5	0.00%
T3	1052.2	-0.081	324.9	2.91%
T4	989.49	-0.080	310.0	-1.81%

PM. Previous works also showed that the fatigue strength of welded joints also depended on material properties such as microstructure, hardness, and tensile strength (Forrest, 1962; Jang *et al*., 2010). It was found in this study that most welded fatigue specimens failed in the FGHAZ. For different heat inputs, the microstructure and hardness of the HAZ did not change appreciably. So this might be another reason why heat input had only slight effect on the fatigue strength of SAW ASTM A709 Grade 50 steel joints at room temperature in this study.

Typical secondary electron SEM images obtained from the fracture surface of a fatigue specimen produced using a heat input of 3.03 kJ/mm are shown in Figure 4.28. Fatigue crack propagation stage (area 1) and fracture stage (area 2) could be readily identified in Figure 4.28 (a). Figure 4.28 (b) shows the transition from fatigue crack propagation stage to the final ductile fracture stage. Figure 4.28 (c) shows fatigue crack growth around an inclusion. Figure 4.29 shows optical macrographs of fracture surfaces of fatigue specimens of plate T1 tested under different stress amplitude levels. The fracture

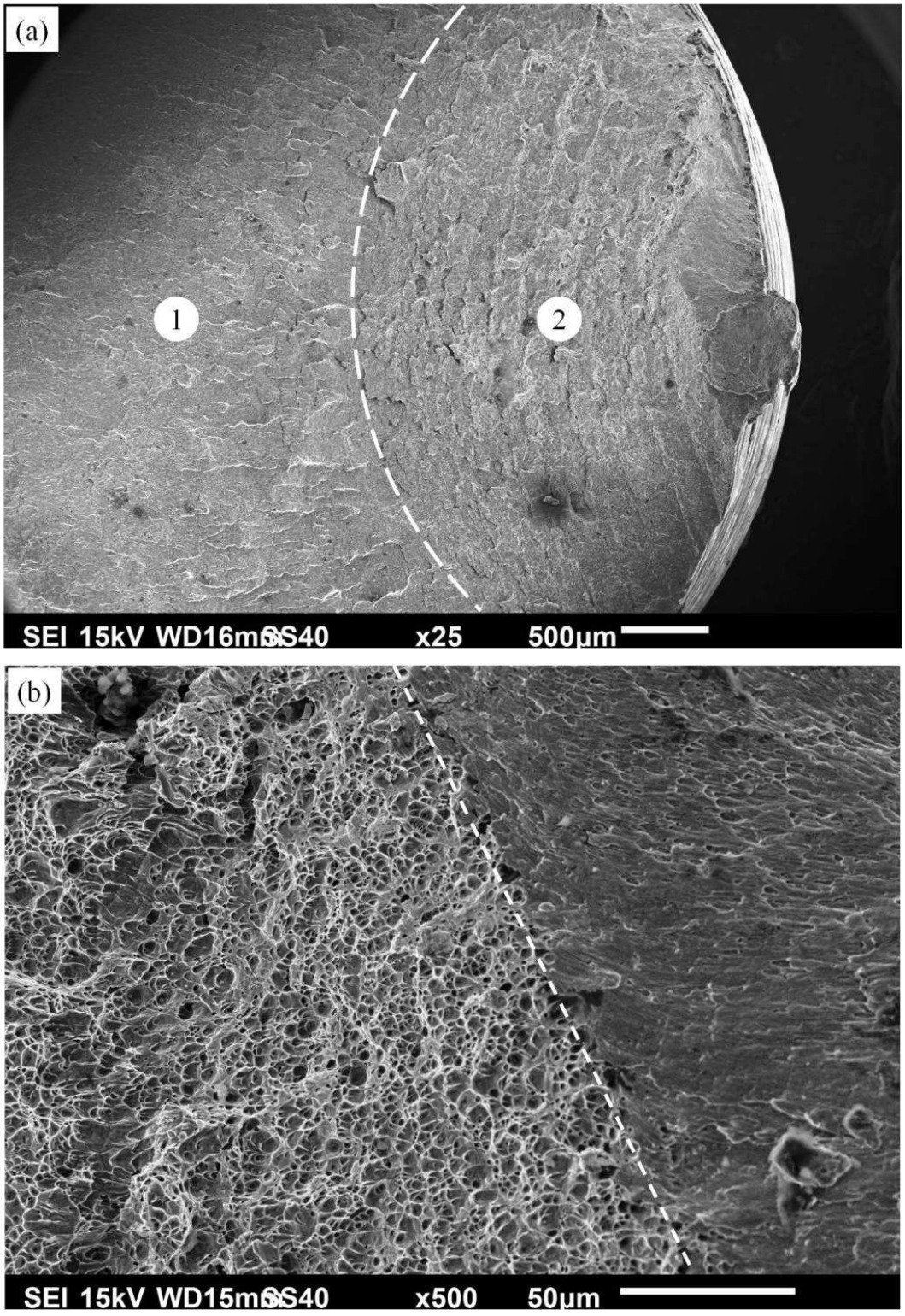

Figure 4.28. Secondary electron SEM micrographs from a fracture surface of welded fatigue specimen (T1) at room temperature: (a) low magnification image showing crack propagation stage and fracture stage, (b) transition from fatigue fracture to dimple fracture, and (c) fracture surface showing striations.

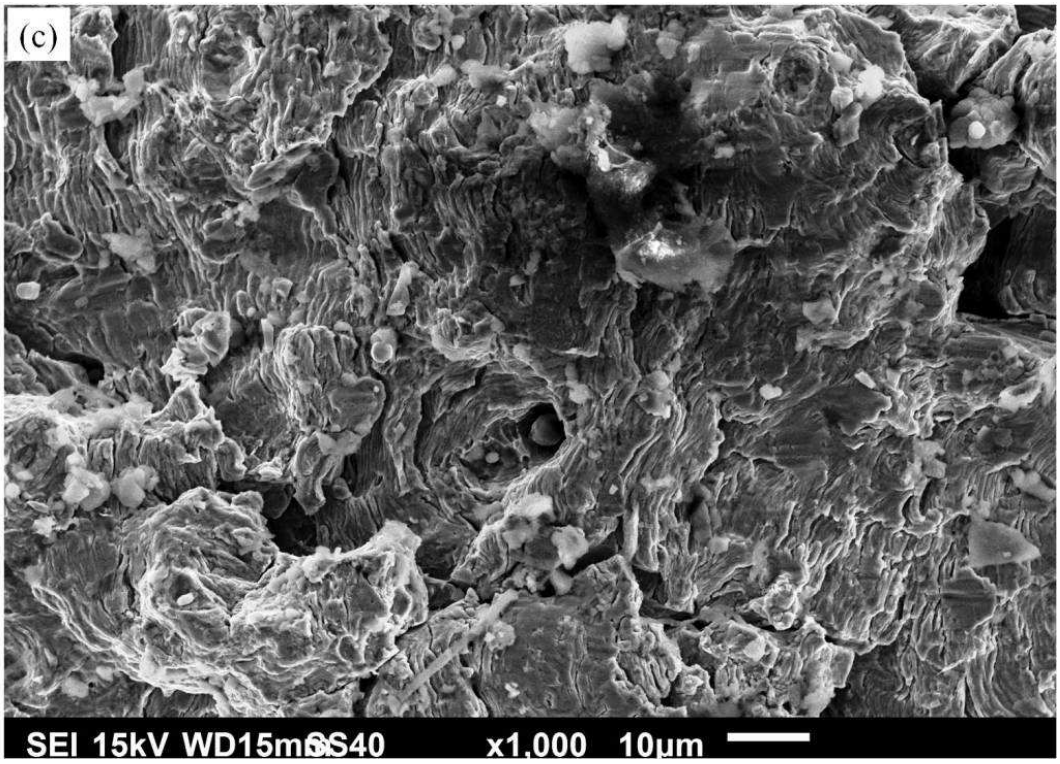

Figure 4.28 continued.

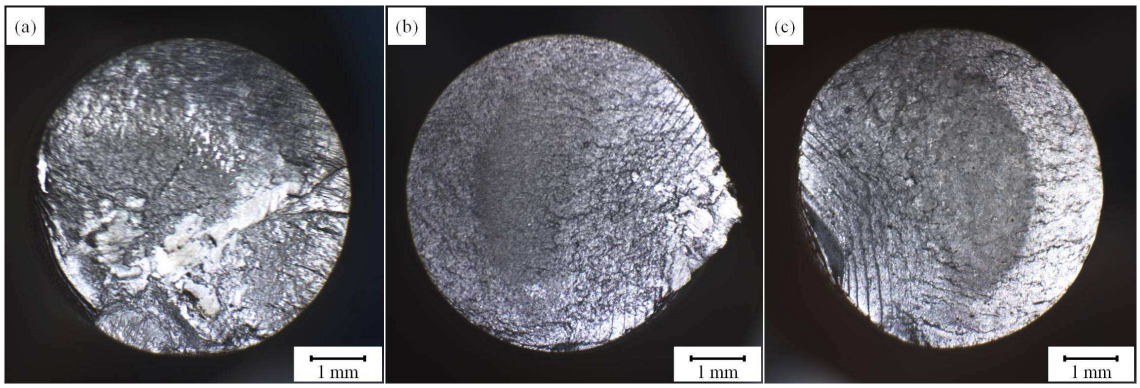

Figure 4.29. Optical macrographs showing fracture surfaces of fatigue specimens of plate T1: (a) failed at 1.3×10^4 cycles at the stress amplitude of 426 MPa, (b) failed at 3.3×10^5 cycles at the stress amplitude of 373 MPa, and (c) failed at 2.0×10^6 cycles at the stress amplitude of 325 MPa.

surface of specimen tested under high stress amplitude was flatter than those of specimen tested under low stress amplitudes. More SEM images of fracture surfaces of welded fatigue specimens are presented in Appendix B.

To further understand where the fatigue crack started, a cross-session including the fracture surface as the top was cut from the ruptured fatigue specimen, polished, etched and examined in a Nikon MA100 optical microscope. Figure 4.30 shows the micrograph of the section. On close examination, it was found that fatigue crack initiation, propagation and final rupture occurred in the FGHAZ. A few other fracture specimens examined showed that fatigue failure took place in the FGHAZ.

4.5.4 Effect of Sub-zero Temperatures on Fatigue Properties of Parent Metal and Welded A709 Steel

The *S-N* plots obtained from fatigue testing at -20 °C of specimen of unnotched parent metal, notched parent metal and welded joints are shown in Figure 4.31. It can be seen from Figure 4.31 that the fatigue strengths of all the specimens were generally higher at -20 °C than at room temperature. Figure 4.32 shows the fatigue test data obtained at -20 °C and -30 °C for unnotched parent metal, notched parent metal and welded specimens. With a decrease in temperature from -20 °C to -30 °C, the fatigue strength of the tested specimens increased appreciably. A comparison of the fatigue strengths at 2×10^6 cycles for both parent metal and welded specimens at room temperature, -20 °C and -30 °C are shown in Figure 4.33. The ratio of fatigue strengths of the specimens tested at -20 °C and -30 °C to the fatigue strength at room temperature is summarized in Table 4.4. As

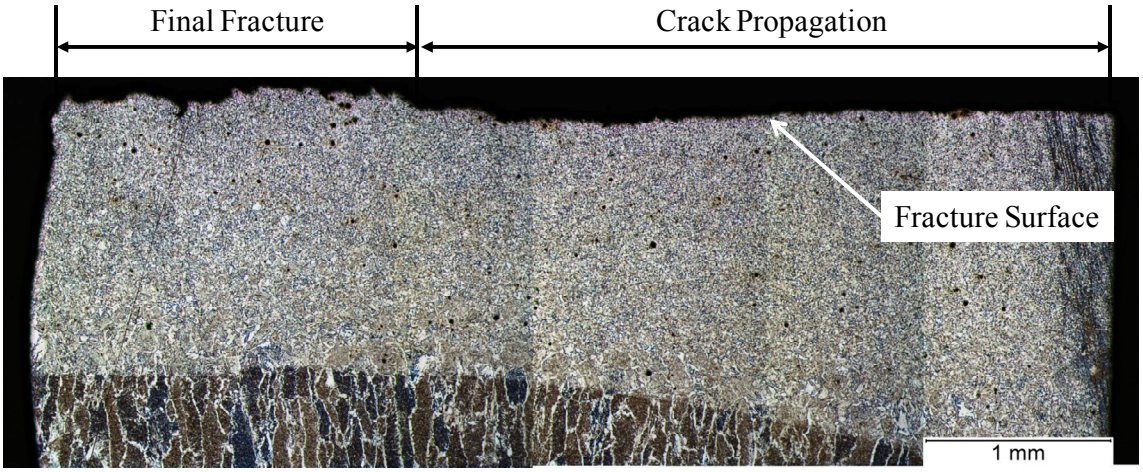

Figure 4.30. Micrograph showing the location where fatigue crack occurred.

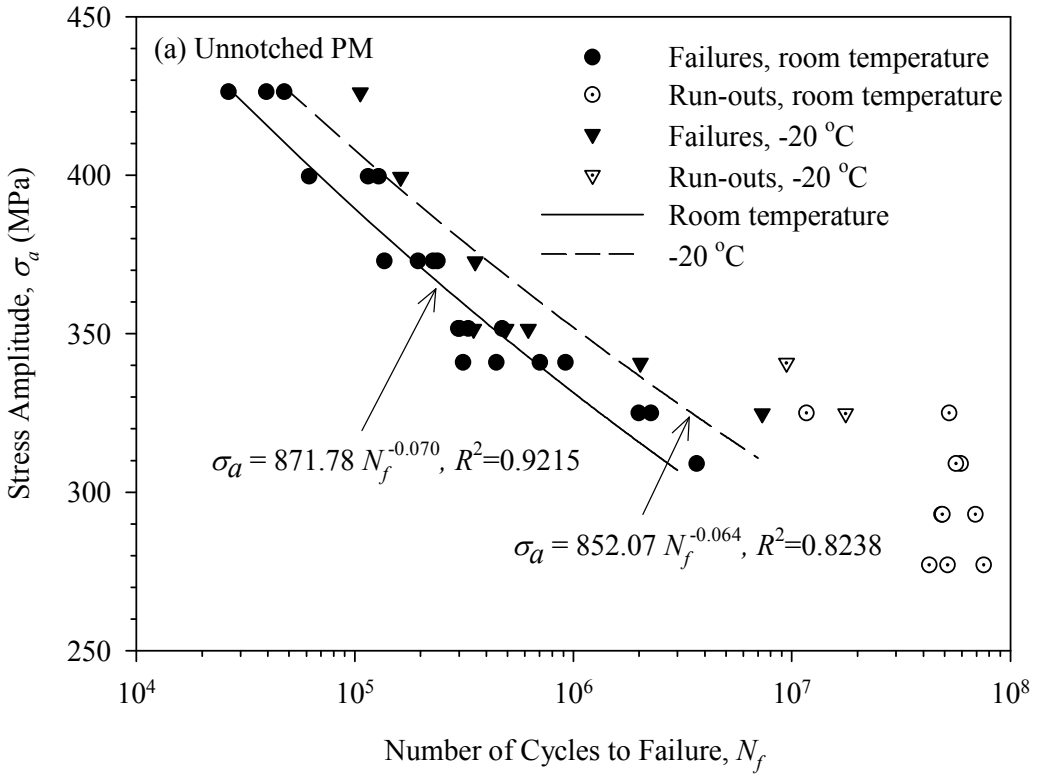

Figure 4.31. *S-N* plots for welded A709 steel specimens tested at room temperature and -20 °C: (a) unnotched PM, (b) notched PM, (c) plate T1, (d) plate T2, (e) plate T3, and (f) plate T4.

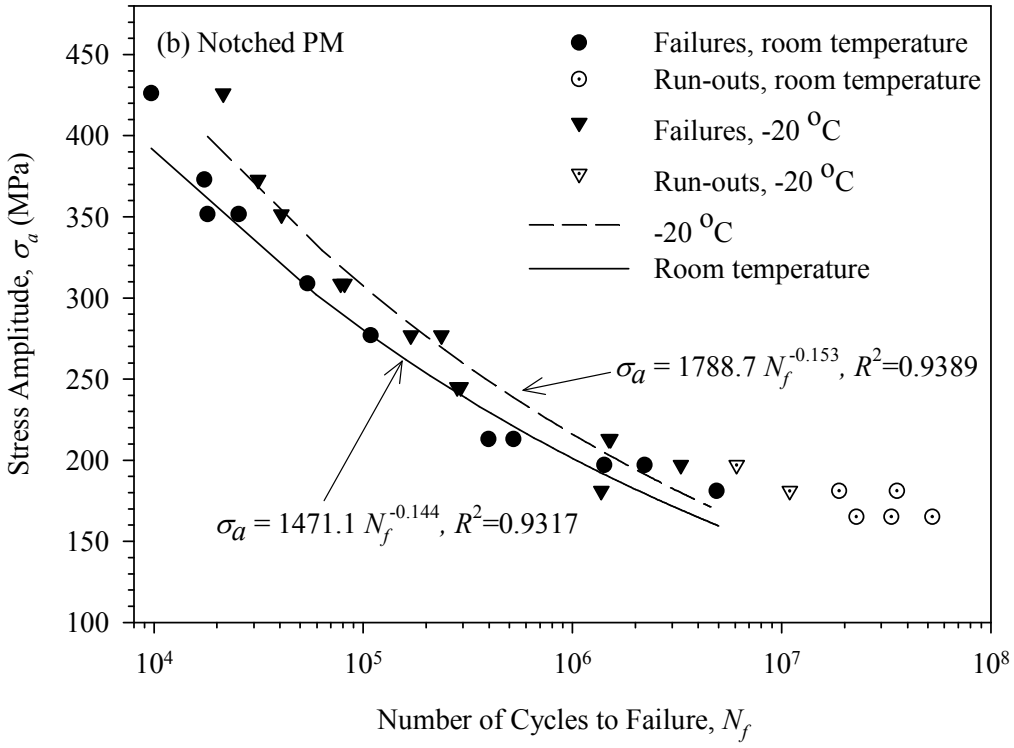

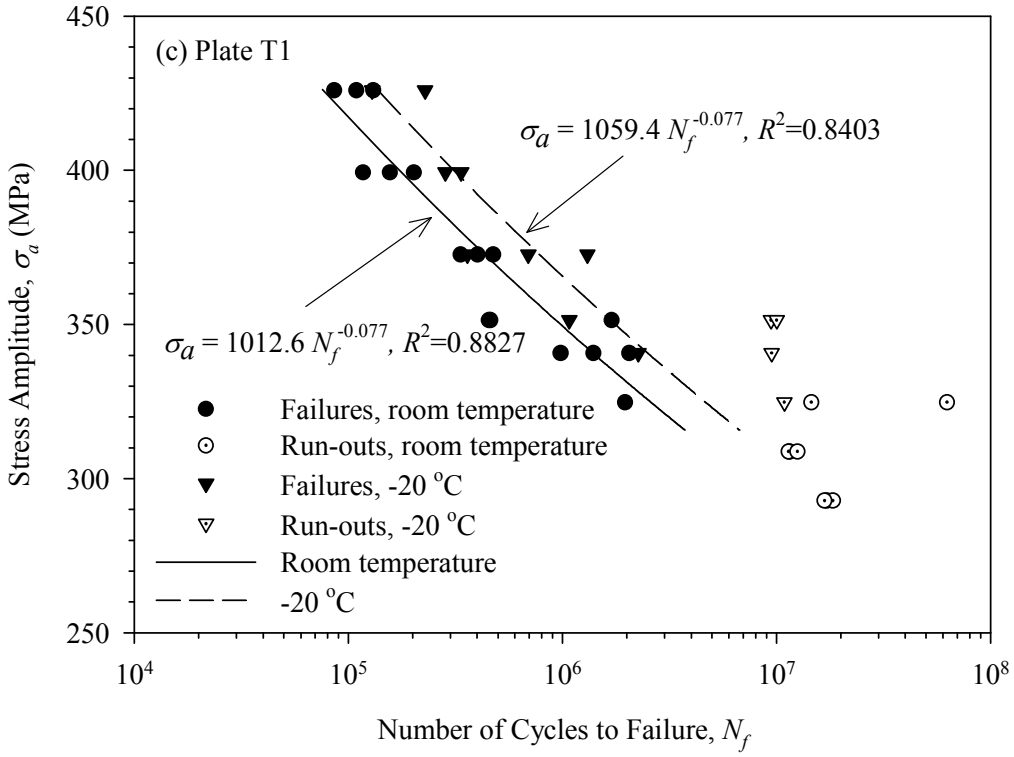

Figure 4.31 continued.

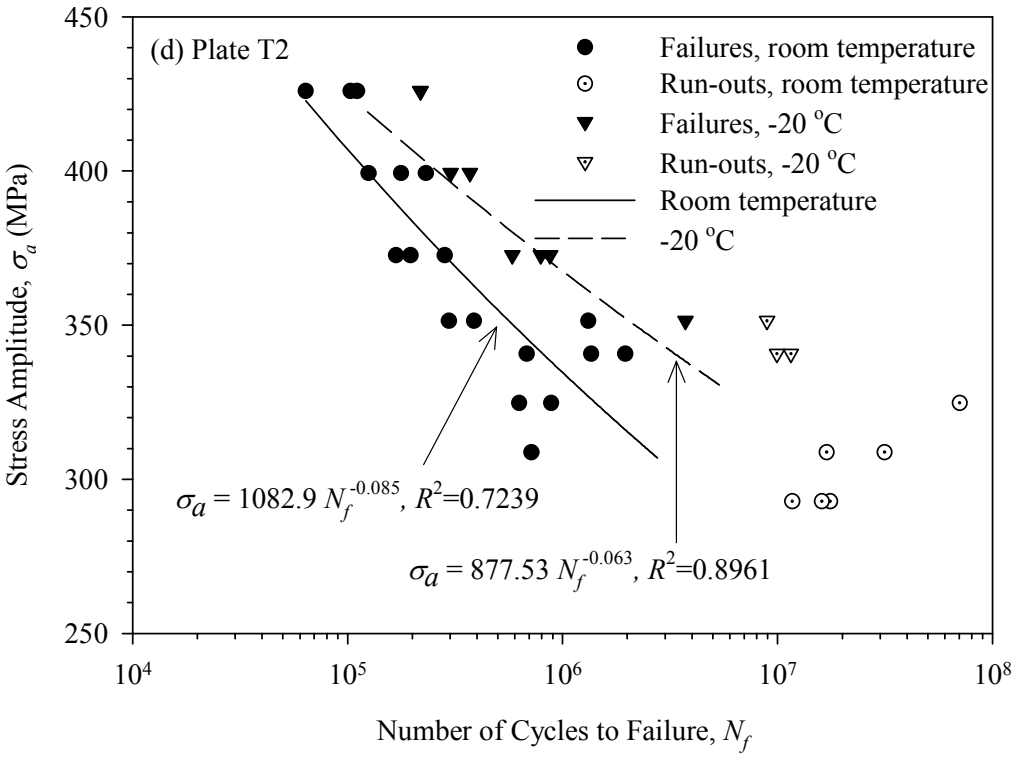

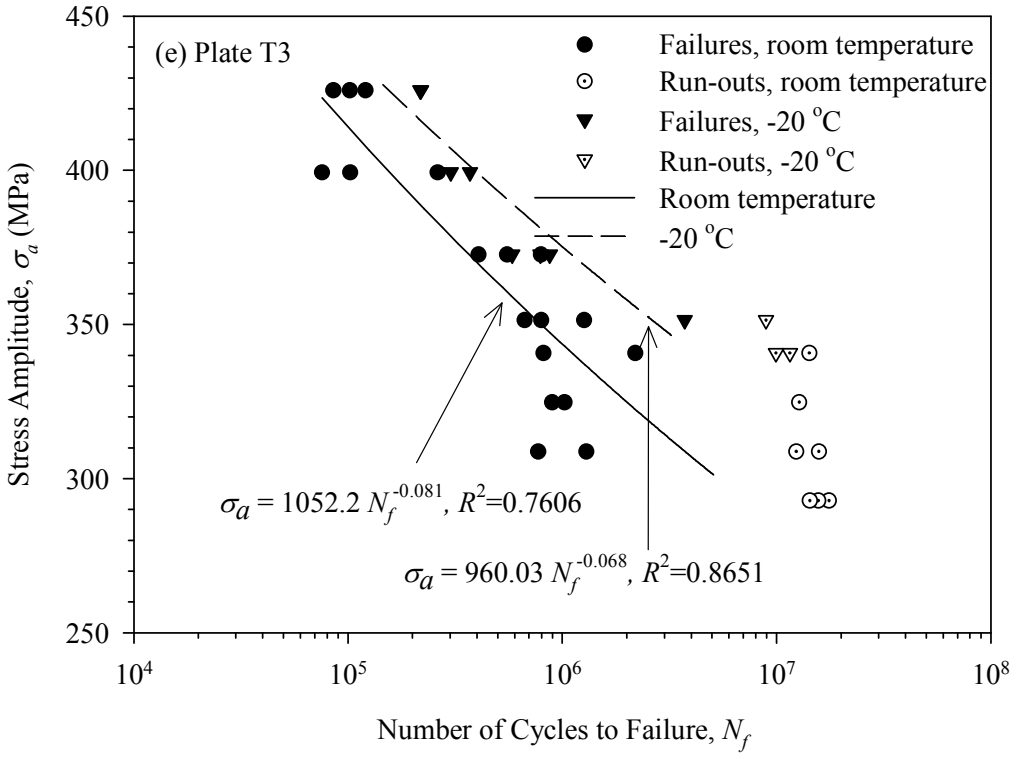

Figure 4.31 continued.

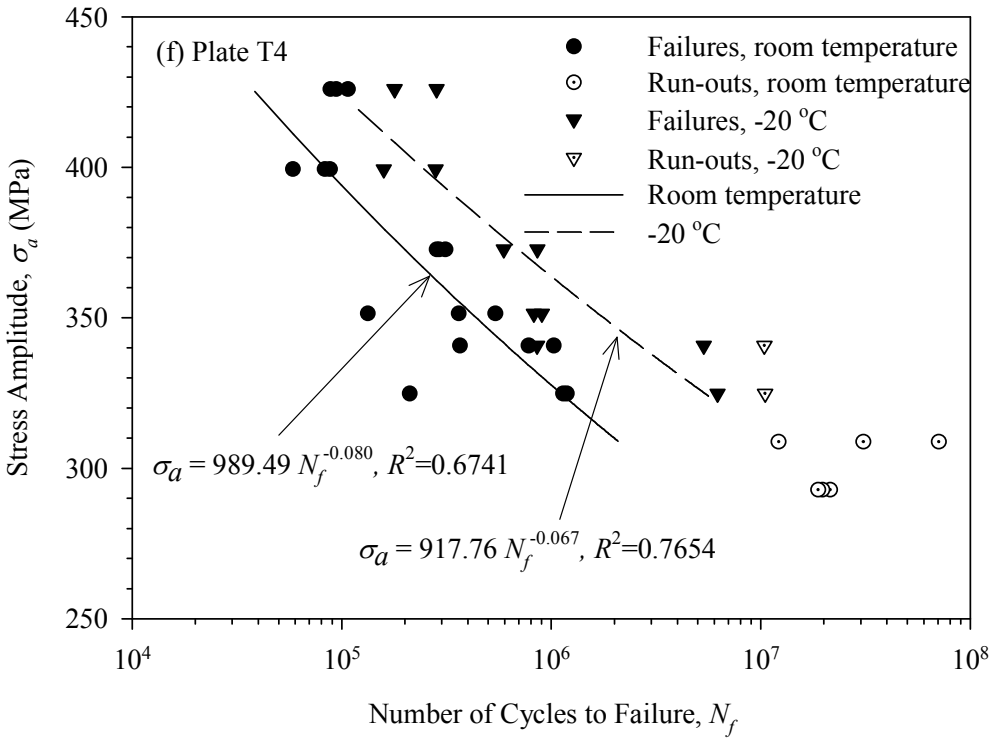

Figure 4.31 continued.

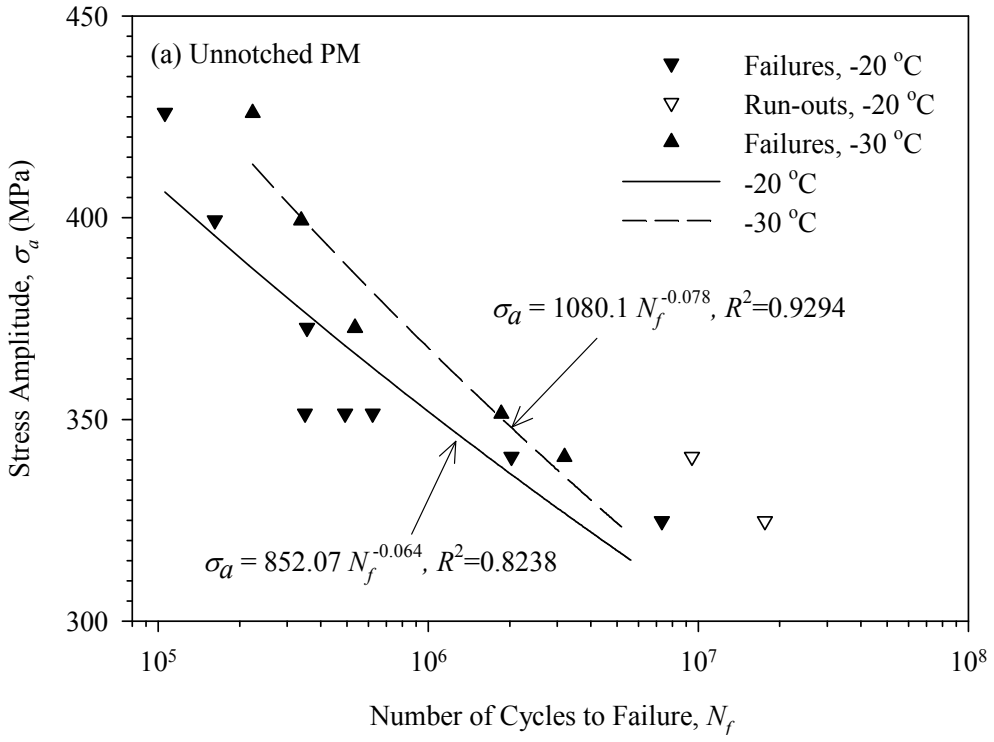

Figure 4.32. *S-N* plots for welded A709 steel specimens tested at -20 °C and -30 °C: (a) unnotched PM, (b) notched PM, (c) plate T1, (d) plate T2, (e) plate T3, and (f) plate T4. (Note: only one or two specimens were test at each stress amplitude level at -30 °C)

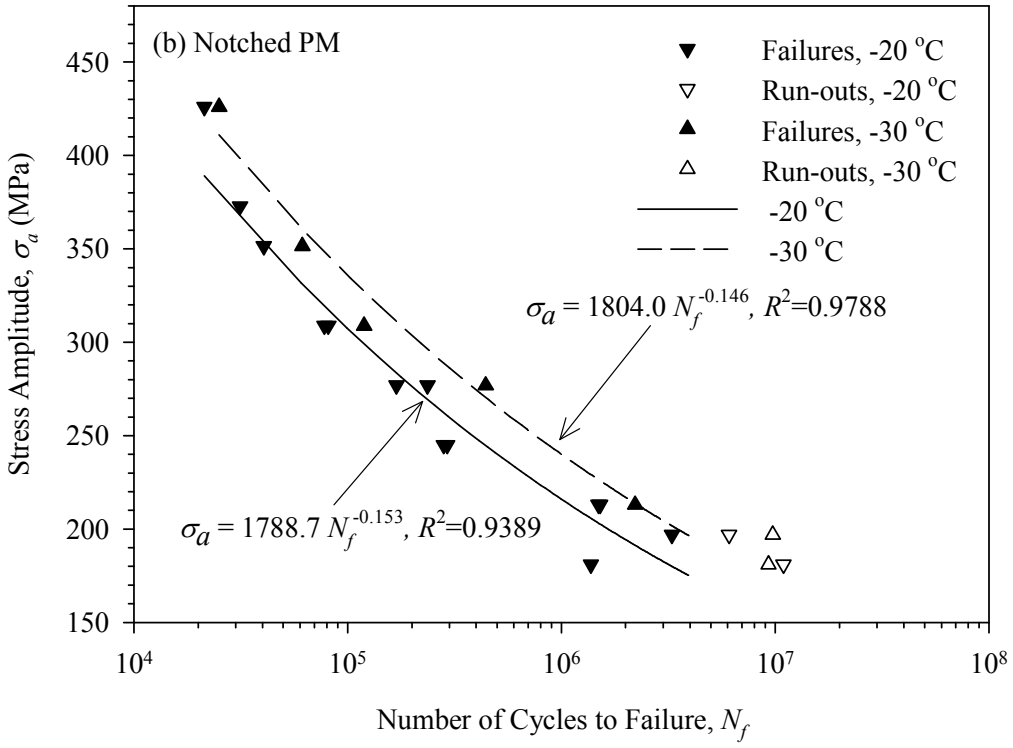

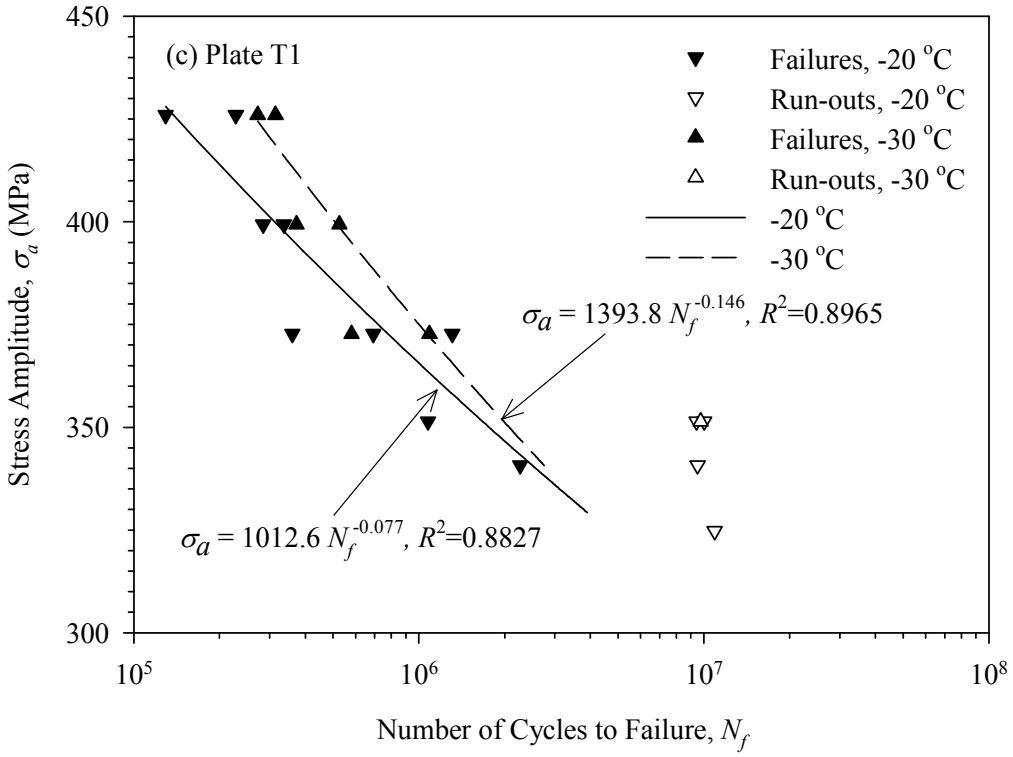

Figure 4.32 continued.

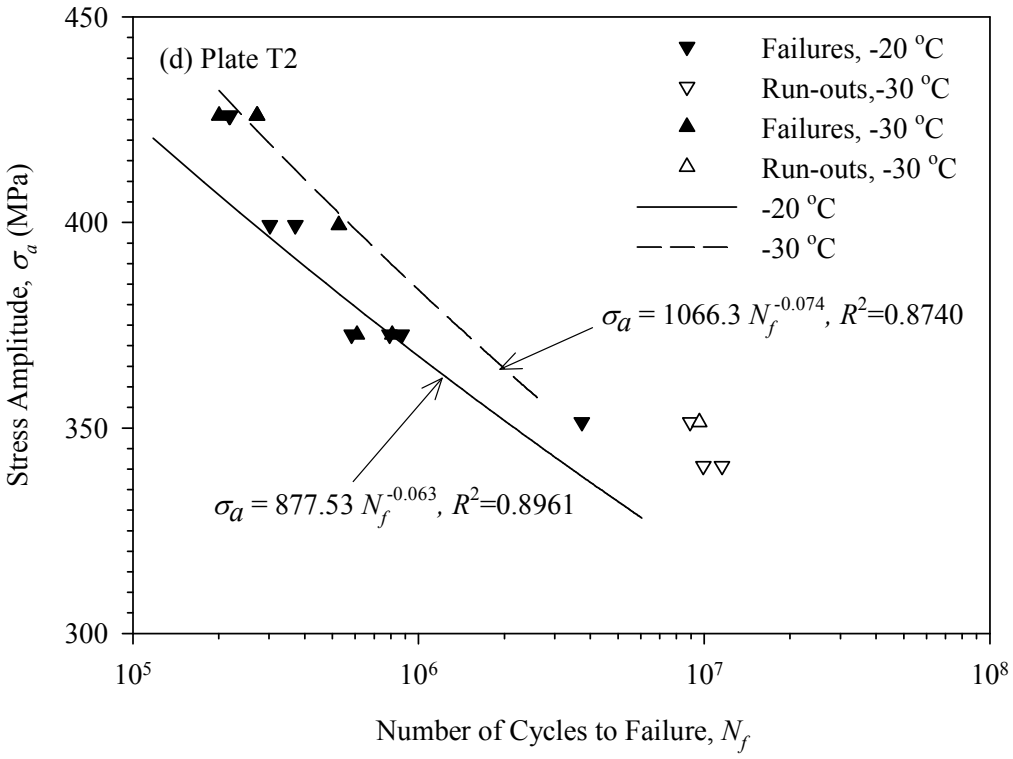

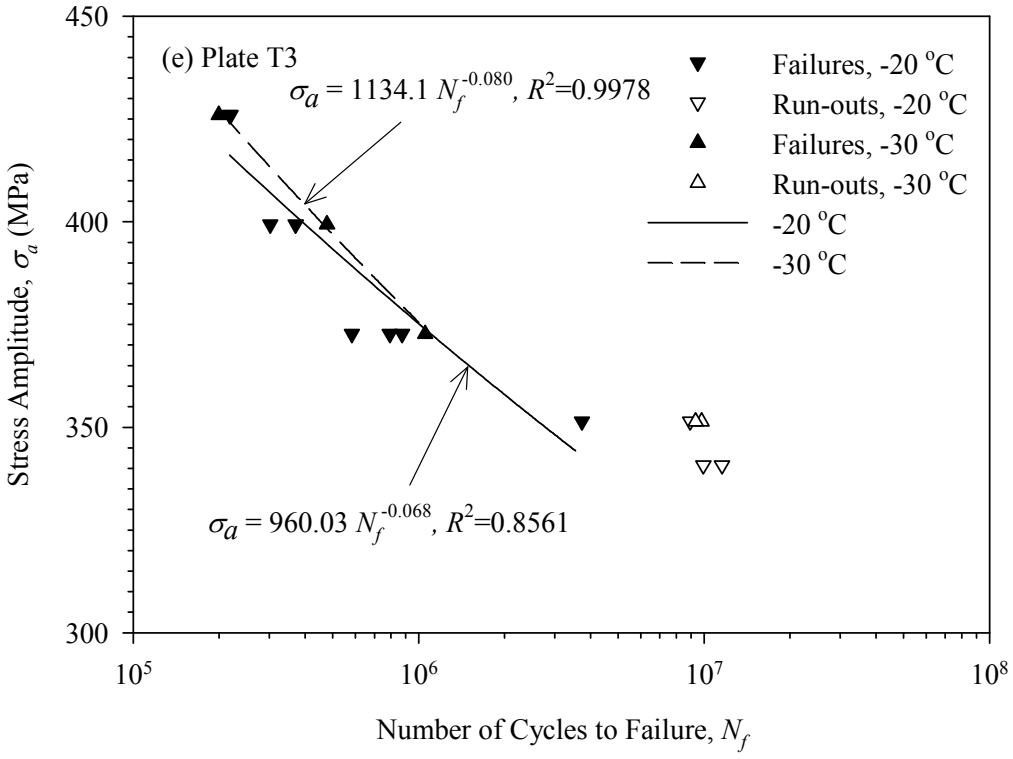

Figure 4.32 continued.

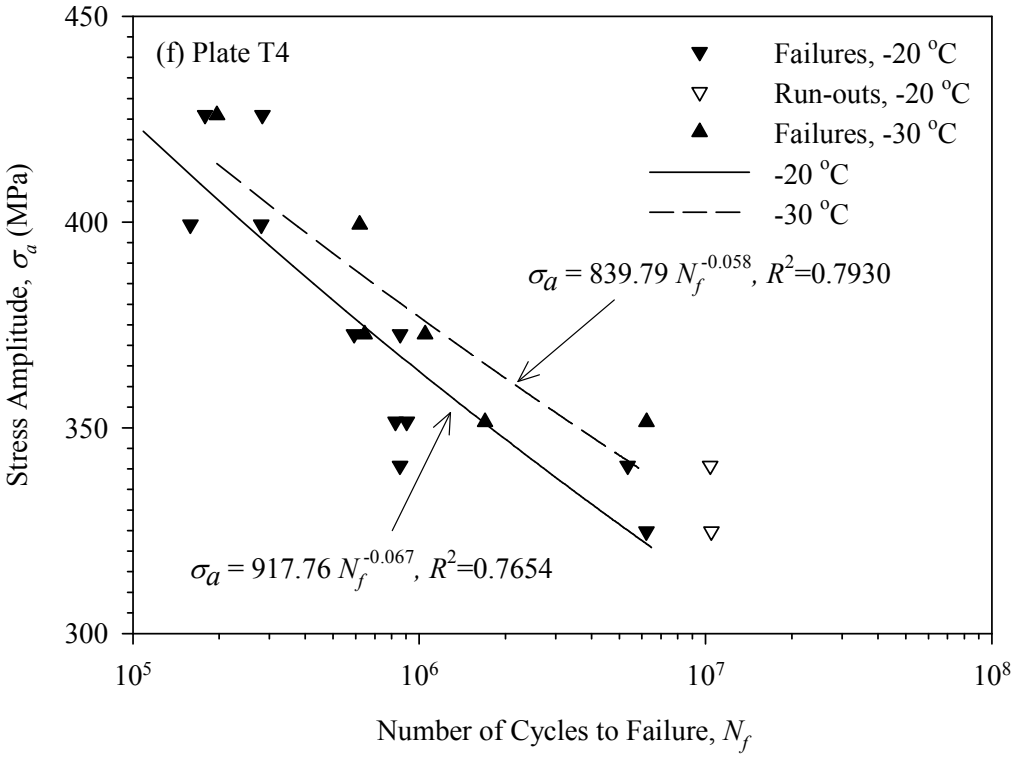

Figure 4.32 continued.

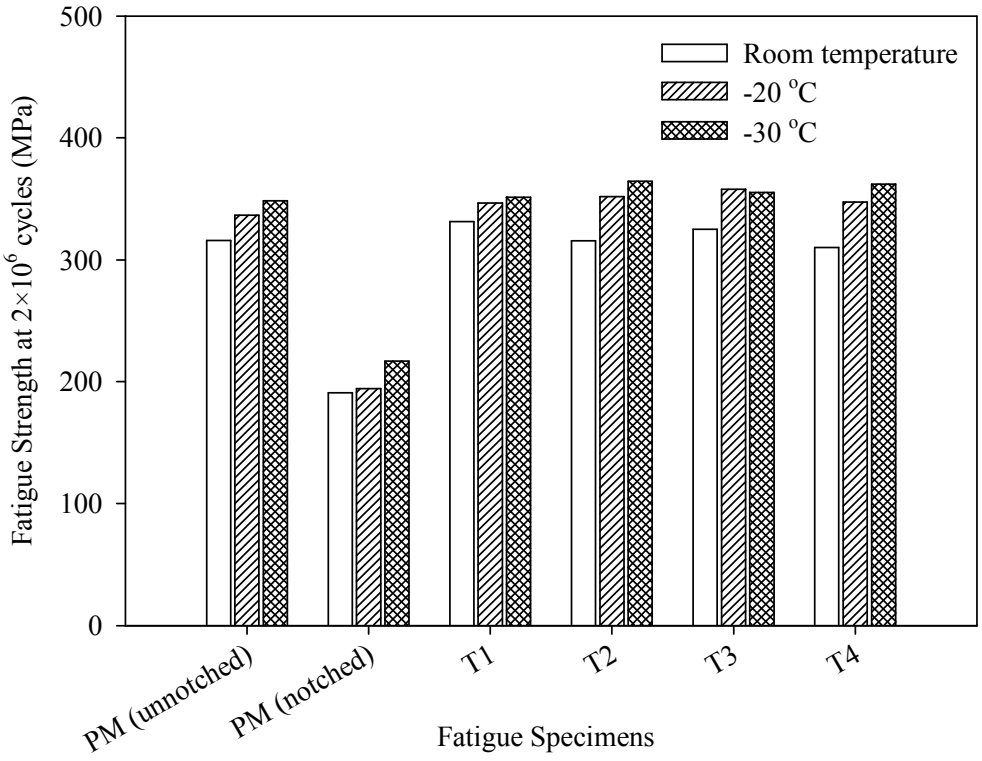

Figure 4.33. Comparison of fatigue strength at 2×10^6 cycles for different specimens at room temperature, -20 °C, and -30 °C.

Table 4.4. A comparison of fatigue limit at sub-zero temperatures with fatigue limit at room temperature.

Specimens	Fatigue limit at - 20° C / Fatigue limit at room temperature	Fatigue limit at - 30° C / Fatigue limit at room temperature
PM (unnotched)	1.066	1.103
PM (notched)	1.067	1.191
T1	1.046	1.060
T2	1.115	1.155
T3	1.102	1.094
T4	1.120	1.168

can be seen from Figure 4.33 and Table 4.4, heat input did not have appreciable effect on the fatigue strength of welded A709 steel joints at -20 °C and -30 °C, which is consistent with that at room temperature discussed in Section 4.5.3. From Figures 4.31 - 4.33, the general observation is that the fatigue strength of unnotched parent metal, notched parent metal and welded specimens increased with a reduction in temperature. This is consistent with many other works (Forrest, 1962; Frost *et al*., 1999).

The values of constants σ'_f and b obtained from *S*-*N* curves obtained from tests at -20 °C and -30 °C are summarized in Table 4.5. An approximate relationship between the fatigue strength exponent b and the cyclic strain hardening coefficient n' was suggested in (Lefebvre and Ellyin, 1984):

$$b \approx -n'/(1+5n') \tag{4.8}$$

Table 4.5. Values of σ'_f and b for the specimens at -20 °C and -30 °C.

Temperature	Specimens	Fatigue strength coefficient, σ'_f (MPa)	Fatigue strength exponent, b
-20 °C	PM (unnotched)	852.07	-0.064
	PM (notched)	1788.7	-0.153
	T1	1059.4	-0.077
	T2	877.53	-0.063
	T3	960.03	-0.068
	T4	917.76	-0.067
-30 °C	PM (unnotched)	1080.1	-0.078
	PM (notched)	1804.0	-0.146
	T1	1393.8	-0.095
	T2	1066.3	-0.074
	T3	1134.1	-0.080
	T4	839.79	-0.058

Figure 4.34 shows the estimated cyclic strain hardening coefficients using equation (4.8) for both parent metal and welded specimens at room temperature and -20 °C. Values of n' were in the range from 0.09 to 0.15, which was close to the typical range of 0.1 to 0.2 for engineering metals (Dowling, 1999). As can be seen from Figure 4.34, n' decreased with a decrease in temperature from room temperature to -20 °C. This result is consistent with the previous work of Lucas and Gerberich (1981). Those authors studied effect of low temperature on the cyclic strain hardening exponent of HSLA steel and found cyclic strain hardening exponent decreased with decreasing temperature.

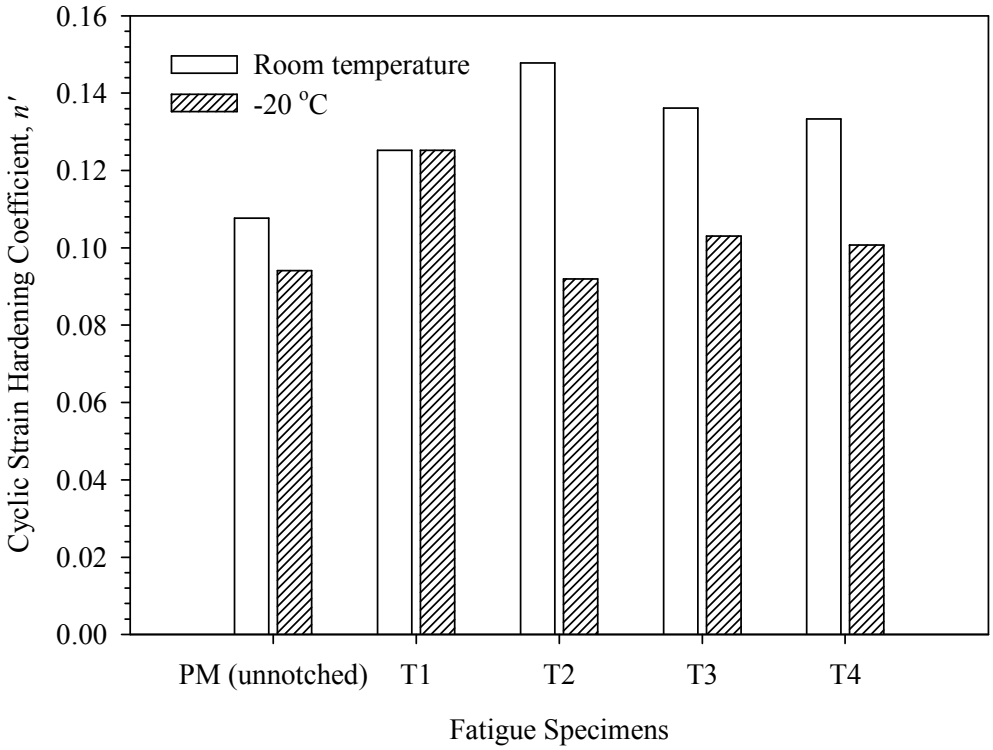

Figure 4.34. Cyclic strain hardening coefficient values for parent metal and welded specimens at room temperature and -20 °C.

Typical secondary electron SEM images obtained from a fracture surface of a fatigue specimen of plate T1 tested at -20 °C are shown in Figure 4.35. Fatigue crack propagation stage (area 1) and fracture stage (area 2) can be readily identified in Figure 4.35 (a). Figures 4.35 (b) and (c) show the magnified area 1 (fatigue fracture) and area 2 (dimple rupture). Some areas of the fracture surface were so damaged that most of striations were indiscernible. As highlighted using dotted curves in Figure 4.35 (d), only small regions of undamaged striations remained.

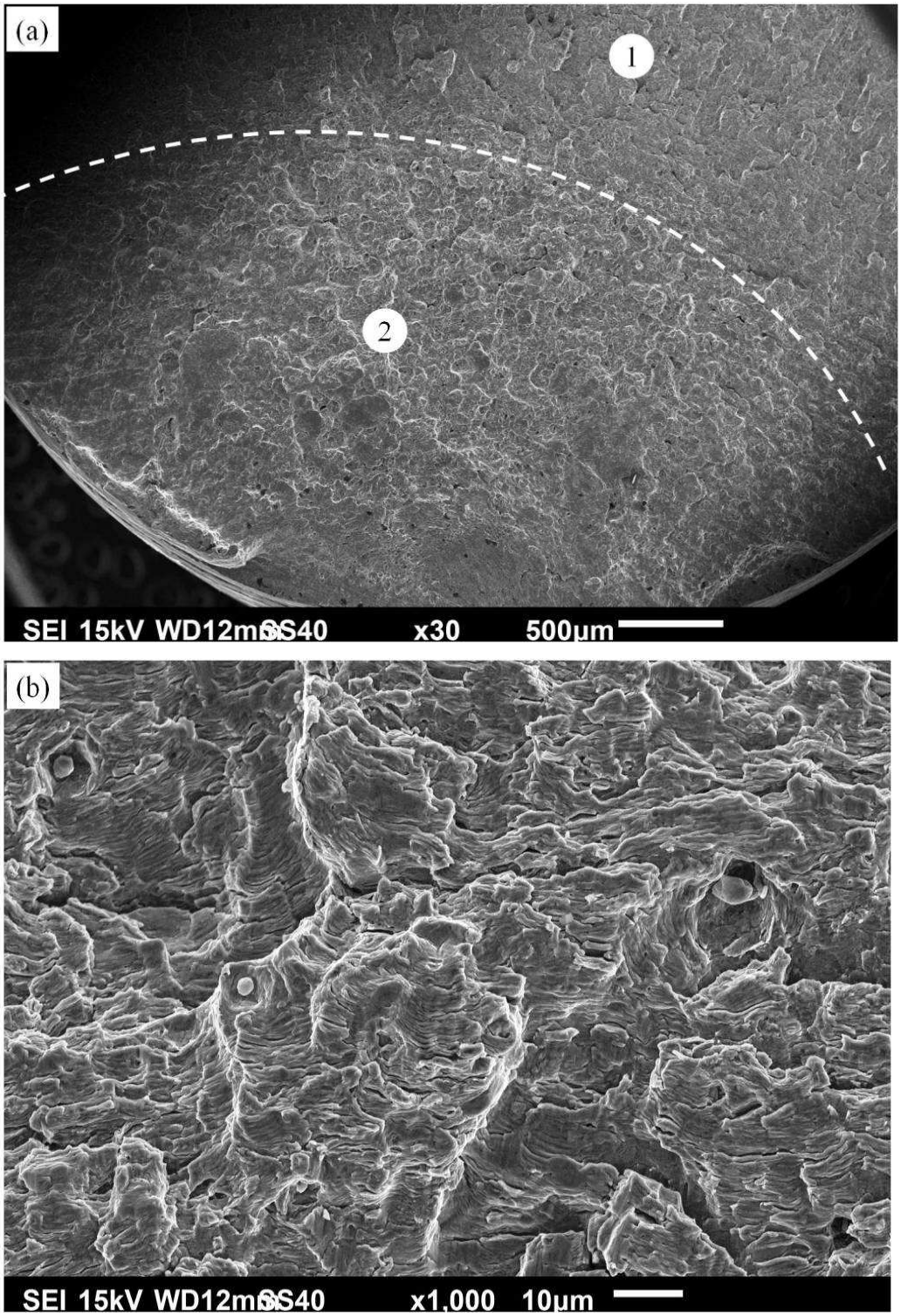

Figure 4.35. Secondary electron SEM micrographs from a fracture surface of a fatigue specimen of plate T1 tested at -20 °C: (a) low magnification image showing crack propagation stage and fracture stage, (b) fracture surface showing striations, (c) ductile fracture surface, and (d) partial damaged fracture surface showing some discernable striations.

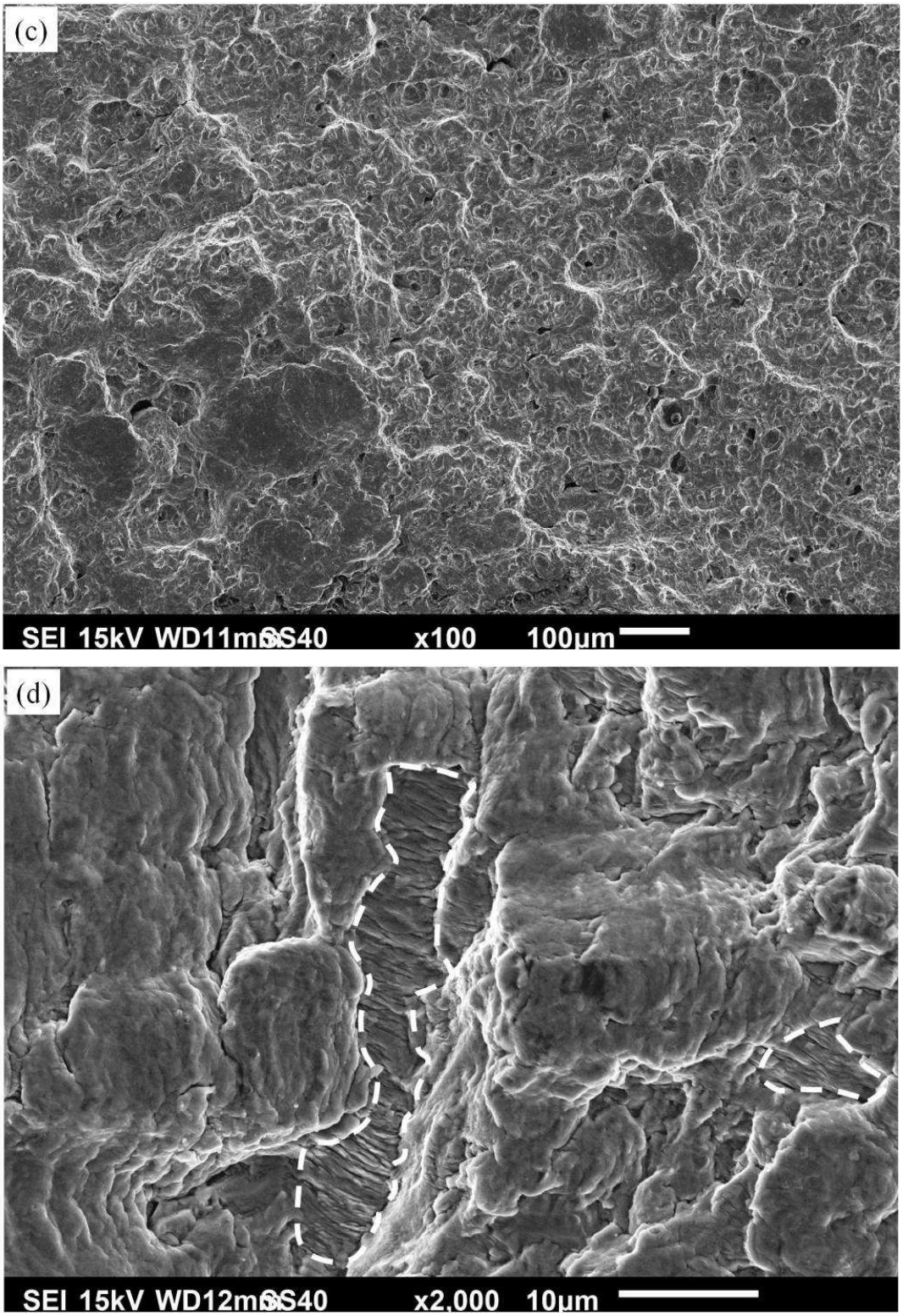

Figure 4.35 continued.

CHAPTER 5

CONCLUSIONS AND RECOMMENDATIONS

5.1 Conclusions

This study investigated the effect of heat input on the mechanical and fatigue properties of the ASTM A709 Grade 50 steel weld. Based on the analysis of the results obtained in Chapter 4, the following main conclusions can be drawn.

(1) Heat input had a strong effect on the microstructure of the weld. High heat input increased the amount of the grain boundary ferrite and slightly reduced the amount of acicular ferrite within the WM. In the CGHAZ, high heat input resulted in coarser microstructures.

(2) Heat input had an appreciable effect on the weld bead geometry of the ASTM A709 Grade 50 steel weld. With an increase in heat input, the following weld bead parameters increased: penetration depth, HAZ size, bead width, bead reinforcement, penetration area, and deposition area. However, the contact angle decreased with increasing heat input. Electrode melting efficiency increased with increasing heat input for single wire welding, but the plate melting efficiency did

not change much for both single wire and tandem wire welding. Percent dilution did not change much with heat input.

(3) The hardness of the ASTM A709 Grade 50 steel weld was different from zone to zone due to the microstructures formed in the different zones. The hardness decreased with increasing distance from the center of the WM. The WM had the highest hardness, while the PM the lowest hardness. Heat input had little effect on the hardness of the PM and the FGHAZ; however, the hardness of the CGHAZ and the WM increased with increasing heat input.

(4) The tensile and yield strengths of ASTM A709 Grade 50 steel weld did do not change appreciably with increasing heat input. They were almost the same as those of parent metal samples because all the welded specimens failed in the PM during tensile testing.

(5) At room temperature, the fatigue limit of ASTM A709 Grade 50 steel was approximately 315 MPa. The welded specimens showed similar fatigue limits with the parent material specimens, which indicates that heat input affected the fatigue life of ASTM A709 Grade 50 steel weld only slightly.

(6) The fatigue limit of ASTM A709 Grade 50 steel and its weld increased with a reduction in test temperature. Therefore, on the basis of the results obtained in this study, a design based on room temperature fatigue data would be safe for the

use at the low temperatures tested. Heat input did not have much effect on the fatigue strength of ASTM A709 Grade 50 steel welds at -20 °C and -30 °C.

(7) Notched specimens of the PM had lower fatigue limit than unnotched specimens at the same stress amplitude at room temperature, -20 °C and -30 °C.

5.2 Limitations and Recommendations

(1) All the tensile test specimens broke in the PM because the PM had the lowest strength of all the weld zones. The actual yield and tensile strengths of the WM could not be obtained. To investigate the effect of heat input on the strength and ductility of the WM, it is suggested that small-sized tensile specimens be machined from the WM.

(2) With an increase in heat input, coarsening and a slight increase in volume fraction of grain boundary ferrite in the WM was observed. However, the hardness of the WM increased. The reason for the discrepancy is unknown and requires further investigation.

(3) The data obtained showed that heat input affected the weld bead geometry which, in turn, may affect the fatigue strength of the ASTM A709 Grade 50 steel weld in real life applications. In this study, the way the fatigue specimens were cut from the welded plates made it impossible to investigate the effect of weld

bead geometry on the fatigue properties of the welded joints. A new way of machining specimens from the welded plates is required to investigate the effect of weld bead geometry on the fatigue behavior of the ASTM A709 Grade 50 steel weld.

(4) It will be informative to conduct tensile testing at the sub-zero temperatures used in this study. This will help to clarify how the stain-hardening exponent, *n*, changes with decreasing temperature in the PM and the welds.

(5) Only one or two fatigue specimens were tested at each stress amplitude level at -30 °C in this study because either the motor or the weight was frozen once the temperature reached -30 °C. To obtain more accurate S-N curves at -30 °C, more fatigue testing is required.

(6) The SEM images showed evidence of the presence of inclusions. It will be informative to know the chemical compositions of these inclusions using an SEM equipped with energy dispersive X-ray spectroscopy (EDS).

REFENENCES

Ancona D and McVeigh J, 2010, "Wind Turbine – Materials and Manufacturing Fact Sheet", Available from: http://www.perihq.com/documents/WindTurbine-MaterialsandManufacturing_FactSheet.pdf. [Accessed 2011 August 22]

ASM Handbook, 1990, *Properties and Selection: Irons, Steels and High-Performance Alloys (Volume 1)*, OH, USA: ASM International.

ASM Metals Handbook, 1983, *Welding, Brazing and Soldering (Volume 6)*, OH., USA: ASM Publication.

ASTM Standard A370, 2010, *Standard Test Methods and Definitions for Mechanical Testing of Steel Products*, West Conshohocken, PA: ASTM International.

ASTM Standard A709/A709M, 2009, *Standard Specification for Structural Steel for Bridges*, West Conshohocken, PA: ASTM International.

ASTM Standard E466, 2007, *Standard Practice for Conducting Force Controlled Constant Amplitude Axial Fatigue Tests of Metallic Materials*, West Conshohocken, PA: ASTM International

Benyounis KY and Olabi AG, 2008, "Optimization of Different Welding Processes Using Statistical and Numerical Approaches – A Reference Guide", *Advances in Engineering Software*, 39: 483-496.

Bhole SD and Billingham J, 1983, "Effect of Heat Input on HAZ Toughness in HSLA Steels", *Metals Technology*, 10 (9): 363-367.

Breen DH and Wene EM, 1978, "Fatigue in Machines and Structures – Ground Vehicles", In: *American Society for Metals, Fatigue and Microstructure*, Ohio, USA: Metals Park, p. 57-100.

Brnic J, Canadija M, Turkalj G. and Lanc D, 2010, "Structural Steel ASTM A709 – Behavior at Uniaxial Tests Conducted at Lowered and Elevated Temperatures, Short-Time Creep Response, and Fracture Toughness Calculation", *Journal of Engineering Mechanics*, September: 1083-1089.

Chakravarti AP, Thibau R and Bala SR, 1985, "Cooling Characteristics of Bead-on-Plate Welds", *Metal Construction*, March: 178R-183R.

Chandel RS, 1990, "Electrode Melting and Plate Melting Efficiencies of Submerged Arc Welding and Gas Metal Arc Welding", *Materials Science and Technology*, 6: 772-777.

Chandel RS and Hang L, 1996, "Effect of Electrode Geometry and Tilt Angle on the Plate Melting Efficiency and the GAT Welding Process", *Journal of Materials Science Letters*, 15: 2099-2100.

Chandel RS, Seow HP and Cheong FL, 1997, "Effect of Increasing Deposition Rate on the Bead Geometry of Submerged Arc Welds", *Journal of Materials Processing Technology*, 72: 124–128.

Chen HT, Grondin GY and Driver RG, 2007, "Characterization of Fatigue Properties of ASTM A709 High Performance Steel", *Journal of Constructional Steel Research*, 63: 838-848.

Cicero S, Lacalle R and Cicero R, 2009, "Estimation of the Maximum Allowable Lack of Penetration Defects in Circumferential Butt Welds of Structural Tubular Towers", *Engineering Structures*, 31: 2123-2131.

Clark JN, 1985, "Manual Metal Arc Weld Modelling Part 1: Effect of Process Parameters on Dimensions of Weld Bead and Heat-Affected Zone", *Materials Science and Technology*, 1: 1069-1079.

Connor LP, editor, 1987, *Welding Handbook*, 8th ed., Miami, FL, USA: American Welding Society.

Dallam CB, Liu S and Olson DL, 1985, "Flux Composition Dependence of Microstructure and Toughness of Submerged Arc HSLA Weldmen", *Welding Journal*, 64: 140-s-1151-s.

Davis JR, 2001, *Alloying: Understanding the Basics*, OH, USA: ASM International, Materials Park.

De Jesus AMP, Ribeiro AS and Fernandes AA, 2007, "Influence of the Submerged Are Welding in the Mechanical Behaviour of the P355NL1 Steel – Part II: Analysis of the Low/High Cycle Fatigue Behaviours", *Journal of Material Science*, 42: 5973-5981.

Dhas JER and Kumanan S, 2007, "ANFIS for Prediction of Weld Bead Width in a Submerged Arc Welding Process", *Journal of Scientific and Industrial Research*, 66: 335-338.

Donald C, Varney S and Wilbur R, 1952, *Physical Metallurgy for Engineers*, New Jersey, USA: D. Van Nostrand Company Inc., Princeton.

Dowling NE, 1999, *Mechanical Behavior of Materials: Engineering Methods for Deformation, Fracture and Fatigue*, 2nd ed., New Jersey, USA: Prentice Hall.

Easterling K, 1992, *Introduction to the Physical Metallurgy of Welding*, 2nd ed., Oxford: Butterworth-Heinemann Ltd.

Farhat H, 2007, *Effects of Multiple Wires and Welding Speed on the Msicrostructures and Properties of Submerged Arc Welded X80 Steel*, M.sc. thesis, University of Saskatchewan.

Farrar RA, Tuliani SS and Norman SR, 1974, "Relationship Between Fracture Toughness and Microstructure of Mild Steel Submerged-Arc Weld Metal", *Welding and Metal Fabrication*, 42: 68 -73.

Farrar R and Harrison P, 1987a, "Microstructure Development and Toughness of C-Mn and C-Mn-Ni Weld metals Part 2 – Toughness", *Metal Construction*, 19: 392R-399R.

Farrar RA and Norman SR, 1987b, "Acicular Ferrite in Carbon-Manganese Weld Metals: An Overview", *Journal of Materials Science*, 22: 3812-3820.

Fazzini PG, Belmonte JC, Chapetti MD and Otegui JL, 2007, "Fatigue Assessment of a Double Submerged Arc Welded Gas Pipeline", *International Journal of Fatigue*, 29: 1115-1124.

Forrest PG, 1962, *Fatigue of Metals*, Oxford: Pergamon Press.

Frost NE, Marsh KJ and Pook LP, 1999, *Metal Fatigue*, Mineola, New York, USA: Dover Publications.

Funderburk RS, 1999, "Key Concepts in Welding Engineering: A Look at Heat Input", *Welding Innovation*, XVI (1).

Gharibshahiyan E,4 Raouf AH, Parvin N and Rahimian M, 2011, "The Effect of Microstructure on Hardness and Toughness of Low Carbon Welded Steel Using Inert Gas Welding", *Materials and Design*, 32: 2042–2048.

Gladman T, 1997, *The Physical Metallurgy of Microalloyed Steels*, London: The Institute of Materials.

Gunaraj V and Murugan N, 1999, "Application of Response Surface Methodology of Predicting Weld Bead Quality in Submerged Arc Welding in Pipes", *Journal of Materials Technology*, 88: 266-275.

Güral A, Bostan B and Özdemir AT, 2007, "Heat Treatment in Two Phase Region and its Effect on Microstructure and Mechanical Strength After Welding of a Low Carbon Steel", *Materials and Design*, 28: 897-903.

Gurney TR, 1968, *Fatigue of Welded Structures*, Cambridge, England: Cambridge at the University Press.

Hall A, 2010, *The Effect of Welding Speed on the Properties of ASME SA516 Grade 70 Steel*, M.Sc. Thesis, University of Saskatchewan.

Harrison P and Farrar R, 1987, "Microstructural Development and Toughness of C-Mn and C-Mn-Ni Weld Metals Part 1 - Microstructural Development", *Metal Construction*, 19: 392R-399R.

Hrabe P, Choteborsky R and Navratilova M, 2009, "Influence of Welding Parameters on Geometry of Weld Deposit Bead", *Recent*, 10: 291-294.

Huang H, Tsai W and Lee J, 1994, "The Influences of Microstructure and Composition on the Electrochemical Behavior of A516 Steel Weldment", *Corrosion Science*, 36(6): 1027-1038.

Jang C, Cho PY, Kim M, Oh SJ and Yang JS, 2010, "Effects of Microstructure and Residual Stress on Fatigue Crack Growth of Stainless Steel Narrow Gap Welds", *Materials and Design*, 31: 1862-1870.

Jang J and Indacochea JE, 1987, "Inclusion Effects on Submerged-Arc Weld Microstructure", *Journal of Materials Science*, 22: 689-700.

Juang SC and Tang YS, 2002, "Process Parameter Selection for Optimizing the Weld Pool Geometry in the Tungsten Inert Gas Welding of Stainless Steel", *Journal of Materials Processing Technology*, 122: 33-37.

Karadeniz E, Ozsarac U and Yildiz C, 2005, "The Effect of Process Parameters on Penetration in Gas Metal Arc Welding Processes", *Materials and Design*, 28: 649-656.

Kim BC, Lee S, Kim NJ and Lee DY, 1991, "Microstructure and Local Brittle Zone Phenomena in High-Strength Low-Alloy Steel Welds", *Metallurgical Transactions A: Physical Metallurgy Materials Science*, 22A: 139-149.

Kim IS, Son JS, Kim IG, Kim JY and Kim OS, 2003, "A Study on the Relationship Between Process Variables and Bead Penetration for Robotic CO_2 Arc Welding", *Journal of Materials Processing Technology*, 136: 139-145.

Kim B, Uhm S, Lee C, Lee J and An Y, 2005, "Effects of Inclusions and Microstructures on Impact Energy of High Heat-Input Submerged-Arc-Weld Metals", *Journal of Engineering Materials and Technology*, 127: 204-213.

Kobrin MM, Matrosov and Vikman EA, 1972, "Facilities for Low-Temperature Fatigue Tests (Down to -60 °C) on Metals and Structural Components", *Consultants Bureau*, 986-990.

Kou S, 1987, *Welding Metallurgy*, New York, USA: A Wiley-Interscience Publication.

Lancaster JF, 1999, *Metallurgy of Welding*, Cambridge, England: Abington Publishing.

Lee CH, Chang KH, Jang GC and Lee CY, 2009, "Effect of Weld Geometry on the Fatigue Life of Non-Load-Carrying Fillet Welded Cruciform Joints", *Engineering Failure Analysis*, 16: 849-855.

Lee CS, Chandel RS and Seow HP, 2000, "Effect of Welding Parameters on the Size of Heat Affected Zone of Submerged Arc Welding", *Materials and Manufacturing Processes*, 15: 649-666.

Lee YL, Pan J, Hathaway R and Barkey M, 2005, *Fatigue Testing and Analysis: Theory and Practice*, Burlington, USA: Elsevier Butterworth-Heinemann.

Lefebvre D and Ellyin F, 1984, "Cyclic Response and Inelastic Strain Energy in Low Cycle Fatigue", *International Journal of Fatigue*, 6(1): 9-15.

Lucas JP and Gerberich WW, 1981, "Low Temperature and Grain Size Effects on the Cyclic Strain Hardening Exponent of an HSLA Steel", *Scripta Metallurgica*, 15(3): 327-330.

Magudeeswaran G, Balasubramanian V and Madhusudhan Reddy G, 2009, "Effect of Welding Consumables on Fatigue Performance of Shielded Metal Arc Welded High Strength, Q and T steel Joints", *Journal of Materials Engineering and Performance*, 18(1): 49-56.

McGrath JT, Chandel RS, Orr RF and Gianetto JA, 1989, "A Review of Factors Affecting the Structural Integrity of Weldments in Heavy Wall Reactor Vessels", *Canadian Metallurgical Quarterly*, 28: 75-83.

Messler RW, 2004, *Principle of Welding: Process, Physics, Chemistry, and Metallurgy*, Weinheim, Germany: Wiley-VCH Verlag BmbH & Co.

Miki C, Homma K and Tominaga T, 2002, "High Strength and High Performance Steels and Their Use in Bridge St ructures", *Journal of Constructional Steel Research*, 58: 3-20.

Moeinifar SA, Kokabi H and Madaah Hosseini HR, 2011, "Role of Tandem Submerged Arc Welding Thermal Cycles on Properties of the Heat Affected Zone in X80 Microalloyed Pipe Line Steel", *Journal of Materials Processing Technology*, 211: 368-375.

Murray A, Norrish J and Billingham J, 1996, "Assessing Offshore Submerged Arc Weld Metals", *Welding and Metal Fabrication*, 64: 267-274.

Murugan N and Gunaraj V, 2005, "Prediction and Control of Weld Bead Geometry and Shape Relationships in Submerged Arc Welding of Pipes", *Journal of Materials Processing Technology*, 168: 478-487.

Nagesh DS and Datta GL, 2002, "Prediction of Weld Bead Geometry and Penetration in Shielded Metal-Arc Welding Using Artificial Neural Networks", *Journal of Materials Processing Technology*, 123: 303–312.

Newman RP, 1959. "Effect of Fatigue Strength of Internal Defects in Welded Joints", *British Welding Journal*, 6: 59-64.

Neves J and Loureiro A, 2004, "Fracture Toughness of Welds – Effect of Brittle Zones and Strength Mismatch", *Journal of Materials Processing Technology*, 153-154: 537–543.

Ninh NT and Wahab MA, 1998, "The Effect of Weld Geometry and Residual Stresses on the Fatigue of Welded Joints under Combined Loading", *Journal of Materials Processing Technology*, 77: 201-208.

Ninh NT and Wahab MA, 1995a, "The Effect of Residual Stresses and Weld Geometry on the Improvement of Fatigue Life", *Journal of Materials Processing Technology*, 2: 581-588.

Ninh NT and Wahab MA, 1995b, "A Theoretical Study of the Effect of Weld Geometry Parameters on Fatigue Crack Propagation Life", *Engineering Fracture Mechanics*, 51(1): 1-18.

Onoro J and Ranninger C, 1997, "Fatigue Behaviour of Laser Welds of High-Strength Low-Alloy Steels", *Journal of Materials Processing Technology*, 68: 68-70.

Palani PK and Murugan N, 2007, "Optimization of Weld Bead Geometry for Stainless Steel Claddings Deposited by FCAW", *Journal of Materials Processing Technology*, 190: 291–299.

Pook L, 2007, *Metal Fatigue*, Dordrecht, The Netherlands: Springer.

Poorhaydari K, Patchett BM and Ivey DG, 2005, "Estimation of Cooling Rate in the Welding of Plates with Intermediate Thickness", *Welding Journal*, 84: 149-s-155-s.

Prasad K and Dwivedi DK, 2008, "Microstructure and Tensile Properties of Submerged Arc Welded 1.25Cr-0.5Mo Steel Joints", *Materials and Manufacturing Processes*, 23: 463-468.

Rao PS, Gupta OP, Murty SSN and Rao ABK, 2009, "Effect of Process Parameters and Mathematical Model for the Prediction of Bead Geometry in Pulsed GMA

Welding", *The International Journal of Advanced Manufacturing Technology*, 45: 496-505.

Sevensson LE, 1994, *Control of Microstructure and Properties in Steel Arc Welds*, Boca Raton: FL CRC Press.

Shul'ginov BS and Matveyev VV, 1997, "Impact Fatigue of Low-Alloy Steels and Their Welded Joints at Low Temperature", *International Journal of Fatigue*, 19: 621 - 627.

Smith NJ, McGrath JT, Gianetto JA and Orr RF, 1989, "Microstructure/Mechanical Property Relationships of Submerged Arc Welds in HSLA 80 Steel", *Welding Journal*, 68: 112-120.

Socie DF, 2002, "Fatigue Made Easy", Available from: https://www.efatigue.com/seminars/ [Accessed 2011 August 22].

Stephens RI, Fatemi A, Stephens RR, Henry O and Fuchs HO, 2001, *Metal Fatigue in Engineering*, 2nd ed, New York, USA: John Wiley and Sons.

Sundaram P, Pandey RK and Kumar AN, 1987, "Effect of the Welding Process and Heat Input on the Fracture Toughness of Welded Joints in High Strength Low Alloy Steel", *Materials Science and Engineering*, 91: 29-38.

Taylor D, Barrett N and Lucano G, 2002, "Some New Methods for Predicting Fatigue in Welded Joints", *International Journal of Fatigue*, 24: 509-518.

Tarng YS and Yang WH, 1998, "Optimization of the Weld Bead Geometry in Gas Tungsten Arc Welding by the Taguchi Method", *The International Journal of Advanced Manufacturing Technology*, 14: 549-554.

Thornton CE, 1992, "Increasing Productivity in Submerged Arc Welding", *Welding Review International*, 11: 14-15.

Vercesi J and Surian E, 1998, "Effect of Welding Parameters on High-Strength SMAW All-Weld-Metal - Part 2: AWS E10018-M and E12018-M", *Welding Journal*, 77: 164-s-171-s.

Verkin BI, Grinberg NM, Serdyuk VA and Yakovenko LF, 1983, "Low Temperature Fatigue Fracture of Metals and Alloys", *Materials Science and Engineering*, 58: 145-168.

Viano DM, Ahmed NU and Schumann GO, 2000, "Influence of Heat Input and Travel Speed on the Microstructure and Mechanical Properties of Double Tandem Submerged Arc High Strength Low Alloy Steel Weldments", *Science and Technology of Welding Joining*, 5(1): 26-34.

Wang W and Liu S, 2002, "Alloying and Microstructural Management in Developing SMAW Electrodes for HSLA-100 Steel", *Welding Journal (Miami, Fla)*, 81(7): 132-S-145-S.

Wikipedia website, "Submerged Arc Welding", Available from: http://en.wikipedia.org/wiki/Submerged_arc_welding [Assessed 2011 August 22].

Yang Y, 2008, *The Effect of Submerged Arc Welding Parameters on the Properties of Pressure Vessels and Wind Turbine Tower Steels*, M.Sc. Thesis, University of Saskatchewan.

Yurioka N, Okumura M, Kasuya T and Cotton HJU, 1987, "Prediction of HAZ Hardness of Transformable Steels", *Metal Construction*, April: 217R-223R.

APPENDIX A1

STRESS CONCENTRATION FACTOR OF A DOUBLE BUTT WELD

The fatigue stress concentration (K_f) of a double butt weld could be estimated by Peterson's Equation (Socie, 2002):

$$K_f = 1 + \frac{K_t - 1}{1 + \frac{\alpha}{\rho}} \tag{A.1}$$

where K_f is fatigue stress concentration, K_t stress concentration, α (mm) a material parameter, and ρ (mm) weld toe radius. K_t depends on weld bead parameters the contact angle (θ), plate thickness (t), and local weld toe radius (ρ), as shown in Figure A.1. With decreasing θ, stress concentration K_t increased. Since θ varies from 120° to 170° (refer to weld bead geometry measurement results), when θ = 120°, the maximum K_t is obtained. For ρ, there is a critical value that will result in the maximum K_f. This critical radius is equal to the material parameter α. K_t and α can be obtained by (Dowling, 1999)

$$K_t = 1 + \beta\sqrt{\frac{t}{\rho}} \tag{A.2}$$

$$\alpha = 0.025\left(\frac{2070}{\sigma_T}\right)^{1.8} \tag{A.3}$$

where β = 0.2 for bending, t (mm) is plate thickness, and σ_T (MPa) is ultimate tensile stress.

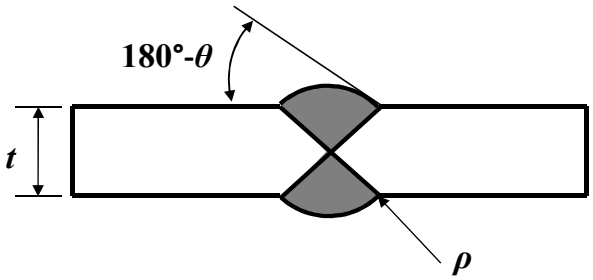

Figure A.1. A schematic diagram showing on the contact angle (θ), plate thickness (t), and local weld toe radius (ρ).

For the weld plates used in this study, σ_T = 500 MPa and t = 20 mm. Then,

$$\rho = \alpha = 0.025(\frac{2070}{\sigma_T})^{1.8} = 0.025(\frac{2070}{500})^{1.8} = 0.3225\text{mm}$$

$$K_t = 1 + \beta\sqrt{\frac{t}{\rho}} = 1 + 0.2\sqrt{\frac{20}{0.3225}} = 2.58$$

$$K_f = 1 + \frac{K_t - 1}{1 + \frac{\alpha}{\rho}} = 1 + \frac{2.58 - 1}{1 + \frac{0.3225}{0.3225}} = 1.79$$

APPENDIX A2

FATIGUE STRESS CONCENTRATION FACTOR OF NOTCHED CYLINDRICAL BAR

Cylindrical specimens with circumferential V-notch were used to study the effect of stress concentration on the fatigue properties. The notch, shown in Figure A.2, was 1 mm deep with an included angle of 60°, and a root radius of 0.34 mm.

The stress concentration factor (K_t) was estimated by a calculator provided by (https://www.efatigue.com/constantamplitude/stressconcentration/). Nominal stresses are based on the net cross section. As shown in Figure A.3, under bending loading condition, $K_t = 2.25$ was ontained.

The effective stress concentration in fatigue is less than that predicted by the stress concentration factor, K_t. This effective stress concentration factor is called the fatigue notch factor, K_f. The variation between K_f and K_t is dependent on the size of the notch and strength of the material. A material that is very sensitive to notches will have K_f equal to K_t. If the material is very insensitive to notches, K_f will be close to 1 (Socie, 2002). For steel, K_f can be estimated by equation (A.1). Then K_f could be obtained:

$$K_f = 1 + \frac{K_t - 1}{1 + \frac{\alpha}{r}} = 1 + \frac{2.25 - 1}{1 + \frac{0.3225}{0.34}} = 1.69 .$$

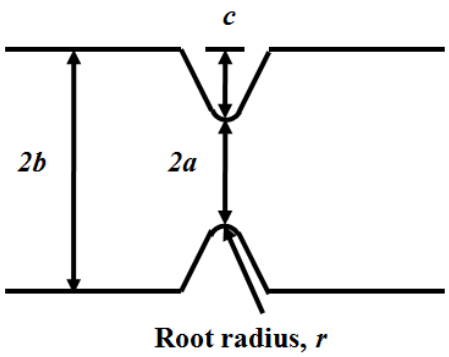

Figure A.2. Notch details of V-notched cylindrical fatigue specimen, with a = 3 mm, b = 4 mm, c = 1 mm, and r = 0.34 mm.

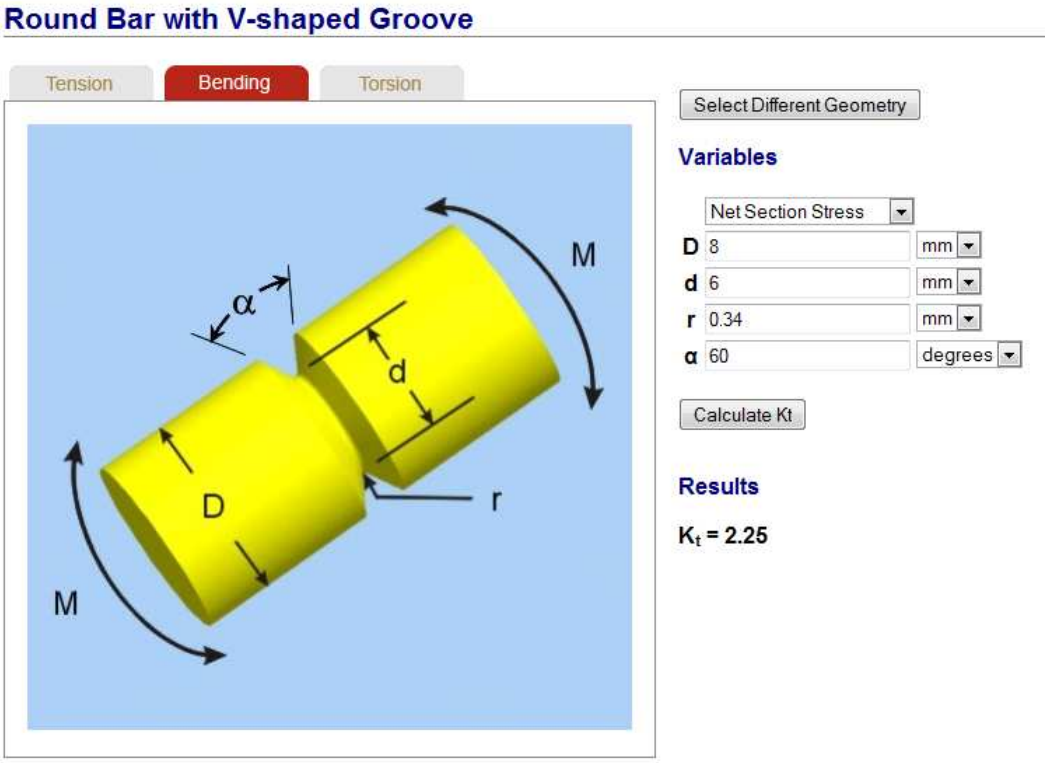

Figure A.3. Stress concentration factor (K_t) estimation of a circumferential V-notch (https://www.efatigue.com/constantamplitude/stressconcentration/).

APPENDIX B

FRACTURE SURFACE OF FATIGUE SPECIMENS

Fracture surfaces of fatigue (unnotched pare metal, notched parent metal and weled) specimens were observed by an Ancansco microscope, interfaced with a QCapture Pro 6.0 software. Observation results are shown in Figures B.1 - B.3.

Fracture surfaces of fatigue specimens (unnotched pare metal, notched parent metal and weled specimens) were also observed by a Hitachi TM3000 SEM and a JEOL JSM-6010LV SEM. SEM micrographs of unnotched parent metal, notched parent metal and weled fatigue specimens tested at room temperature and -20 °C are shown in Figures B.4 and B.9.

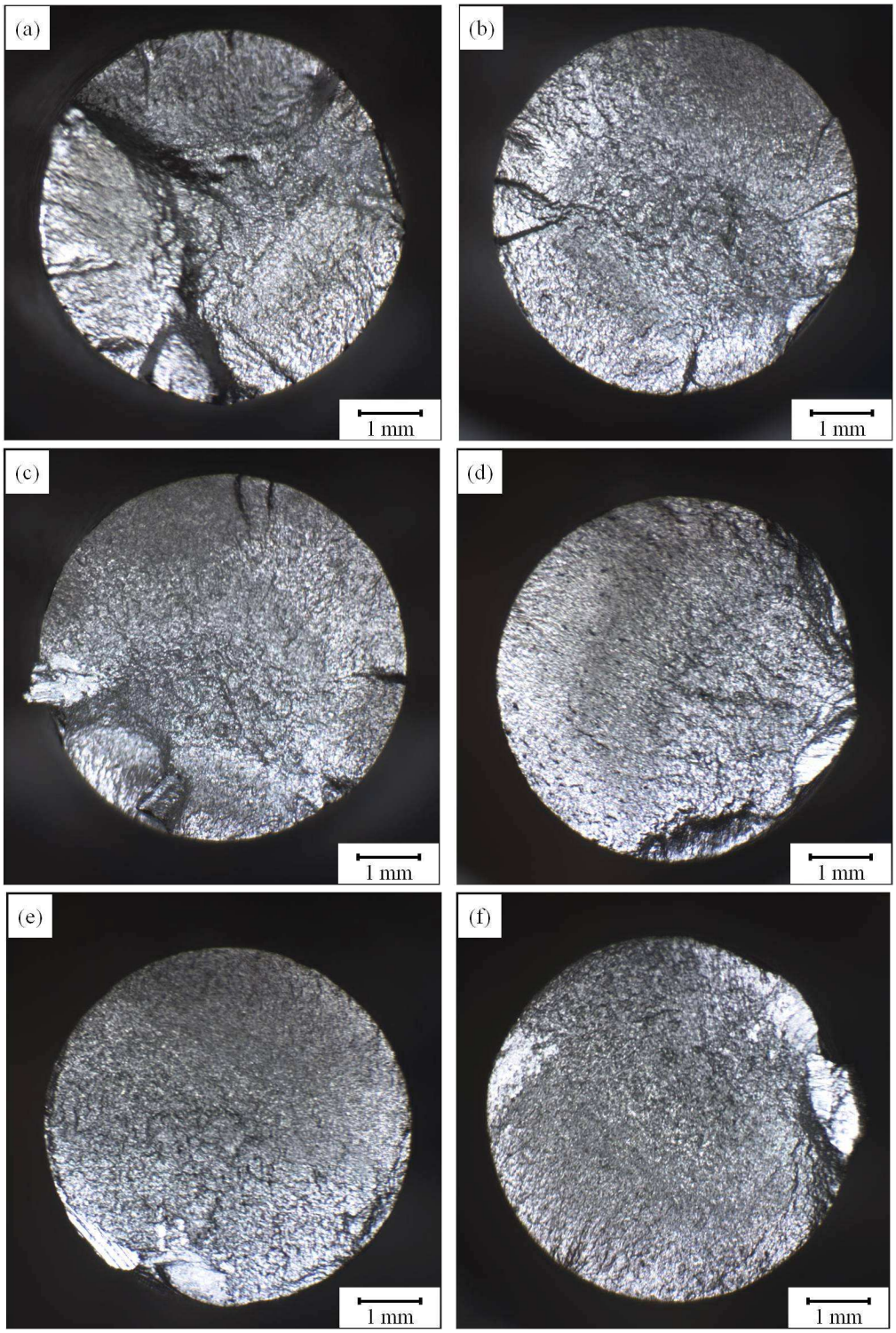

Figure B.1. Optical macrographs of fracture surfaces of fatigue specimens of unnotched parent metal: (a) failed at 2.6×10^4 cycles at the stress amplitude of 426 MPa, (b) failed at 1.3×10^5 cycles at the stress amplitude of 399 MPa, (c) failed at 2.4×10^5 cycles at the stress amplitude of 373 MPa, (d) failed at 3.0×10^5 cycles at the stress amplitude of 351 MPa, (e) failed at 9.2×10^5 cycles at the stress amplitude of 341 MPa, and (f) failed at 2.3×10^6 cycles at the stress amplitude of 325 MPa.

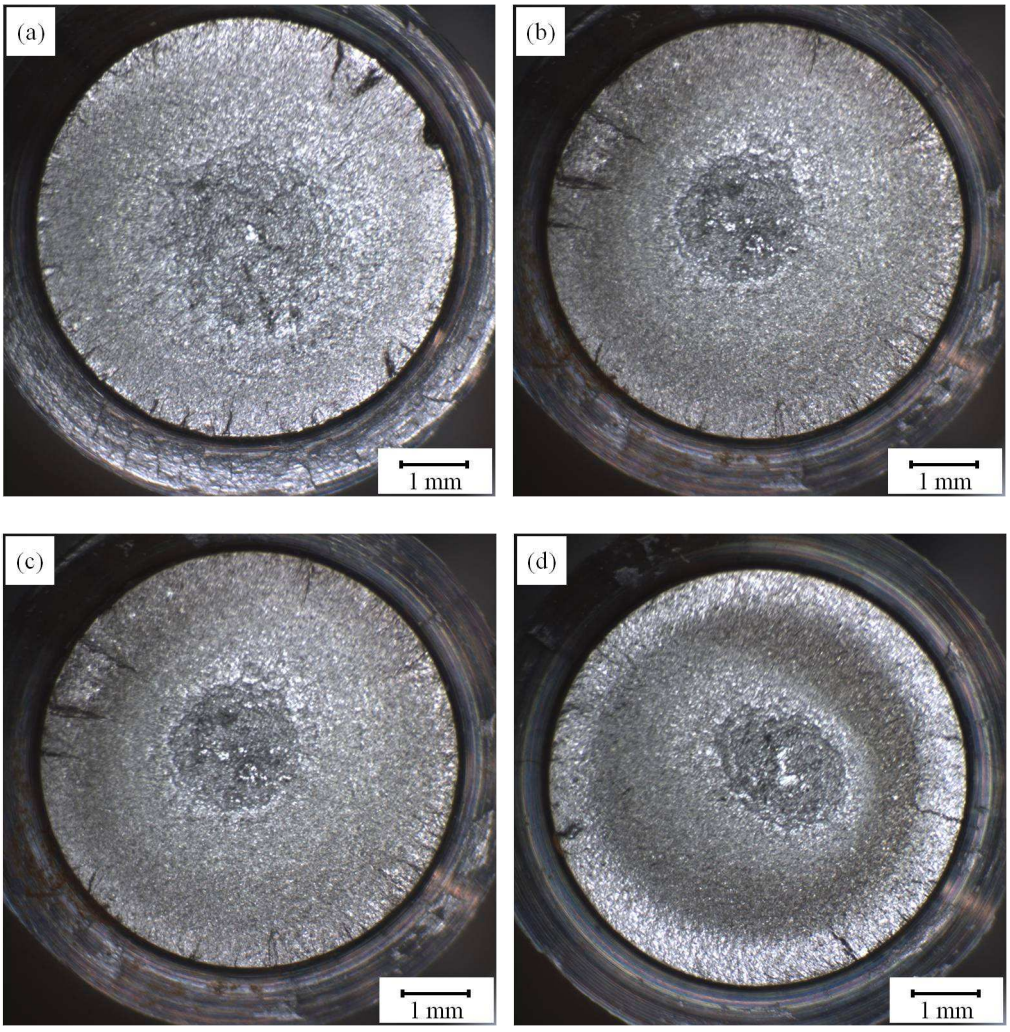

Figure B.2. Optical macrographs of fracture surfaces of fatigue specimens of notched parent metal: (a) failed at 1.8×10^4 cycles at the stress amplitude of 352 MPa, (b) failed at 1.1×10^5 cycles at the stress amplitude of 213 MPa, (c) failed at 5.2×10^5 cycles at the stress amplitude of 213 MPa, and (d) failed at 1.4×10^6 cycles at the stress amplitude of 197 MPa.

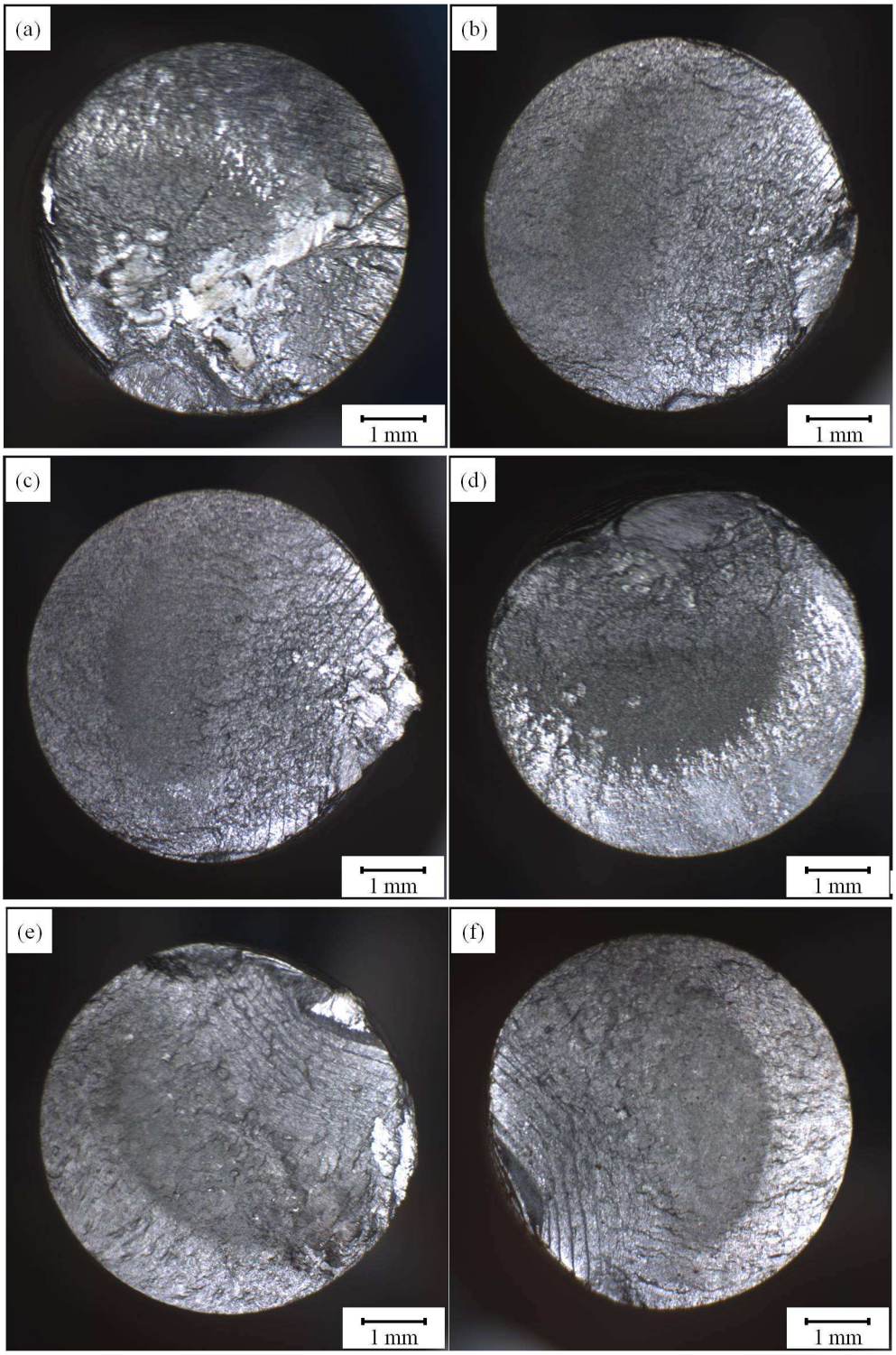

Figure B.3. Optical macrographs of fracture surfaces of fatigue specimens of welded plate T1: (a) failed at 1.3×10^5 cycles at the stress amplitude of 426 MPa, (b) failed at 1.7×10^5 cycles at the stress amplitude of 399 MPa, (c) failed at 3.3×10^5 cycles at the stress amplitude of 373 MPa, (d) failed at 4.6×10^5 cycles at the stress amplitude of 351 MPa, (e) failed at 1.4×10^6 cycles at the stress amplitude of 341 MPa, and (f) failed at 2.0×10^6 cycles at the stress amplitude of 325 MPa.

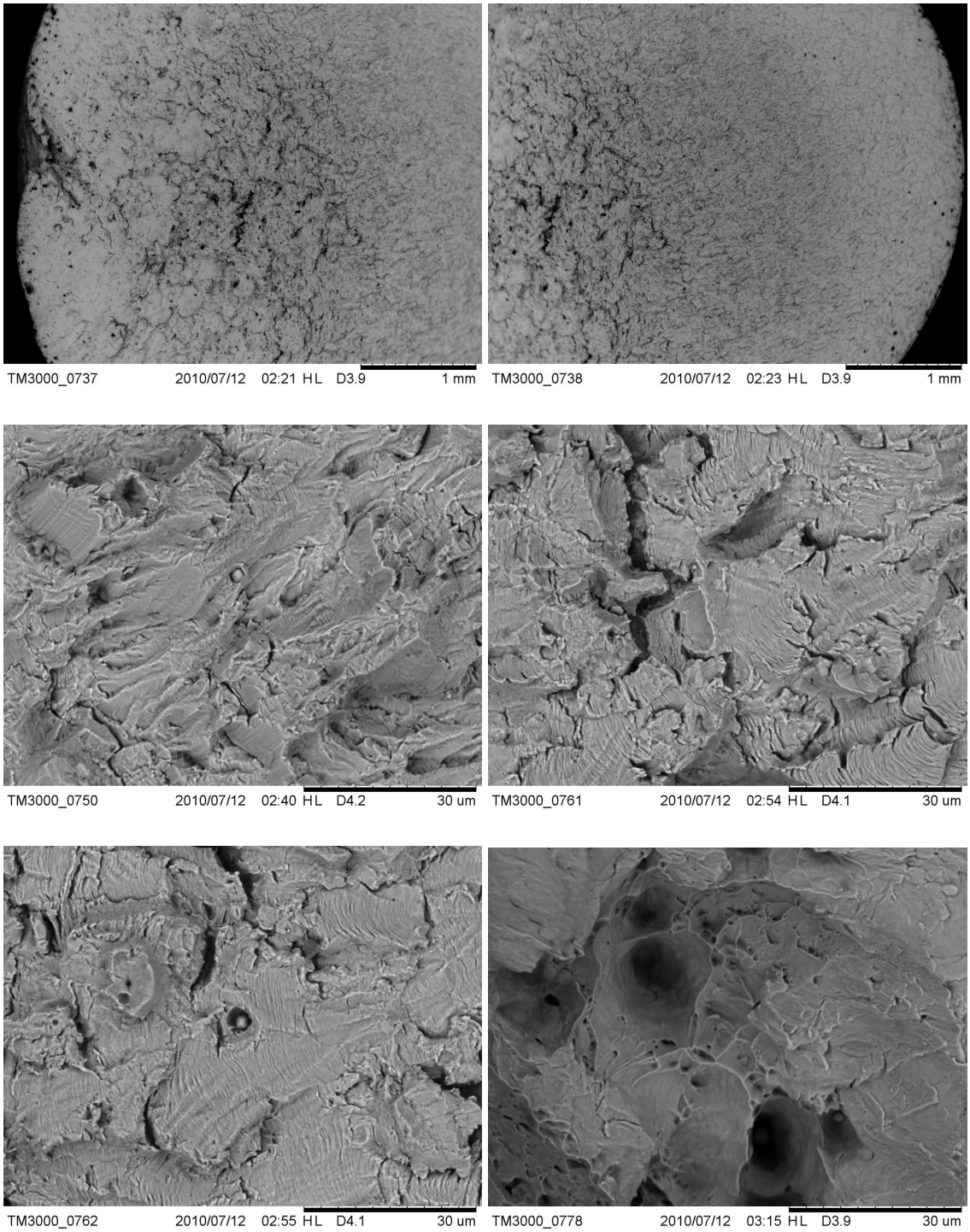

Figure B.4. Secondary electron SEM micrographs of fracture surface of a fatigue specimen of unnotched parent metal tested at roomtemperature.

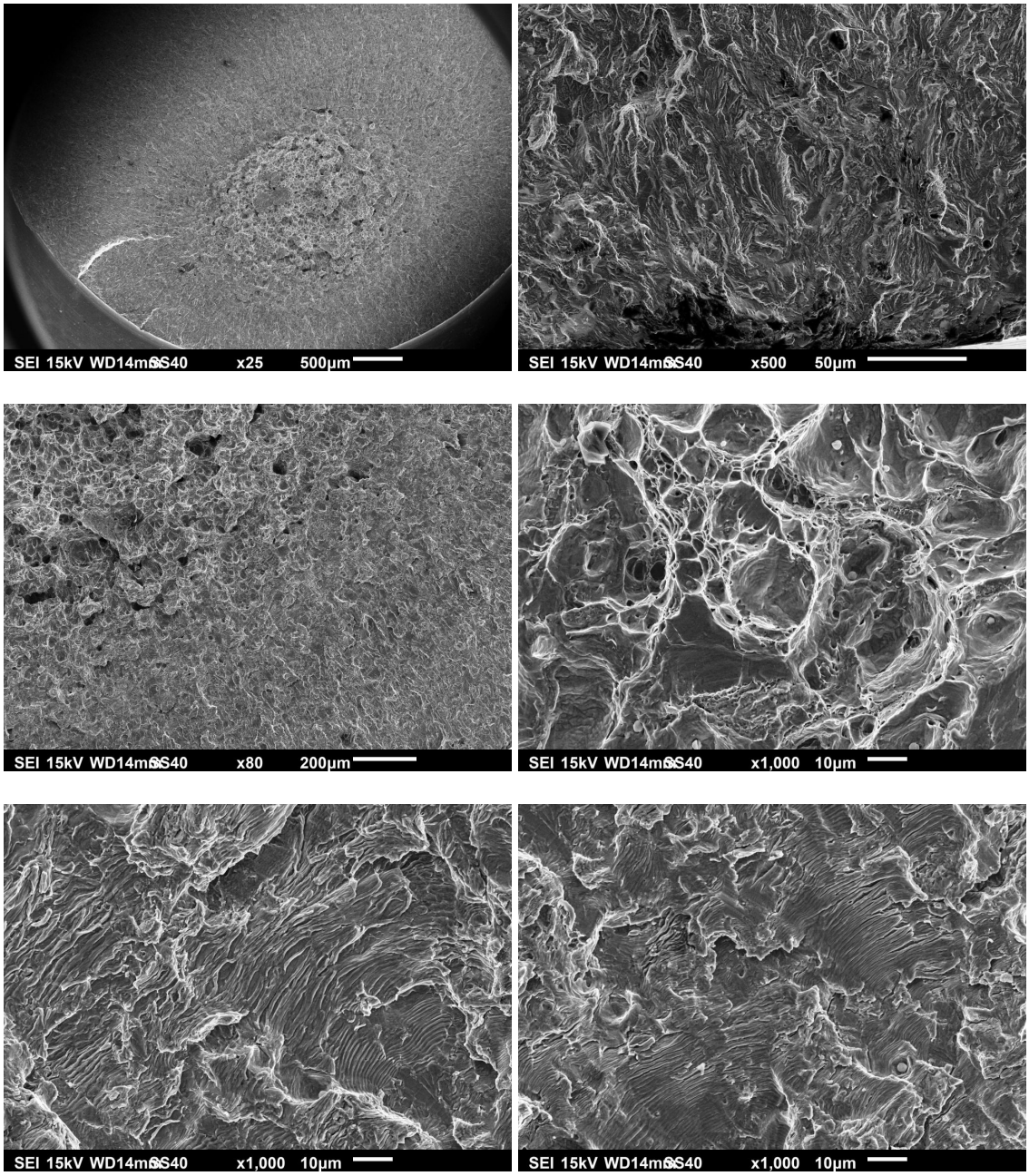

Figure B.5. Secondary electron SEM micrographs of the fracture surface of a fatigue specimen of notched parent metal tested at roomtemperature.

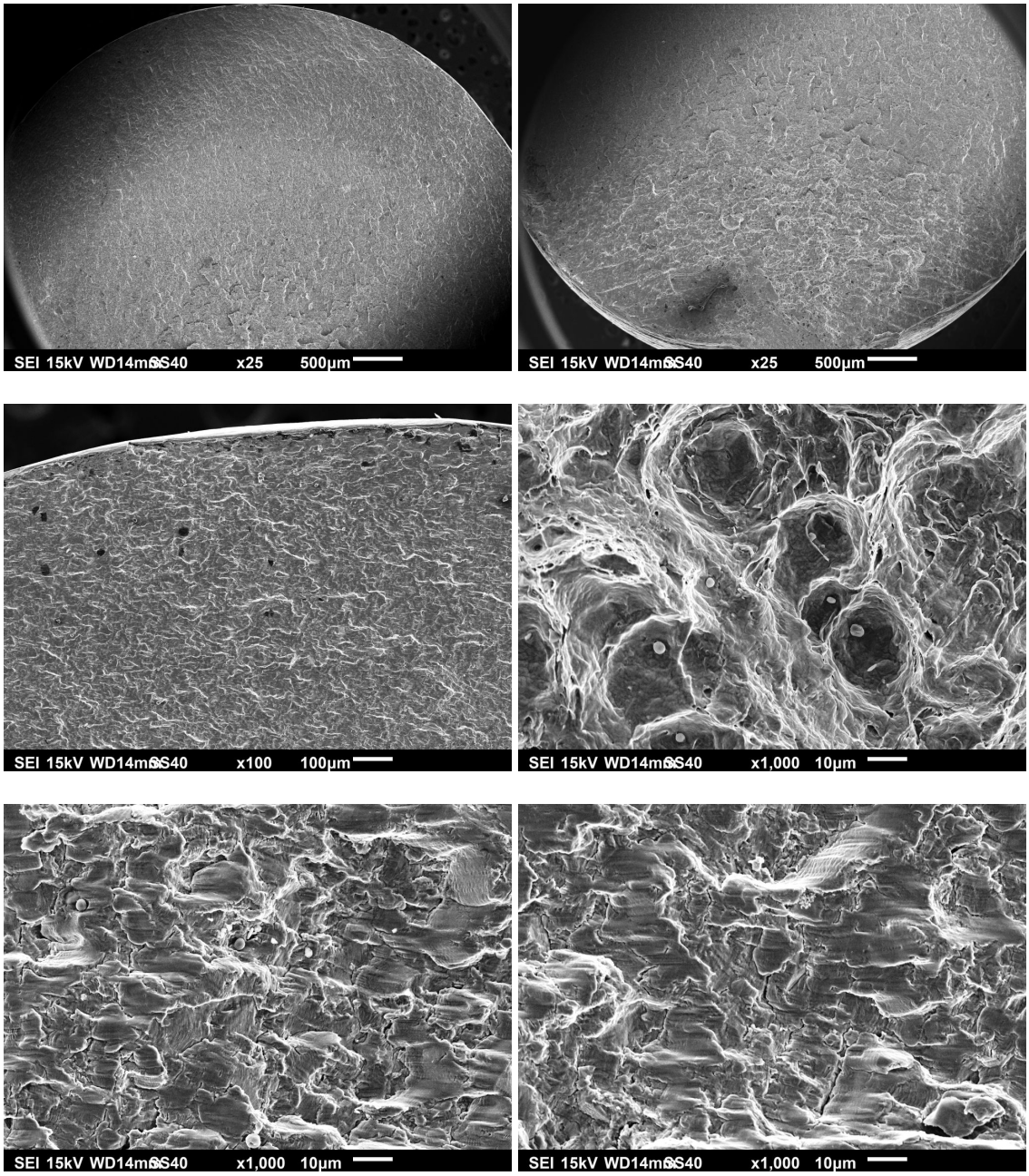

Figure B.6. Secondary electron SEM micrographs of the fracture surface of a fatigue specimen of plate T2 tested at room temperature.

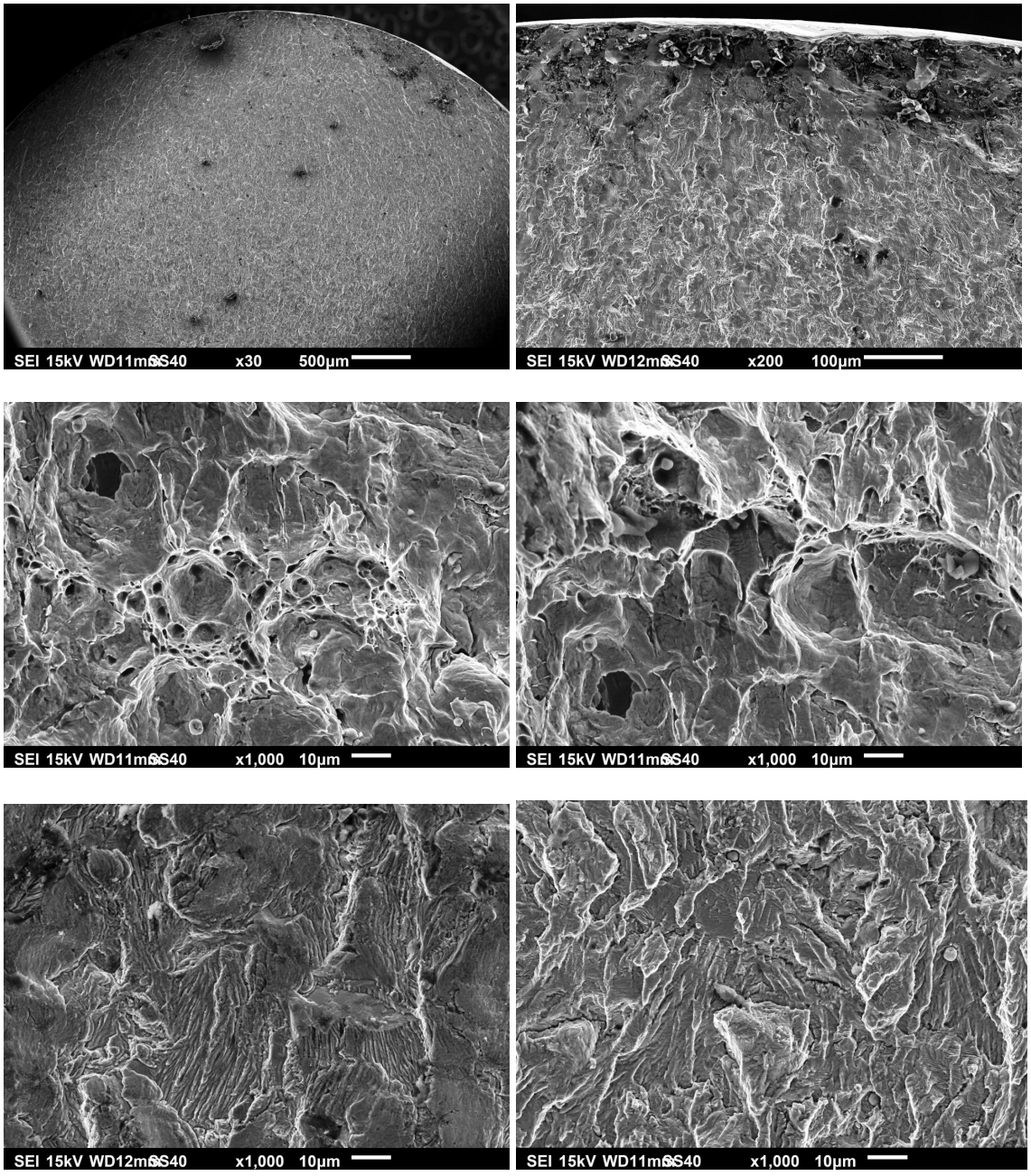

Figure B.7. Secondary electron SEM micrographs of the fracture surface of a fatigue specimen of unnotched parent metal tested at -20 °C.

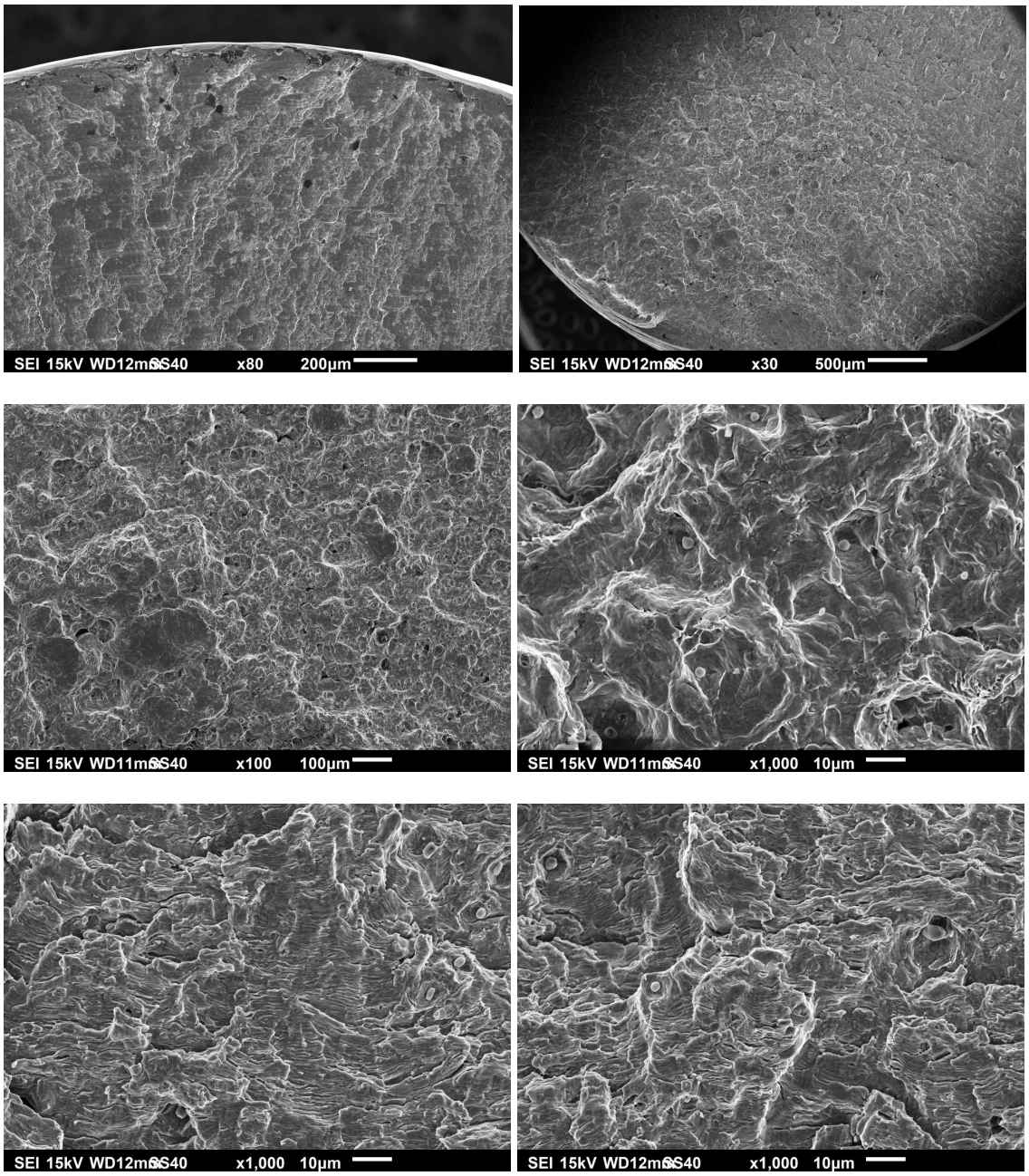

Figure B.8. Secondary electron SEM micrographs of the fracture surface of a fatigue specimen of weled plate T1 tested at -20 °C.

.

APPENDIX C

COPYRIGHT PERMISSIONS

Permission to use Figure 2.1:

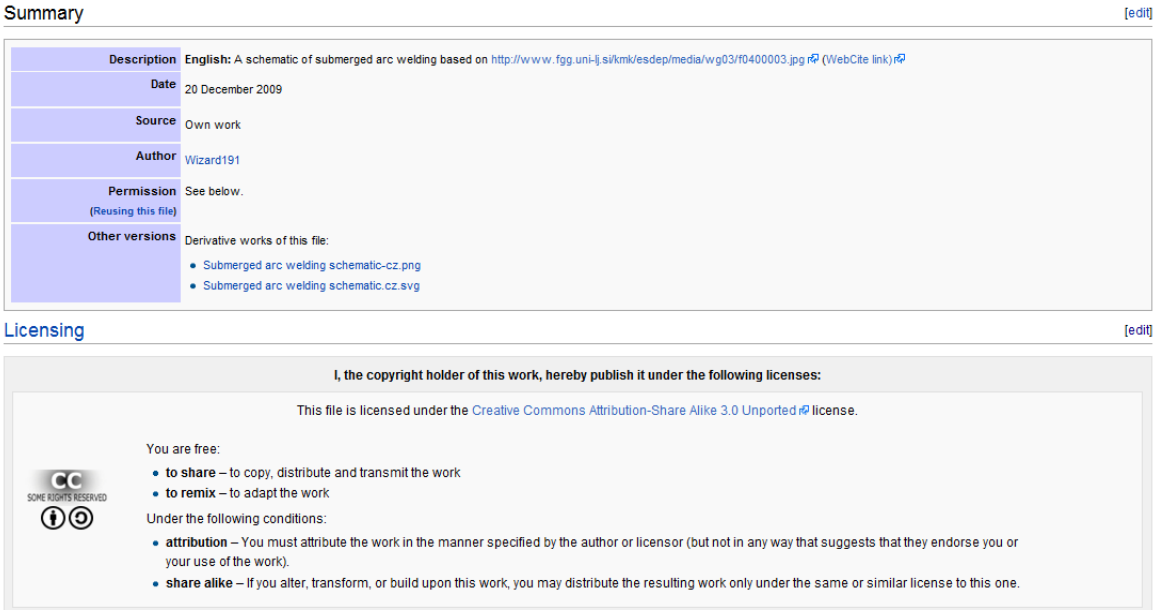

Summary [edit]

Description	**English:** A schematic of submerged arc welding based on http://www.fgg.uni-lj.si/kmk/esdep/media/wg03/f0400003.jpg (WebCite link)
Date	20 December 2009
Source	Own work
Author	Wizard191
Permission (Reusing this file)	See below.
Other versions	Derivative works of this file: • Submerged arc welding schematic-cz.png • Submerged arc welding schematic.cz.svg

Licensing [edit]

I, the copyright holder of this work, hereby publish it under the following licenses:

This file is licensed under the Creative Commons Attribution-Share Alike 3.0 Unported license.

You are free:

- **to share** – to copy, distribute and transmit the work
- **to remix** – to adapt the work

Under the following conditions:

- **attribution** – You must attribute the work in the manner specified by the author or licensor (but not in any way that suggests that they endorse you or your use of the work).
- **share alike** – If you alter, transform, or build upon this work, you may distribute the resulting work only under the same or similar license to this one.

Permission to use Figure 2.3:

From: Annette O'Brien [mailto:aobrien@aws.org]
Sent: Monday, April 25, 2011 2:37 PM
To: Jose Salgado
Subject: RE: AWS Employee Email Notification

Shufang

Your request for permission to use Figure 4.28 from Volume 1, Welding Handbook, 8th edition, was forwarded to me for response. As Editor of the Welding Handbook, I hereby grant permission to use this figure in your thesis.

This figure is reproduced as Figure 4.31 in Chapter 4 of the Welding Handbook, 9th edition. You may use the following reference if you wish to have a more current date for the reference: Welding Handbook, 9th Edition, Volume 1, Welding Science and Technology, 2001, Figure 1.31, Page 139.

Annette O'Brien

-----Original Message-----
From: Jose Salgado [mailto:jsalgado@aws.org]
Sent: Monday, April 18, 2011 9:13 AM
To: aobrien@aws.org
Subject: FW: AWS Employee Email Notification

Jose Salgado
Webmaster, AWS Marketing Team

-----Original Message-----
From: AWS Info [mailto:shs032@mail.usask.ca]
Sent: Saturday, April 16, 2011 1:04 PM
To: webmaster@aws.org
Subject: AWS Employee Email Notification

Someone has sent you an email from the AWS website. Here are the details:

Entry Date: 2011-04-16 01:04 PM
First Name: Shufang
Last Name: Shen
Email: shs032@mail.usask.ca
Phone:
Fax:
Message: Good morning Madam or Sir,

I am a Master student at the University of Saskatchewan in Saskatoon, Saskatchewan, Canada. I am writing a thesis studying the effects of welding heat input on the mechanical properties of a specific steel. In the literature review I discuss the microstructures of welded joints and would like to use your graph "Figure 4.28 – Approximate relationships among peak temperature, distance from weld interface, and the iron-carbon phase diagram" from page 110 of Welding Handbook (Connor LP, editor, 1987, Welding Handbook, 8th ed).

I would appreciate it if you would let me know how I can get the permission to use these graphs within my literature review. I would cite the book as a reference.

Thank you very much for your consideration. If you could reply as soon as possible so I can submit my thesis that would be much appreciated.

Regards,

Shufang Shen